Nanoscale Horizons

ROYAL SOCIETY OF CHEMISTRY

REVIEW

Published on 15 June 2026
Licence and permissions

Check for updates

Cite this: *Nanoscale Horiz.*, 2026, **11**, 2071

Engineering surface functional groups of MXenes for advanced catalysis and energy technology

Wenkang Xu,[a] Haoran Wang,[a] Xiaoyan An,[a] Changzhuo Xue,[a] Zhiyang Yu,[a] Chao Peng,[b] Hao-Fan Wang,[a] Yonghai Cao,[a] Hongjuan Wang[a] and Hao Yu *[a]

MXenes, as an emerging class of two-dimensional transition metal carbides, nitrides, and carbonitrides, have attracted extensive attention in catalysis and energy technology owing to their unique properties, including metallic conductivity, hydrophilic surfaces, and structural diversity. A key distinguishing feature of MXenes lies in the richness and tunability of their surface functional groups (T_x, *e.g.*, –O, –OH, –F), which serve as a powerful lever for precisely engineering the material's structural, electronic, mechanical, and chemical characteristics. The deliberate modulation of T_x, achieved through T_x engineering, including *in situ* synthesis control or post-synthetic treatments, directly governs critical properties such as work function, electrical conductivity, hydrophilicity, and oxidation stability. These tailored properties, in turn, drive performance enhancements in surface-sensitive applications: in electrocatalysis, T_x engineering optimizes intermediate adsorption and charge transfer for reactions like hydrogen evolution and CO_2 reduction; in energy storage devices such as batteries and supercapacitors, it enhances ion accessibility, redox activity, and cycling stability. This review systematically summarizes recent advances in surface T_x engineering of MXenes, elucidating the fundamental mechanisms linking T_x customization to property evolution and application-specific performance. By discussing T_x engineering strategies, structure–property–performance relationships, and mechanistic roles of distinct T_x, we aim to provide a deep understanding of how T_x tunability makes MXenes particularly suited for catalysis and energy technologies, while also outlining future directions for rational surface design in this rapidly evolving field.

Received 30th January 2026,
Accepted 2nd June 2026

DOI: 10.1039/d6nh00047a

rsc.li/nanoscale-horizons

1. Introduction

The escalating global demand for clean energy and sustainable chemical processes has intensified the search for high-performance, cost-effective, and stable functional materials.[1,2] In this context, two-dimensional (2D) materials have emerged

[a] *School of Chemistry and Chemical Engineering, South China University of Technology, Guangzhou 510641, China. E-mail: yuhao@scut.edu.cn*
[b] *School of Biotechnology and Health Sciences, Wuyi University, Jiangmen 529020, China*



Wenkang Xu

Wenkang Xu received his PhD degree in 2025 from South China University of Technology. He is currently a postdoctoral fellow at South China University of Technology, working under the supervision of Prof. Hao Yu. His research focuses on the synthesis and surface engineering of two-dimensional MXene materials, with particular emphasis on their applications in photocatalysis for energy conversion and environmental remediation.



Haoran Wang

Haoran Wang is currently an undergraduate student at South China University of Technology, expecting to graduate in 2026. He is conducting his research in the School of Chemistry and Chemical Engineering under the supervision of Prof. Hao Yu. His research interests focus on photocatalysis and catalytic oxidation over nanocarbon materials.

as promising candidates. Among them, a family of 2D transition metal carbides, nitrides, and carbonitrides, known as MXenes, has generated remarkable research momentum over the past decade.[3,4] MXenes are typically synthesized by selectively etching the 'A' layer from their parent MAX phases, yielding materials with a unique combination of properties including metallic conductivity,[5] hydrophilic surfaces,[6] rich surface chemistry,[7] and structural diversity.[8,9] These intrinsic characteristics have positioned MXenes as key components in designing advanced devices and catalytic systems,[10,11] leading to significant progress in applications such as catalysis,[12,13] batteries,[14,15] supercapacitors,[16,17] and chemical transformations.[18,19]

A paramount challenge, however, remains the rational design of MXene-based materials with predictable and optimized performance for specific applications.[20,21] This challenge underscores the critical need for a deeper, atomistic understanding of their intrinsic properties and the reaction mechanisms at their surfaces to guide precise synthesis and modification.[22,23] The performance of any material in catalysis or energy storage is inherently governed by its surface structure and composition.[24,25] For MXenes, a distinctive advantage over other 2D materials lies in the richness and tunability of their surface functional groups (T_x, *e.g.*, –O, –OH, –F). These terminations are not merely surface passivants but are active determinants of the material's fundamental properties, serving as a powerful lever for modulating its behavior. However, the initial, mixed T_x from traditional synthesis often impose inherent limitations on performance. Therefore, deliberate T_x engineering is pursued to overcome these constraints and precisely tailor the surface for application-specific demands.[26–33] Consequently, the deliberate engineering of these T_x has emerged as a central strategy for precise property control, sparking intensive investigation into their fundamental characteristics and mechanistic roles.[34–38] The influence of T_x on MXene properties is exerted through several key mechanisms. Primarily, they dictate the electronic structure by modulating the density of states near the Fermi level and shifting band alignment.[39–41] For instance, halogen T_x like –Br and –I can enhance conductivity by increasing the number of energy bands near the Fermi level.[42] The work function is also strongly correlated with T_x type, enabled by surface dipoles and weak Fermi level pinning, with values from 1.81 eV for $Ti_3C_2(OH)_2$ to 6.15 eV for $Ti_3C_2O_2$, and can even reach up to 6.31 eV with complete –N-termination.[43,44] Furthermore, surface



Xiaoyan An

Xiaoyan An is currently an undergraduate student at South China University of Technology, working under the supervision of Prof. Hao Yu, mainly focusing on the field of MXene two-dimensional materials.



Changzhuo Xue

Changzhuo Xue is currently an undergraduate student at South China University of Technology, working under the supervision of Prof. Hao Yu, mainly focusing on the field of MXene two-dimensional materials.



Zhiyang Yu

Zhiyang Yu is currently a master student at South China University of Technology, working under the supervision of Prof. Hao Yu. His research focuses on the application of two-dimensional MXene materials in photocatalysis.



Hao Yu

Professor Hao Yu received his Bachelor's degree in 1999 and PhD in 2005 from Tsinghua University. He has been teaching at South China University of Technology since 2005. He has published 200+ papers in peer-reviewed journals and has been granted 20 Chinese invention patents and 1 U.S. patent as first inventor. His research interests include development of carbon-based catalysts and their energy-environment related applications, electrified chemical processes and catalytic reaction engineering.

This journal is © The Royal Society of Chemistry 2026

T_x critically govern oxidation stability, hydrophilicity, and other physicochemical characteristics.[45–47] This intrinsic tunability makes MXenes exceptionally suitable for surface-sensitive applications like catalysis and energy storage, where interfacial processes are paramount.

These tailored properties directly govern application performance. By strategically engineering T_x, MXenes can be optimized for specific technologies.[48–50] In energy storage, for example, –O terminations optimize electrical conductivity, while hydrophilic –OH enhance ion accessibility and interfacial charge transfer, synergistically contributing to the high capacity and superior cycling stability of MXene-based supercapacitors and batteries.[51,52] In photocatalysis, modulated –OH terminations promote the separation of photogenerated holes, thereby enhancing hydrogen evolution performance.[53] The key to these advancements lies in controlling the type and distribution of T_x, achievable either *in situ* during synthesis using selective etchants (*e.g.*, HF, HCl/LiF)[49,54] or *via* post-synthetic treatments such as thermal annealing,[55] substitution,[56] or molecular grafting.[57] This unparalleled capability for precise surface engineering—spanning both synthetic and post-synthetic stages—confers a degree of property tunability that surpasses many other 2D materials, enabling systematic customization for applications ranging from high-selectivity electrocatalysts to high-power energy storage (Fig. 1).[58,59]

Despite this significant potential, a systematic and application-driven understanding of MXenes T_x remains nascent. While prior reviews have established the foundation of MXenes surface chemistry, a comprehensive analysis that specifically links the deliberate engineering of both conventional and emerging T_x to their resulting properties and ultimate performance in catalysis and energy technologies is notably absent. This review aims to fill this gap by providing a distinct, threefold perspective: it expands the scope beyond common –O, –OH, –F to systematically encompass emerging T_x such as –S, $-NH_x$, heavy halogens (–Cl, –Br, –I), and organic groups; it highlights the evolution towards sophisticated multi-step engineering strategies that combine *in situ* synthesis with post-synthetic treatments to achieve precise and pure surface terminations; and it places a strong emphasis on elucidating the fundamental structure–property–performance relationships, detailing how specific T_x dictate electronic structure, surface characteristics, and interfacial processes to drive efficiency in applications like electrocatalysis, photocatalysis, and energy storage. By consolidating this knowledge, we provide a deep understanding of how rational T_x engineering unlocks the potential of MXenes, while also outlining future directions for the design of next-generation catalytic and energy technologies.

2. Overview of functional groups of MXenes

MXenes represent a rapidly expanding family of two-dimensional transition metal carbides, nitrides, and carbonitrides. They are

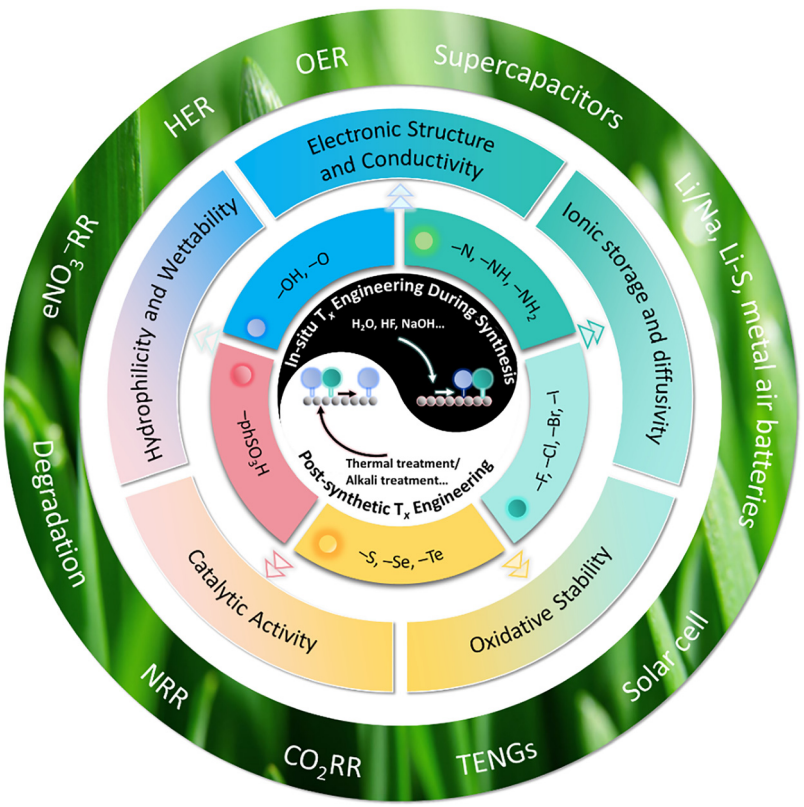

Fig. 1 The versatile functional landscape of MXenes T_x engineering for catalysis and energy technologies.

typically derived from layered ternary MAXs phase precursors by selectively etching the A-layer element, which is commonly aluminum, gallium, or silicon. MXenes are universally described by the general formula $M_{n+1}X_nT_x$, where n ranges from 1 to 4. As illustrated in Fig. 2, M denotes an early transition metal such as titanium, vanadium, molybdenum, chromium, or niobium; X represents carbon or nitrogen; and T_x signifies the diverse surface functional groups that terminate the exposed metal atoms.[4] A key distinction between MXenes and other two-dimensional materials such as graphene lies in their inherently active and readily functionalized surfaces.[62] Unlike the inert carbon lattice of graphene, MXenes sheets present exposed transition metal atoms. These metal sites are rarely left bare following aqueous etching; instead, they are promptly passivated by T_x terminations introduced during synthesis.[42] The type, coverage, and distribution of these T_x are strongly influenced by specific synthesis conditions, including the etchant type and concentration as well as drying process parameters.[65,66] Common etchants include hydrofluoric acid (HF) or hydrofluoric acid generated *in situ* (such as LiF + HCl).[60,61] This chemical exfoliation yields multilayered MXenes, which can subsequently be delaminated into single- or few-layer flakes through intercalation and sonication. Analysis of MXenes produced *via* these fluoride-based wet-chemical etching routes has confirmed the presence of characteristic T_x, including –OH (hydroxyl), –O (oxygen), –F (fluorine), and –Cl (chlorine) species, as illustrated in Fig. 2.

Subsequent advances in synthetic protocols, particularly the exploration of alternative etchants and reaction conditions, have dramatically broadened the T_x landscape. A significant expansion occurred around 2020, researchers demonstrated that a molten salt etching strategy could yield Br-terminated MXenes, and –Br groups could subsequently be replaced by –O, –S (sulfur), –Se (selenium), –Te (tellurium), –NH, and vacancies.[62] This approach greatly enriched the diversity of MXenes surface functionalities. Progress continued into 2021 with the successful incorporation of iodine (–I) terminations.[63] These emerging T_x species impart distinct structural and electronic properties to MXenes. For example, functionalization with –NH, –S, and –Se has been shown to induce superconductivity in Nb_2C, while –Te-functionalized MXenes exhibit a pronounced in-plane lattice expansion exceeding 18%.[62]

Building on these developments, post-synthetic treatments have further diversified the family of T_x terminations. In 2022, substitution of surface –Cl with –N was achieved through post-thermal treatment of $Ti_3C_2Cl_x$ in Li_3N-containing molten salt electrolytes. While the Cl-terminated pristine material shows

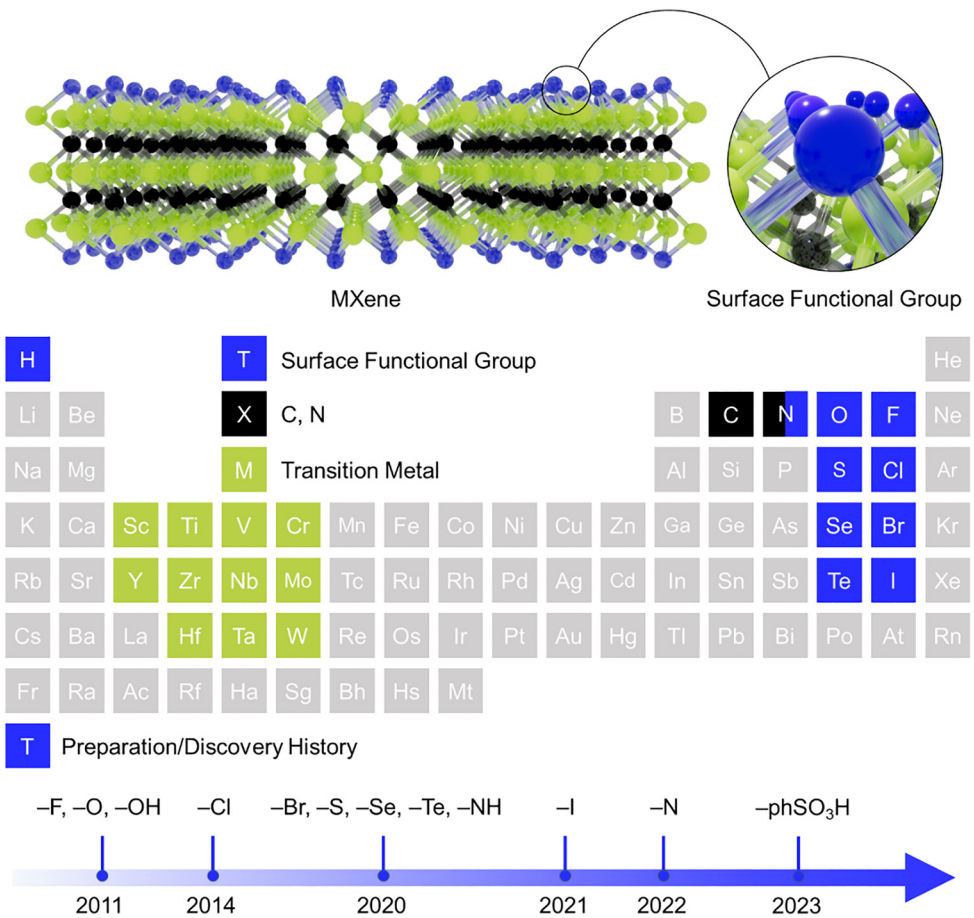

Fig. 2 Schematic representation of the MXenes general formula illustrating the key components (M, X, T_x) and the development history of T_x, showing the expansion from conventional (–O, –OH, –F, and –Cl)[60,61] to emerging (–Br,[62] –I,[63] –S, –Se, –Te, –NH, –N,[64] –phSO$_3$H,[57] *etc.*) T_x species.

 This journal is © The Royal Society of Chemistry 2026

no electrochemical activity, the N-functionalized $Ti_3C_2T_x$ exhibits a distinct capacitive-like electrochemical signature in sulfuric acid electrolyte along with improved rate performance.[64] Modification with phenylsulfonic acid T_x successfully widened the bandgap of semimetallic $Ti_3C_2T_x$ MXenes to 1.53 eV, rendering it promising as a photosensitive material.[57] These post-synthetic approaches have thus substantially enriched the variety of T_x species and broadened the application scope of MXenes. The regulation of T_x in MXenes has become an active research field.

3. Formation and structure of functional groups of MXenes

3.1. Formation of T_x

The formation of surface T_x on MXenes is an inevitable consequence dictated by the specific synthesis strategies and environmental conditions employed. Taking the most prevalent synthesis route as an example, as shown in Fig. 3, MXenes are typically produced by etching the precursor MAXs phase using HF or fluoride-containing etchants that generate HF *in situ*. The etching process for a classic precursor like Ti_3AlC_2 MAX phase can be summarized by the simplified reaction:[54]

$$Ti_3AlC_2 + 3HF \rightarrow Ti_3C_2 + AlF_3 + 1.5H_2 \quad (1)$$

However, this stoichiometric equation offers an incomplete description. As shown in Fig. 3, the freshly exposed MXenes layers contain highly reactive undercoordinated transition metal atoms on the surface, which are rapidly passivated by anions present in the etching solution. This leads to surface termination with various T_x. In conventional HF-based and HF *in situ* etching methods, the introduced T_x originate from distinct sources: –F originate directly from HF molecules or F^- ions, while –O and –OH are mainly introduced from H_2O, which is invariably present in the HF solution and the ambient environment.[54] Depending on the specific synthesis conditions, other $\mathbf{T_x}$ may also be incorporated. For instance, etchants containing Cl^- inevitably result in the introduction of –Cl, as shown in the following representative reactions:[54]

$$Ti_3C_2 + 2HF \rightarrow Ti_3C_2\mathbf{(F)_2} + H_2 \quad (2)$$

$$Ti_3C_2 + 2H_2O \rightarrow Ti_3C_2\mathbf{(OH)_2} + H_2 \quad (3)$$

$$Ti_3C_2 + 2H_2O \rightarrow Ti_3C_2\mathbf{(O)_2} + 2H_2 \quad (4)$$

$$Ti_3C_2 + 2HCl \rightarrow Ti_3C_2\mathbf{(Cl)_2} + H_2 \quad (5)$$

The types and proportions of these T_x is thus directly governed by the chemical composition of the etching medium and subsequent processing conditions.[65] As a result, the surface of a freshly synthesized MXenes produced using HF typically exhibits a mixture of T_x, predominantly –O, –OH, and –F. This is reflected in the general chemical formula $M_{n+1}X_nO_x(OH)_yF_z$. The relative proportions of these T_x are strongly influenced by etching parameters, including HF concentration, temperature, duration, and solvent choice, as well as by the post-synthetic storage environment.[68–70] For instance, higher HF concentrations generally promote a greater –F content, whereas etchants containing polyols have been reported to yield MXenes with –OH-rich surfaces.[71,72] Modulating the T_x composition of MXenes during the synthesis process represents a highly rational design approach.[73,74]

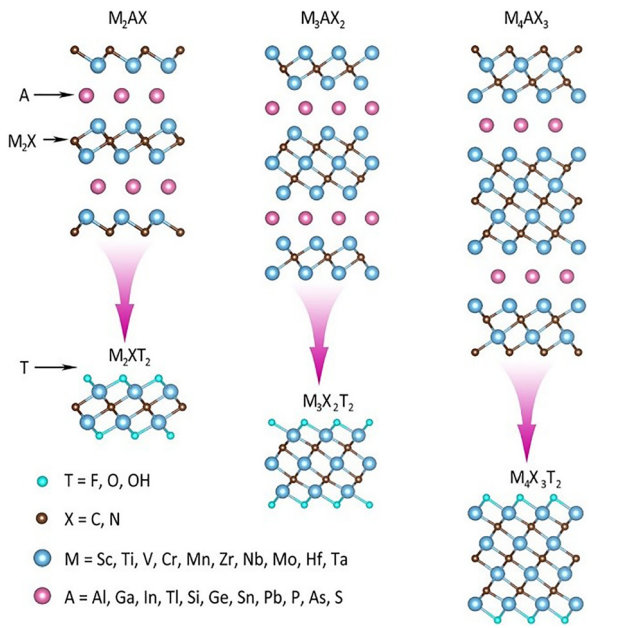

Fig. 3 Schematic diagram of the structure of MXenes synthesized by MAXs etching and the formation of T_x. [Fig. 3 adapted with permission from ref. 67 Copyright © 2018 Elsevier Inc.].

3.2. Atomic structure and stability of T_x

Understanding the precise atomic arrangement of these T_x on the MXenes surface is crucial for predicting and interpreting their chemical properties. MXenes typically exhibit a hexagonal close-packed structure with two distinct sites for T_x to bind on the surface: the hollow site directly above the second-layer transition metal atom (referred to as the FCC site), and the hollow site directly above the central carbon atom (referred to as the HCP site), as illustrated in Fig. 4(a)–(c).[75,76]

Different T_x on MXenes surfaces compete for thermodynamically stable sites. Scanning transmission electron microscopy (STEM) studies have revealed that –F preferentially occupy the FCC sites, while oxygen atoms can simultaneously occupy both FCC and HCP sites.[77] Complementary to experimental observations, first-principles calculations further demonstrate that the distribution of T_x on MXenes surfaces exhibits a strong preference for a mixed configuration, with no evidence of phase separation (Fig. 4(d)). These results indicate that the mixed T_x distribution on the MXenes surface corresponds to the thermodynamically stable state under ambient conditions.[68]

T_x can desorb or exchange with one another, as illustrated in Fig. 5. The main paths that have been reported are as follows (6)–(11):[76]

$$M_{n+1}X_nO_2 + 2H_2\,(g) \rightarrow M_{n+1}X_n + H_2O\ (\text{heating}) \quad (6)$$

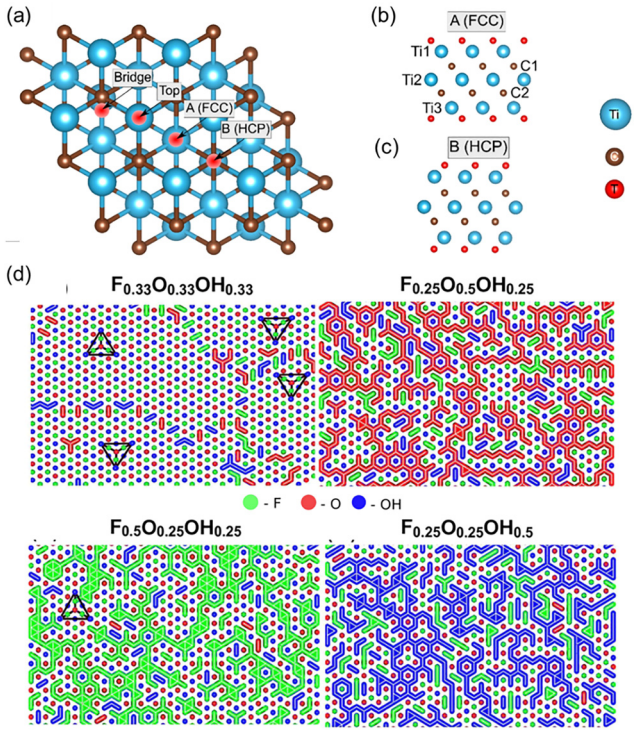

Fig. 4 Schematic illustration of the different adsorption sites of $Ti_3C_2T_x$. (a) Top view and side views of (b) A (FCC) adsorption site (on top of M atom in the third atomic layer), and (c) B (HCP) adsorption site (on top of X atom in the second atomic layer). (d) Surface structures for $Ti_3C_2(O_{0.33}OH_{0.33}F_{0.33})_2$, $Ti_3C_2(O_{0.25}OH_{0.5}F_{0.25})_2$, $Ti_3C_2(O_{0.5}OH_{0.25}F_{0.25})_2$, $Ti_3C_2(O_{0.25}OH_{0.25}F_{0.5})_2$. [(a)–(c) Adapted with permission from ref. 75. Copyright © 2019 American Chemical Society. (d) Adapted with permission from ref. 68 Copyright © 2019 American Chemical Society].

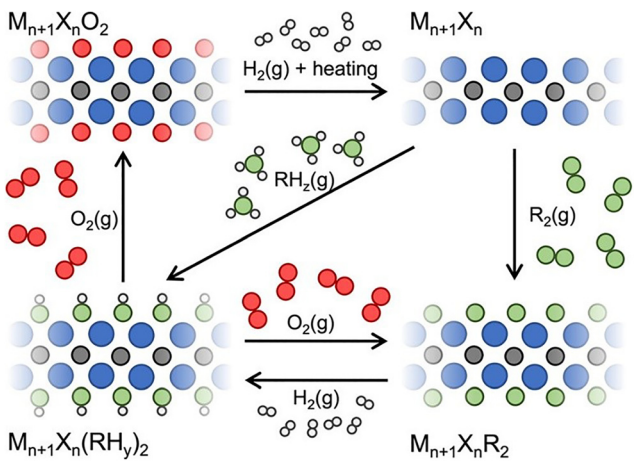

Fig. 5 Reaction pathways for MXenes functionalization. [Fig. 5 adapted with permission from ref. 76 Copyright © 2021 American Chemical Society].

$$M_{n+1}X_n + R_2\,(g) \rightarrow M_{n+1}X_nR_2 \quad (7)$$

$$M_{n+1}X_n + 2RH_z\,(g) \rightarrow M_{n+1}X_n(RH_y)_2 + (z\text{–}y)H_2 \quad (8)$$

$$M_{n+1}X_n(RH_y)_2 + 0.5yO_2\,(g) \rightarrow M_{n+1}X_nR_2 + yH_2O \quad (9)$$

$$M_{n+1}X_n(RH_y)_2 + O_2\,(g) \rightarrow M_{n+1}X_nO_2 + R_2 + yH_2 \quad (10)$$

$$M_{n+1}X_nR_2 + yH_2\,(g) \rightarrow M_{n+1}X_n(RH_y)_2 \quad (11)$$

In eqn (6)–(11), R_2 and RH_z represent diatomic gases and hydrides, respectively.

Multiple pathways endow the synthesized MXenes with extremely flexible surface engineering potential. Moreover, the stability of $M_n + 1X_nR_2$ varies depending on the type of R. It is predicted that replacing –F with –O is thermodynamically favorable.[74] In practice, as-prepared T_x like –F and –OH are relatively labile, in contrast to the more stable –O terminations, which often become dominant in MXenes engineered for applications such as energy storage.[76] This variation in stability, coupled with the controllable composition of T_x, opens pathways for deliberate property tuning. For example, post-synthetic treatments like thermal annealing can selectively remove less stable –F and –OH, thereby enriching the surface with more robust –O terminations—a process shown to enhance electrochemical performance by improving electrical conductivity and active site accessibility.[38,78]

In essence, MXenes surface chemistry is inherently dynamic. While this susceptibility to ambient degradation complicates storage and handling, the very same chemical lability enables precise functionalization. By strategically modulating the type and ratio of surface T_x, key properties such as oxidation resistance and electronic structure can be tailored for specific applications. This tunability is typically achieved through two primary approaches: *in situ* synthesis and post-synthetic treatment.

3.3. Analytical characterization techniques

Analytical characterization techniques have been instrumental in both qualitatively and quantitatively modulating the T_x of MXenes. However, the characterization of T_x remains challenging due to the complex chemical composition, low atomic mass, and high susceptibility to surface contamination.[7] Therefore, an integrated multi-technique approach is essential to obtain a comprehensive understanding of their structure and properties.[79]

3.3.1. X-ray photoelectron spectroscopy (XPS). XPS is one of the most powerful and widely used techniques for identifying the elemental composition and chemical states of surface T_x on MXenes. Its particular strength lies in the discrimination of oxygen-containing species on MXenes surfaces.[80,81] The O 1s spectrum of MXenes can typically be deconvoluted into five components: the peak at the lowest binding energy (~529.9 eV) is attributed to TiO_2, followed by peaks at ~531.2 eV and ~532.0 eV, assigned to C–Ti–O and C–Ti–OH species, respectively. Peaks at ~533.8 eV and ~535.0 eV are commonly assigned to adsorbed water and aluminum oxide contaminants, respectively.[80] The presence of single peaks in the Cl 2p and F 1s regions in thoroughly washed MXenes is generally interpreted as evidence of terminal –Cl and –F.[81]

In the study by Li *et al.*, the T_x of $Ti_3C_2T_x$ MXenes synthesized *via* molten salt etching were quantitatively analyzed.

 This journal is © The Royal Society of Chemistry 2026

From the XPS survey spectra, the atomic percentages of Ti, C, Cl, and O were determined, revealing the content of oxygen-termination and chlorine-termination group. This led to the derived composition of $Ti_3C_{1.94}Cl_{0.77}O_{1.71}$.[82] Furthermore, high-resolution XPS analysis with peak deconvolution allowed the identification of specific bonding states, such as Ti–O, Ti–OH, Ti–O_x, and adsorbed H_2O. The relative contents of these species were quantitatively assessed based on the corresponding peak-area ratios, providing detailed insights into the surface termination distribution.[83]

Despite its strengths in identifying T_x species, the information depth of XPS is typically 5–10 nm, while a monolayer MXene is only about 1–3 nm thick.[84,85] Consequently, the collected signal originates not only from the surface T_x but also from the bulk of MXenes flakes, as well as intercalated species such as cations, adsorbed H_2O, oxides, and etching residues, which complicates the accurate quantification of the T_x.[80,86]

3.3.2. Nuclear magnetic resonance (NMR) spectroscopy. NMR spectroscopy effectively complements XPS for analysing MXenes surface functionalization, offering high specificity and quantitative capabilities for T_x like –OH, –F, and –O by probing nuclei such as ^1H, ^{19}F, and ^{13}C non-destructively.[87–90]

Michael A. Hope *et al.*[66] employed NMR spectroscopy to probe the T_x of $Ti_3C_2T_x$ MXenes synthesized by two methods. ^1H NMR of $Ti_3C_2T_x$ revealed –OH terminations at 18.6 ppm (HF-etched) and 12.5 ppm (LiF–HCl etched), with interlayer H_2O at 6.5 ppm (Fig. 6(a)), while ^{19}F NMR showed –F signals at 227 ppm and 255 ppm, alongside impurities AlF_3 and TiF_3 (Fig. 6(b)). Quantitative analysis further yielded compositions like $Ti_3C_2(OH)_{0.12}F_{0.8}O_{0.54}$ (HF-etched) and $Ti_3C_2(OH)_{0.06}F_{0.25}O_{0.84}$ (LiF–HCl etched), underscoring minor –OH presence and synthesis-dependent chemistry of T_x (Fig. 6(c)).

Recently, Sanjay Sunny *et al.*[91] employed NMR spectroscopy to investigate the correlation between T_x of Ti_3C_2 MXenes and the formation of the solid electrolyte interphase (SEI). Their study highlights that T_x significantly influence the characteristics of the SEI layer. For instance, the presence of –O in MXenes synthesized *via* the molten salt etching method promotes the generation of a greater amount of Li_2CO_3 and alkyl carbonates. The NMR analysis confirmed that the SEI formed on these MXenes is predominantly thick and Li_2CO_3-rich. NMR spectroscopy, by revealing the evolution of surface terminations, has proven to be a powerful tool for characterizing advanced MXene-based catalysts and energy storage devices.[90]

3.3.3. Thermogravimetric analysis. Thermogravimetric analysis (TGA) serves as a powerful technique to complement the characterization of MXenes T_x by providing critical information on their thermal stability and composition.[92] By monitoring mass changes under controlled heating programs, distinct decomposition steps can be detected, corresponding to the loss of intercalated water, the removal of less stable T_x (*e.g.*, –F, –OH), and the oxidation of the MXenes framework.[93] Coupling TGA with mass spectrometry (TG-MS) further enhances this analysis by identifying the specific temperatures at which these processes occur, thereby offering semi-quantitative insights into the relative abundance of different T_x species (Fig. 7(a) and (b)).[38] For the surface engineering of MXenes, thermal analysis is therefore an excellent method for optimizing processing parameters and elucidating underlying reaction mechanisms.

3.3.4. Neutron scattering. Neutron total scattering, combined with pair distribution function (PDF) analysis, is a powerful technique for characterizing the surface functional groups of MXenes, such as $Ti_3C_2T_x$. The unique sensitivity of neutrons to light atoms, especially hydrogen, allows the technique to detect and quantify hydrogen-containing –OH terminations, which are often difficult to resolve with X-rays.[94]

In summary, T_x on MXenes is formed *in situ* during synthesis and can be further modulated. Their atomic arrangement is well-

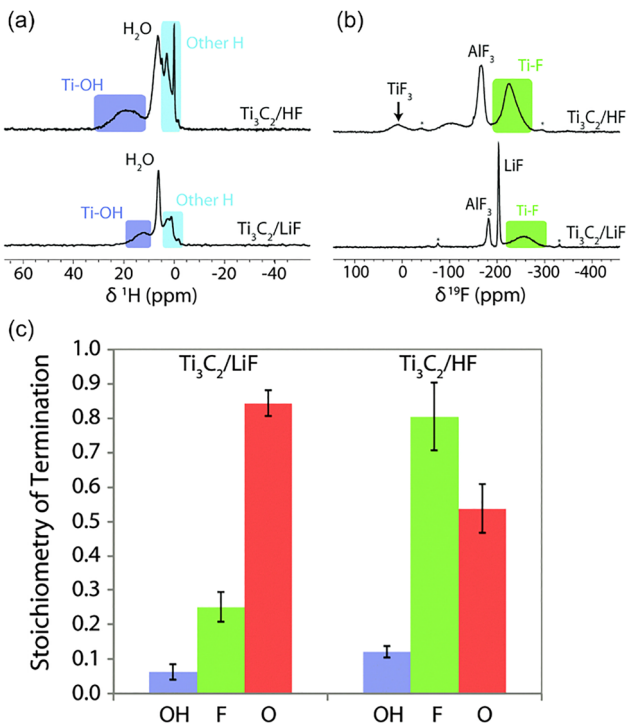

Fig. 6 (a) ^1H NMR, and (b) ^{19}F NMR of HF and LiF–HCl synthesized Ti_3C_2 MXenes, and (c) composition of the $Ti_3C_2T_x$ surface T_x of HF and LiF–HCl synthesized Ti_3C_2 MXenes, per Ti_3C_2 formula unit, *i.e.*, $Ti_3C_2(OH)_xF_yO_z$. [Fig. 6 adapted with permission from ref. 66 according to CC-BY 3.0. Copyright © 2016 Royal Society of Chemistry].

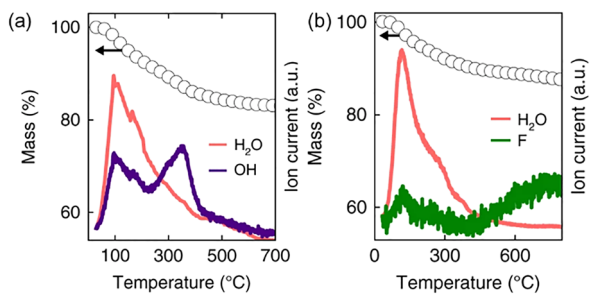

Fig. 7 (a) TGA-MS of Ti_3CNT_x showing de-intercalation of H_2O and –OH, (b) TGA-MS of $Ti_3C_2T_x$ showing de-intercalation of H_2O and –F. [Fig. 7 reproduced with permission from ref. 38 according to CC-BY 4.0. Copyright © 2019 Springer Nature Publishing].

defined, showing a preference for thermodynamically stable FCC and HCP sites. Deciphering their complex and mixed chemistry requires a combination of spectroscopic, microscopic, and computational methods—a foundational step toward their targeted engineering for catalysis and energy devices applications.

4. Engineering the surface functional groups of MXenes

Precise control over T_x of MXenes is pivotal for tailoring their properties for specific applications. The formation and evolution of these T_x exhibit a high degree of tunability, providing a versatile foundation for surface engineering. Generally, the engineering strategies can be categorized into two main approaches: *in situ* control during the synthesis process and post-synthetic modification of as-prepared MXenes. This section summarizes and discusses these surface functionalization strategies, further elaborated by classifying them according to the type of introduced functional groups.

4.1. *In situ* T_x engineering during synthesis

The initial composition of T_x on MXenes surfaces is predominantly determined by the synthesis conditions. By carefully selecting the etchant and reaction medium, specific T_x can be preferentially introduced.

4.1.1. Engineering –F-rich terminations. When HF was employed as the etchant for precursor MAXs phases, the resulting MXenes were rapidly passivated by HF or F^- present in the etching solution (eqn (2)). Studies have shown that the concentration of HF determines the surface fluorination degree of freshly prepared MXenes. For instance, when 5 wt% HF was used, the –F content on freshly prepared $Ti_3C_2T_x$ MXenes reached 15.85 at%. Increasing the HF concentration to 10 wt% raised the –F content to 19.93 at%, and at 30 wt% HF, it further increases to 27.51 at%.[65,95]

However, the upper limit of HF concentration in aqueous solutions is approximately 50 wt%, beyond which water introduces oxygen-containing T_x that occupy surface sites on MXene, hindering further enhancement of the surface –F content. To achieve higher –F functionalization, Varun Natu *et al.* adopted an alternative approach using anhydrous polar solvents, such as propylene carbonate (PC), acetonitrile (ACN), and *N*,*N*-dimethylformamide (DMF), to dissolve NH_4HF_2 as the etchant. This method enabled the synthesis of $Ti_3C_2T_x$ MXene with a notably high surface –F content of 70%, with the remaining 30% consisting of oxygen-containing T_x (–O/–OH). This represents the highest surface –F content ever reported for MXenes.[72]

4.1.2. Engineering –halogen-rich terminations. Engineering –halogen-rich terminations, particularly with heavy halogen T_x (–Cl/–Br/–I), presents a significant avenue for tuning MXene properties distinct from fluorine. These T_x can be achieved through various emerging methods such as Lewis acid etching and electrochemical etching.[96]

The molten salt etching approach enables the synthesis of MXenes with well-defined halogen-rich T_x, as illustrated in Fig. 8(a). This method typically employs Lewis acidic molten salts (*e.g.*, $FeCl_3$, $CuCl_2$, and $CdBr_2$) at elevated above 500 °C to etch the A-layer from the MAXs phase.[82,98] The mechanism initiates with the direct reaction between the molten salt and the MAXs phase, where the Al were selectively extracted, and the exposed transition metal atoms on the nascent MXenes surface were simultaneously passivated by Cl^- or Br^- from the melt. This process results in the formation of phase-pure MXenes with uniform halogen T_x, such as $Ti_3C_2Cl_2$, and $Ti_3C_2Br_2$. These materials, especially –Br functionalized $Ti_3C_2Br_2$, not only endow these MXenes with unique characteristics but also serve as a stable and versatile platform for further functionalization, enabling subsequent surface exchange reactions to access a broader range of T_x (Fig. 8(a)).[62]

In recent years, novel –halogen engineering methods during synthesis, such as electrochemical etching and halogen etching, have continued to expand the toolkit for producing MXenes with tailored surface functionalities. Electrochemical etching utilizes electrochemical reactions to selectively remove the A-layer element from the parent MAXs phase (Fig. 8(b), eqn (12)) while allowing precise control over the T_x of the resulting MXenes (eqn (3)–(5)), thus obtaining $Ti_3C_2Cl_2$ with good crystallization and uniformly functionalization by –Cl (Fig. 8(c)–(e)).[97,99]

$$Ti_3AlC_2 + 3Cl^- - 3e^- \rightarrow Ti_3C_2 + AlCl_3 \qquad (12)$$

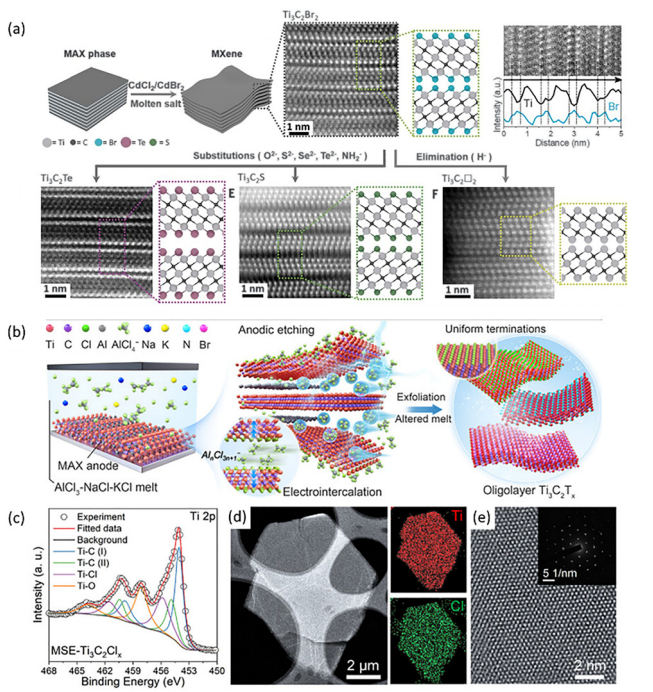

Fig. 8 Schematic illustrations of *in situ* surface T_x engineering for MXene synthesis: (a) molten salt etching, (b) electrochemical etching, (c) Ti 2p XPS spectrum, (d) TEM image with Ti and Cl elemental mapping, and (e) HRTEM image with SAED pattern of $Ti_3C_2Cl_x$. [(a) adapted with permission from ref. 62 Copyright © 2020, The American Association for the Advancement of Science. (b)–(e) Adapted with permission from ref. 97 Copyright © 2025 Wiley-VCH GmbH].

This journal is © The Royal Society of Chemistry 2026

By varying the electrolyte composition, the surface T_x can be effectively tuned.[100,101] For instance, $Ti_3C_2T_x$ MXenes with readily exfoliatable tunable –Cl/–Br/–I T_x have been successfully prepared from Ti_3AlC_2 at 170 °C *via* an anodic etching approach in a chloroaluminate molten salt.[97]

Recently, halogen molecules have been reported for MXenes synthesis. For instance, Shi *et al.* demonstrated the etching of Ti_3AlC_2 using I_2 in CH_3CN, yielding iodinated $Ti_3C_2I_x$:[63]

$$Ti_3AlC_2 + (x + 3)/2\ I_2 \rightarrow Ti_3C_2I_x + AlI_3 \quad (13)$$

Subsequent studies have further shown that halogens (Br_2, I_2, ICl, IBr) in anhydrous media are capable of synthesizing MXenes and successfully introducing the corresponding heavy halogen T_x:[102]

$$Ti_3AlC_2 + 3.5Br_2 + C_6H_{12} \xrightarrow{\text{Dark}} C_6H_{11}Br + Ti_3C_2Br_2 + AlBr_3 + HBr \quad (14)$$

$$Ti_3AlC_2 + 3.5I_2 + C_6H_{12} \xrightarrow{\text{Dark}} C_6H_{11}I + Ti_3C_2I_2 + AlI_3 + HI \quad (15)$$

4.1.3. Engineering–oxygen-containing terminations. Oxygen-containing T_x, primarily –OH and –O, are among the most prevalent and widely studied T_x on MXenes. As mentioned in Section 4.1.1, during the synthesis of MXenes, oxygen-containing T_x exhibit significant competition with –F. Therefore, synthesis strategies specifically target or favor the formation of –OH/–O rich surfaces generally require a fluoride-free or low-fluoride environment.

Tengfei Li *et al.* reported a NaOH-assisted hydrothermal route for MXene synthesis. Under hydrothermal conditions (270 °C, 27.5 M NaOH), Al was selectively etched from Ti_3AlC_2. As illustrated in Fig. 9, Al atoms located at the edges of Ti_3AlC_2 were first oxidized to aluminum oxides/hydroxides, which subsequently dissolved in the alkaline medium. This exposure of Ti atoms led to their immediate passivation by –OH or –O. The etching proceeds until all Al was oxidized and dissolved, ultimately yielding a uniform –OH/–O-terminated MXene surface.[69] Following this rationale, a range of other bases, including KOH and hydrazine, have also been demonstrated as effective fluoride-free etchants for the synthesis of MXenes with –OH/–O rich surface.[103,104]

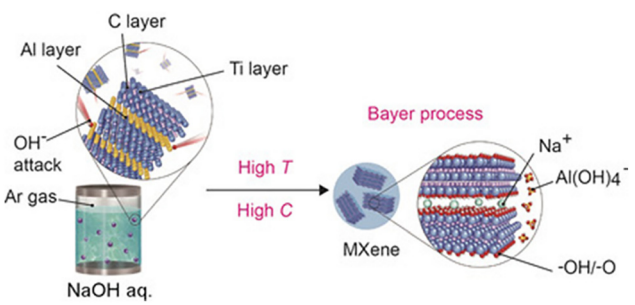

Fig. 9 Schematic illustrations of alkali (NaOH) etching. [Fig. 9 adapted with permission from ref. 69 Copyright © 2018 Wiley VCH Verlag GmbH & Co. KGaA, Weinheim].

UV-assisted etching is another fluorine-free route that involves the use of a photocatalyst, where UV irradiation induces the etching process. The underlying mechanism relies on the high energy of UV light to activate reactive species in the system, thereby promoting the selective removal of the A-layer element from the MAXs phase. For example, –O-rich Mo_2CT_x MXenes was synthesized from a non-MAXs phase Mo–In–C precursor through a UV-assisted safe etching process that selectively removed indium, followed by ultrasonic exfoliation.[105] In another case, –OH/–O-rich mesoporous Mo_2C MXene was successfully obtained within hours *via* UV-induced selective etching of bulk Mo_2Ga_2C ceramic.[106]

Yu Hao *et al.* have focused on reducing the HF associated with etching synthesis while optimizing the structure and surface of MXenes through the use of HF alternatives.[107] Recent innovations continue to refine the control over –OH-rich terminations.[71] In one notable approach, they developed a polyol-assisted solvothermal etching strategy utilizing a minimized (stoichiometric) amount of $NaBF_4$ combined with polyol-based etchants such as glycerol, erythritol, and xylitol. Due to the –OH-rich synthesis environment and the near-stoichiometric use of fluorine during etching, the resulting MXenes exhibited a significantly reduced –F T_x content, only 14–22% of that in commercially available MXenes. This reduction provided more adsorption sites for –OH T_x, thereby successfully yielding five types of –OH-rich MXenes through surface engineering of the etching process. This approach highlights the potential of solvent choice in directing surface chemistry towards desired T_x.

4.1.4. Engineering other terminations. The pursuit of MXenes with tailored surface chemistry extends beyond the common –F, –halogen, and –O/–OH. Recent advances in *in situ* synthesis strategies have unlocked pathways to introduce a diverse array of other T_x, notably –S, –Se, –Te, and –NH. A pivotal foundation for accessing these T_x is the availability of –Br-terminated MXene intermediates, particularly those synthesized *via* the molten salt etching method discussed in Section 4.1.2.

As illustrated in Fig. 8(a), the initial molten salt etching step yields $Ti_3C_2Br_2$. These –Br terminated surfaces are not merely end products but serve as versatile and reactive platforms for subsequent *in situ* anion exchange. The halogen atoms, being relatively good leaving T_x, can be readily substituted by other anions in a second molten salt bath. For instance, by reacting $Ti_3C_2Br_2$ with various anionic precursors (Li_2S, Li_2Se, Li_2Te) or $NaNH_2$ in a second molten salt bath, –Br were directly replaced, leading to the formation of $Ti_3C_2T_x$ (T_x = –S, –Se, –Te, and –NH) without the need for post-synthetic processing.[62] This strategy effectively decouples the etching and functionalization stages, providing exceptional control and purity for synthesizing MXenes with these otherwise challenging-to-achieve T_x.

On the basis of etching methods using NaOH or KOH (Section 4.1.3.), subsequently, it has been demonstrated that a tetramethylammonium hydroxide (TMAOH) solution can also act as a fluorine-free etchant to prepare MXenes.[108] Fig. 10

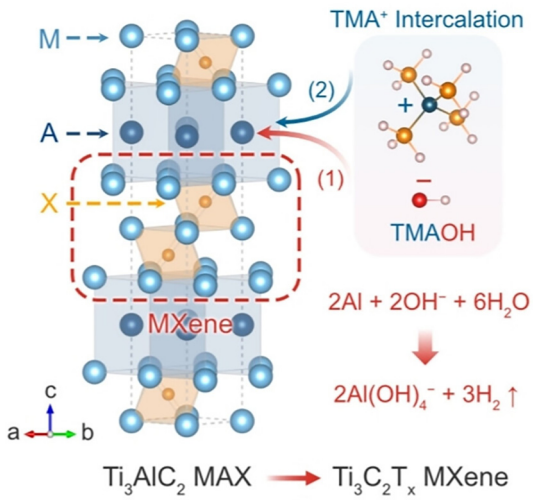

Fig. 10 Schematic illustrations of TMAOH etching. [Fig. 10 adapted with permission from ref. 108 Copyright © 2024 Wiley-VCH GmbH].

schematically illustrates the etching of Al layers from Ti_3AlC_2 MAXs phases to produce MXenes with oxyanion-type terminations. The corresponding etching reaction is:

$$2Al + 2OH^- + 6H_2O \rightarrow 2Al(OH)_4^- + 3H_2 \quad (16)$$

The use of TMAOH as an etchant introduces a novel dimension. As shown in Fig. 10, the generated $Al(OH)_4^-$ anions do not merely act as etching by-products. Instead, they *in situ* passivate the newly exposed titanium atoms on the MXene surface. This process results in MXenes terminated with $-Al(OH)_4^-$.

4.1.5. Summary of *in situ* T_x engineering. The *in situ* functional group engineering of MXenes during synthesis enables precise tailoring of T_x by modulating etchants and conditions. Table 1 summarizes different reported methods, etchants used, and resulting MXenes T_x for *in situ* functional groups engineering during synthesis.

The T_x composition of MXenes is dynamically adjustable during synthesis. A decrease or loss of one T_x is inherently accompanied by an increase in others. Leveraging this characteristic, along with rational synthesis design and careful selection of solvents and etchants, paves the way for developing environmentally benign, non-toxic, and efficient methods that integrate synthesis with surface regulation. Collectively, these strategies underscore the power of *in situ* synthesis design. By leveraging reactive halogen-terminated intermediates or by innovating within established etching environments, researchers can directly incorporate a wide spectrum of functional groups, significantly expanding the chemical diversity and application potential of MXenes from the point of synthesis.

4.2. Post-synthetic T_x engineering

As-prepared MXenes typically contain a mixture of T_x.[4,110] Post-synthetic functionalization methods are often required to precisely tailor their surface properties. This refers to the re-engineering of the MXenes surface after its formation, which can be broadly categorized into several principal approaches based on the treatment method: thermal treatment, chemical substitution, and plasma/special treatments.

4.2.1. Thermal treatment. Thermal treatment is a versatile and widely used post-synthetic strategy for adjusting the composition and ratio of T_x in MXenes. Heat treatment serves as a simple yet effective post-synthetic strategy, bases on the differences in thermal stability among various T_x. Studies have shown that –F and –OH are relatively unstable, whereas –O exhibits higher stability. Annealing at low to moderate temperatures under an inert atmosphere or in vacuum can selectively remove the less stable –F and –OH, thereby achieving defunctionalization of fluorine and enriching the MXene surface with more stable –O terminations.[111]

Table 1 *In situ* functional groups engineering during synthesis: methods, etchants, and functional groups of MXenes

Methods	Etchant	T_x	Key outcomes (✓) and limitation (✗)	Ref.
HF etching	30 wt% HF	**27.51 at% –F**, less –O, and –OH	✓ High –F content. ✗ Highly toxic etchant.	65
Water-free etching	Polar organic solvents + NH_4HF_2	**70% –F**, less –O, and –OH	✓ Highest reported –F content. ✗ Flammable solvents were used.	72
Lewis acid etching	$CdCl_2$, or $CdBr_2$	**–Cl/–Br**	✓ Phase-pure MXenes with uniform halogen T_x. ✗ High temperature required.	62
Electrochemical etching	$AlCl_3$–NaCl–KCl	**–Cl/–Br**	✓ Crystallized, uniformly functionalized MXenes. ✗ High temperature required.	97
Halogen molecule etching	Halogen molecule	**–Cl/–Br/–I**	✓ Iodinated MXenes. ✗ Toxic reagents; side reactions possible.	63 and 102
Alkali etching	27.5 M NaOH	**–O, and –OH**	✓ Uniform –O/–OH-terminated MXenes. ✗ Slow kinetics.	69
UV-assisted etching	UV light	**–O**	✓ –O-rich Mo_2CT_x. ✗ Long processing time, limited scalability.	106
Polyol-assisted solvothermal etching	Polyol solvents + $NaBF_4$	**–OH-rich**, –O, less –F or –F-free	✓ Reduced –F content (14–22% *vs.* commercial) with increased –OH sites. ✗ purification needed.	71
Lewis acid etching and T_x exchange	$CdCl_2$, or $CdBr_2$	**–Te/–S/–NH/–Se**	✓ Versatile –S/–Se/–Te/–NH functionalization. ✗ Multi-step process.	62
TMAOH etching	25% TMAOH	**$-Al(OH)_4^-$, –O, and –OH**	✓ $-Al(OH)_4^-$ oxyanion-terminated MXenes. ✗ Highly toxic etchant.	108

This journal is © The Royal Society of Chemistry 2026

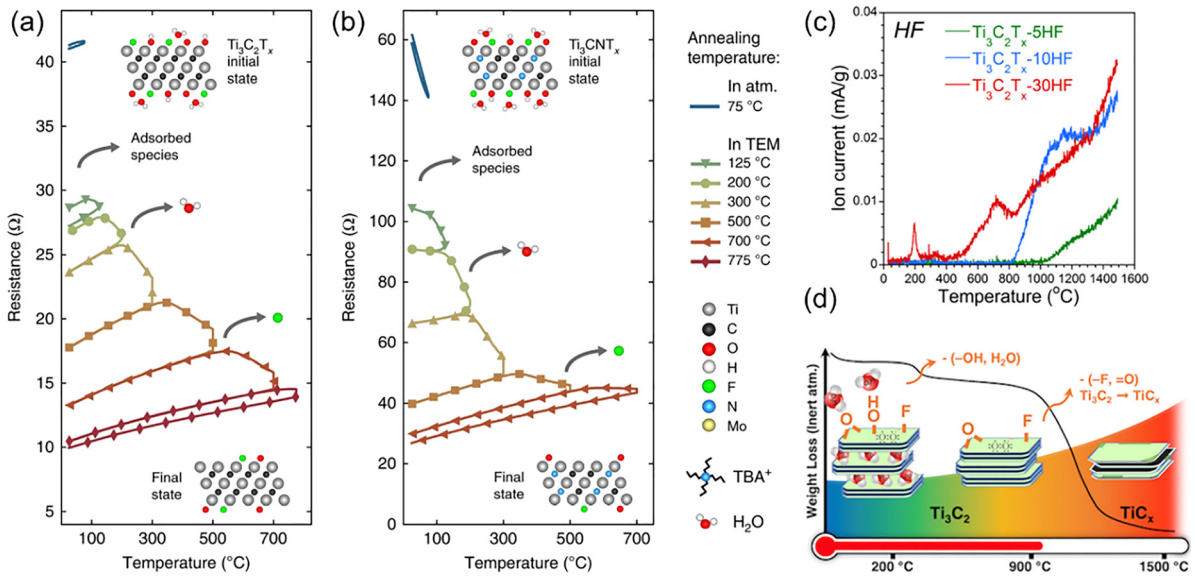

Fig. 11 Schematic diagram of the *in situ* vacuum annealing resistance properties and T_x evolution of (a) $Ti_3C_2T_x$, and (b) Ti_3CNT_x. In all cases, the resistance decreased during annealing, the cooling curves were always lower than the heating curves. During the annealing process, –OH is unstable above 200 °C, and the defluorination functionalization of $Ti_3C_2T_x$ and Ti_3CNT_x occurs above 500 °C. (c) Mass spectrometry analysis of MXenes heat treatment process (20/HF), (d) surface T_x and phase evolution of MXenes heat treatment process. [(a) and (b) Reproduced with permission from ref. 38 Copyright 2019, Springer Nature Publishing. (c) and (d) Adapted with permission from ref. 109 Copyright © 2019, American Chemical Society].

According to L. Hart *et al.*, annealing $Ti_3C_2T_x$ and Ti_3CNT_x in vacuum from 300 °C to 775 °C led to significant desorption of –F (Fig. 11(a) and (b)).[38] Research by Mykola Seredych *et al.* further revealed that –F is primarily released in the form of HF at elevated temperatures, with defluorination continuing up to about 1500 °C (Fig. 11(c)). However, beyond 740 °C, the $Ti_3C_2T_x$ MXenes began to degrade and transform, releasing CO; this degradation accelerated between 830 °C and 850 °C, accompanied by further CO evolution, indicating the transformation of the MXenes structure into cubic TiC (Fig. 11(d)).[109] Based on existing studies, although heat treatment can promote partial desorption of –F from the MXenes surface, achieving complete defluorination solely *via* thermal treatment remains extremely challenging due to the substantial bonding energy between –F and the MXene matrix, as well as the need to prevent structural degradation of the MXene.

Although replacing –F and –OH with –O is thermodynamically favorable, achieving this substitution requires overcoming kinetic barriers.[76] In this regard, some advanced methods have been developed based on traditional annealing processes.[38,112–114]

As shown in Fig. 12(a), Halim *et al.*[115] developed a two-step procedure for the treatment of $Ti_3C_2T_x$ MXenes, in which the materials were first treated with NaOH solution to partially remove –F groups, followed by vacuum annealing at 550 °C to further eliminate residual –F and –OH. This sequential approach effectively achieves dual defunctionalization of both –F and –OH, resulting in a surface predominantly functionalized by –O groups (Fig. 12(b)). Along similar lines, a two-step method involving a NaOH/NaI molten salt treatment followed by thermal annealing was employed by Zhang *et al.*[113] The molten salt step displaces surface –F terminations with –OH, and the subsequent annealing at 380 °C fully converts these –OH into –O terminations. This novel route enables the preparation of pure –O-terminated MXenes while maintaining structural integrity.

–O-terminated MXenes are not the final products obtained from thermal treatment; rather, heating in specific atmospheres enables more targeted outcomes. A key strategy for engineering bare MXenes involves the thermal treatment of –O-terminated MXenes in a H_2 atmosphere. Bare MXenes, while theoretically established, faces significant challenges in experimental stability and practical application due to its high surface reactivity. Achieving complete removal of surface T_x typically requires post-synthetic surface engineering.[54] Current preparation strategies therefore focus on eliminating T_x as thoroughly as possible to expose the underlying $M_{n+1}X_n$ skeleton. One effective route, illustrated in Fig. 5, involves the thermal treatment of –O-terminated MXenes in a H_2 atmosphere to drive de-functionalization of the –O. This approach was experimentally validated by Persson *et al.*[111] As shown in Fig. 13(a)–(c), as-prepared $Ti_3C_2T_x$ MXenes was first thermally treated to remove –F terminations, followed by H_2 exposure to eliminate residual –O groups. The corresponding EELS spectra in Fig. 13(d) show a distinct decrease in the oxygen signal, confirming the successful removal of surface –O and the formation of bare-Ti_3C_2. Building on this methodology, Vladislav Kamysbayev *et al.*[62] extended the pathway by demonstrating that LiH can be used to achieve complete de-functionalization of $Ti_3C_2Br_2$ and Ti_2CBr_2 at 300 °C, yielding bare MXenes.

4.2.2. Chemical substitution. Chemical substitution encompasses methods where MXenes are contacted with various chemical agents to replace existing T_x or introduce new T_x

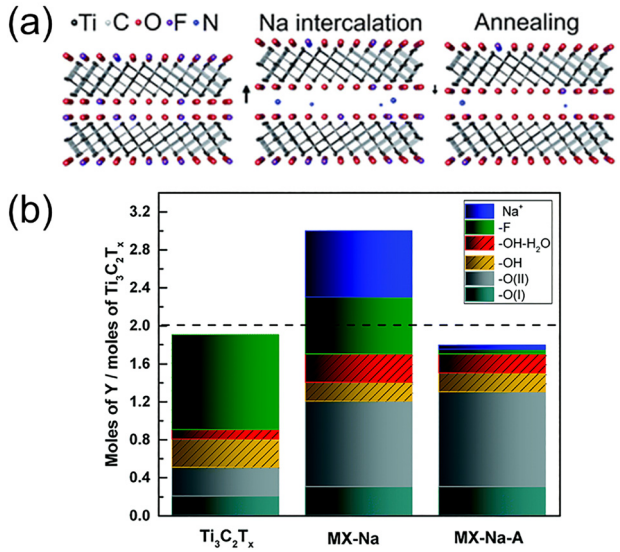

Fig. 12 Schematic diagram of the (a) principle, and (b) effect of two-step thermal treatment. [(a) Adapted with permission from ref. 115 according to CC-BY 3.0. Copyright © 2018, Royal Society of Chemistry].

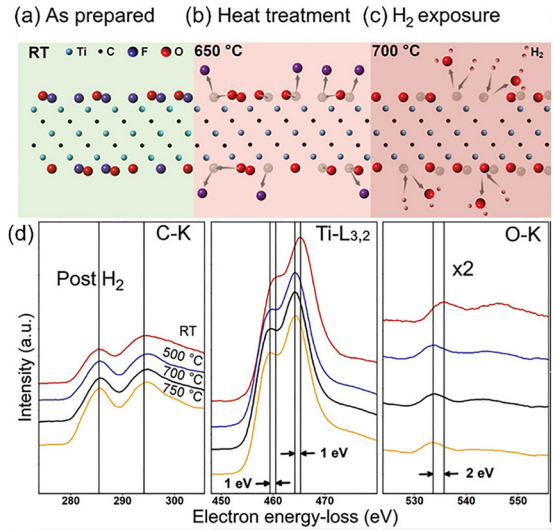

Fig. 13 (a)–(c) Schematic diagram of the atomic structure of MXene in the surface engineering, (d) EELS spectra of $Ti_3C_2T_x$ flakes after exposure to 8 mbar H_2 gas at RT, 500, 700, and 750 °C for 0.5 h. [Fig. 13 adapted with permission from ref. 111 Copyright © 2018 WILEY-VCH].

through displacement reactions, hydrolysis, or other chemical processes.

T_x on MXenes can undergo dynamic exchange driven by differences in their thermodynamic stability. For instance, oxygen-containing terminations are more stable than –F.[118] Thus, under prolonged ambient exposure, –F was gradually replaced by –O/–OH.[72] In the presence of O_2 and/or H_2O exposure, MXene–OH exhibits superior thermodynamic stability compared to MXene–F, thereby enabling the substitution/displacement reaction.[118,119] In a pioneering study, Peng *et al.*[120] treated $Ti_3C_2T_x$ MXenes with a NaOH solution. The alkaline

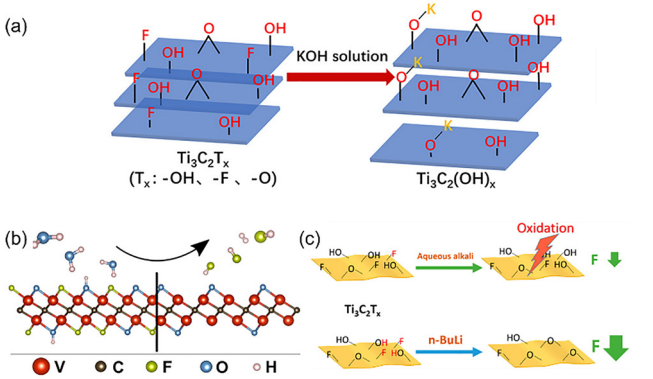

Fig. 14 Schematic diagram of chemical substitution methods: (a) alkali treatment, (b) gas-phase hydrolysis, and (c) strong base treatment. [(a) Adapted with permission from ref. 116 Copyright © 2022, American Chemical Society. (b) Reproduced with permission from ref. 117 Copyright © 2022, American Chemical Society. (c) Adapted with permission from ref. 56 Copyright © 2019, American Chemical Society].

treatment promoted partial defluorination and increased the –OH content, successfully achieving surface hydroxylation (Fig. 14(a)):[116]

$$Ti_3C_2F_2 + 2OH^-\ (aq) \rightarrow Ti_3C_2(OH)_2 + 2F^-\ (aq) \quad (17)$$

Li *et al.*[121] treated $Ti_3C_2T_x$ MXenes with 1.8 mol L^{-1} KOH for 4 h. During this process, the –F content of $Ti_3C_2T_x$ decreased significantly, as –F was replaced by –OH, dropping from 14.89 wt% to 3.19 wt% (corresponding to 4.26 at%). This result surpasses the 6.08 wt% obtained by thermal treatment at 400 °C, while the alkaline environment helps preserve the structural integrity of MXenes during defluorination.

Alkaline treatment is easy to operate and has been widely used in subsequent research.[37,122–126] Nevertheless, conventional alkali treatment still does not achieve complete removal of –F.

To accelerate the removal of –F, Frode Håskjold Fagerli *et al.* developed a gas-phase hydrolysis method, in which V_2CT_x MXenes were thermally treated under a continuous flow of humidified argon. After hydrolysis between 300 and 500 °C, –F on the MXenes surface were nearly completely removed (Fig. 14(b)), as described by the following possible reactions:[117]

$$V_2CF_2 + 2H_2O\ (g) \rightarrow V_2C(OH)_2 + 2HF\ (g) \quad (18)$$

$$V_2CF_2 + 2H_2O\ (g) \rightarrow V_2CO_2 + 2HF\ (g) + H_2\ (g) \quad (19)$$

$$V_2CF_2 + H_2O\ (g) \rightarrow V_2CO + 2HF \quad (20)$$

However, the introduction of water vapor during this process also leads to oxidative degradation of MXenes at temperatures above 300 °C, exemplified by the following reaction:[117]

$$V_2CO_2 + H_2O\ (g) \rightarrow V_2O_3 + C + H_2\ (g) \quad (21)$$

In a subsequent study, a strong base, *n*-butyllithium (*n*-BuLi), was employed as both a strong nucleophile and reducing agent to replace –F with –O (Fig. 14(c)).[127] Compared

 This journal is © The Royal Society of Chemistry 2026

with common modifiers such as KOH, NaOH, and LiOH, this approach enables more efficient exchange of –F. Using optimized conditions, the –F content could be reduced to as low as 2 at% without observable structural damage to the MXenes, owing to the protective alkaline and reducing atmosphere.[56] However, even with the strong base strategy, complete defluorination of MXene has not yet been realized.

Cheng *et al.*[128] found that the –OH of alcoholic solvents can form hydrogen bonds with the –F and –OH groups on MXenes, enhancing the adsorption of these solvents on the MXenes surface. Further calculations revealed that the –OH of the alcohol tends to provide a H atom to the surface –O of MXene, while the remaining O forms a covalent bond with the surface Ti atoms (Fig. 15). This –OH-rich environment promotes the evolution of MXenes T_x toward –OH.[71] Compared with alkaline treatment, the alcohol treatment strategy not only enables surface –OH engineering, but also protects the structural integrity of MXenes during surface engineering, as the adsorbed alcohol molecules stabilize defect sites and shield them from attack by H_2O and/or O_2.[128] At present, alcohol treatment is also a mainstream MXene engineering –OH method.[129–131]

Similar to –OH, from a thermodynamic perspective, the functionalization of $–NH_x$ (amino) groups on MXene surfaces is essentially a process of reducing the system's free energy, primarily achieved through the formation of strong Ti–NH_x and replace –OH or –F. It has been reported that $–NH_x$ functionalization is typically carried out in aqueous solutions of amino sources at room temperature. Common amino sources include ammonia solution (NH_4OH), hydrazine monohydrate (HM), ethylenediamine (EDA), and monoethanolamine (MEA).[132,133] Specifically, in ammonia solution, the positively charged NH_4^+ ions attack and replace the negatively charged –OH groups, yielding MXene–NH_x and H_2O.[134,135] In contrast, HM, EDA, and MEA primarily replace the –F groups on MXenes. Wan *et al.* found that EDA treatment enabled 3.93% $–NH_2$ functionalization due to its stronger electron-donating character.[133] Overall, treatment with liquid-phase amino sources generally achieve only limited $–NH_2$ functionalization on MXenes.[136]

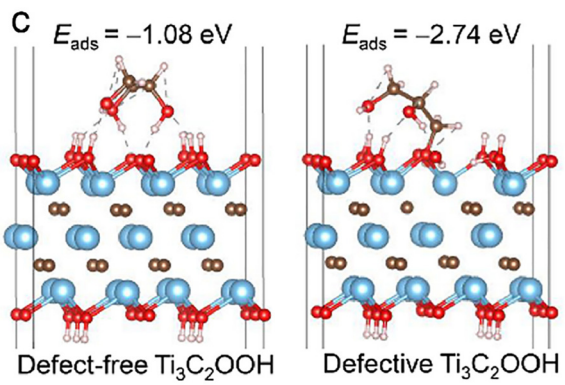

Fig. 15 Hydrogen bonding between glycerol molecules and MXene surface. [Fig. 15 adapted with permission from ref. 128 Copyright © 2023 Elsevier Inc.].

As shown in Fig. 8(a), Kamysbayev *et al.*[62] developed a two-step $–NH_2$-functionalization strategy. The process starts with the synthesis of a pure MXene–Br intermediate *via* a molten salt method. This MXene–Br was then subjected to a surface T_x-exchange reaction in a molten salt bath containing an NH_2^- precursor, leading to the formation of $–NH_2$-functionalized MXenes. The metal to T_x elemental ratios of the resulting MXene–NH closely matches the expected value, indicating near-ideal –NH-functionalization through this two-step route.

4.2.3. Plasma method. Plasma method primarily utilizes the sputtering effect of high-energy reactive O species (ROS) in the plasma to displace unstable surface atoms or weakly bonded T_x on MXenes, thereby selectively introducing stable –O groups onto their surface.[138] After plasma treatment, the surface –F and –OH are selectively cleaved and replaced by –O bonds, ultimately resulting in –O-functionalized MXenes (Fig. 16(a)).[137]

Furthermore, Hart *et al.*[78] combined thermal treatment with plasma processing by repeatedly performing vacuum annealing of MXenes to drive the defunctionalization of surface –F and –OH, followed by Ar + O_2 plasma treatment (Fig. 16(b)). This hybrid approach further increased the concentration of –O on the MXenes surface, achieving nearly complete –O-functionalization. The plasma method is particularly suitable for thermally unstable MXenes such as Ti_2CT_x. It enhances the –O content at temperatures as low as 200 °C while preserving the underlying structure of Ti_2CT_x intact.

4.2.4. Grafting method. The high specific surface area and the presence of native T_x on MXenes provide abundant reactive sites for introducing additional T_x or binding metal cations. The grafting technique enables direct modification of MXenes by leveraging its inherent –O, –OH, and –F T_x. For instance, H. Shin *et al.*[139] demonstrated that the amine groups of oleylamine (OAm) can bond with T_x (–O, –OH, and –F) and Ti atoms through hydrogen bonding and covalent Ti–N bonds,

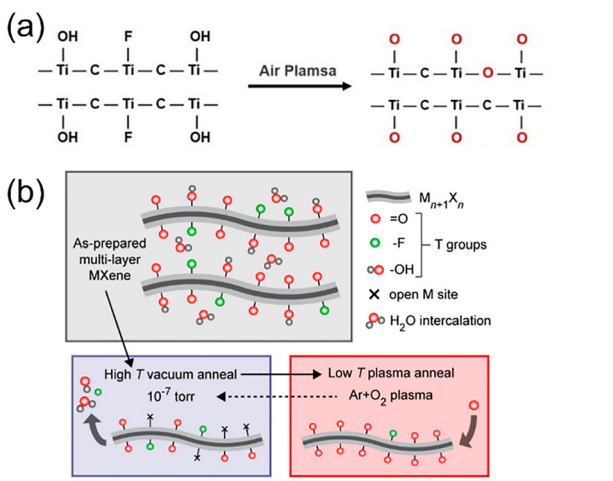

Fig. 16 Schematic diagram of: (a) plasma method, and (b) thermal treatment combined with plasma method. [(a) Adapted with permission from ref. 137 Copyright © 2024 Elsevier Inc. (b) Reproduced with permission from ref. 78 Copyright © 2022 American Chemical Society].

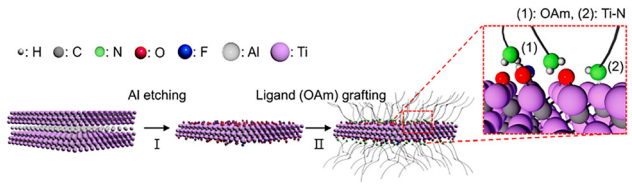

Fig. 17 The grafting process of oleylamine (OAm) and the schematic diagram of the bond between OAm and MXenes. [Fig. 17 adapted with permission from ref. 139 Copyright © 2023, American Chemical Society].

respectively. In a typical procedure, a dispersion of MXenes was mixed with an OAm solution and vigorously stirred at room temperature for 24 hours, resulting in successful grafting of OAm and producing –OAm–MXene, which exhibit a highly stable dispersed phase (Fig. 17). Similarly, novel T_x groups such as silane,[140] 4-nitrophenyl,[141] spiropyran,[142] and sulfonic-group[143] have been successfully grafted onto MXenes using this method, demonstrating the versatility of this method for modifying MXenes with diverse organic T_x.

However, the stability of these grafted materials, crucial for their performance in electrochemical applications, is governed by the strength of the organic–MXene bonds. Theoretical studies reveal that this bond strength is highly dependent on the intrinsic T_x of MXene. On bare or –OH-terminated surfaces, organic molecules can form strong chemical bonds (*e.g.*, Ti–O–C) with high adsorption energy, ensuring robust grafting. Conversely, on –F- or –O-terminated surfaces, interactions are primarily physical (van der Waals forces) with much weaker bonding.[144] Therefore, Ti–O–C bonds on reactive bare/–OH-terminated MXene are chemically stable, whereas physically adsorbed configurations on –F-/–O-terminated surfaces face a higher risk of dissociation or hydrolysis in battery electrolytes.

4.2.5. Summary of post-synthetic functional groups engineering. Table 2 summarizes the post-synthetic engineering strategies for MXene surface functional groups, systematically comparing the evolution pathways, advantages, and limitations of different engineering methods. The table clearly demonstrates that rational combination of processes enables high-purity and high-precision control over specific functional groups.

Based on the comprehensive review, the field of MXenes T_x engineering has evolved from simple modification towards sophisticated, multi-step strategies that enable precise control over termination species and purity. Combining two or more distinct surface treatment processes is highly effective for achieving tailored and purer surface terminations, surpassing the limitations of single-method approaches. This will become the future direction of surface functional group customization.

5. T_x-engineered MXenes for catalysis and energy applications

The tailored surface T_x of MXenes directly govern their performance in target applications by modulating key physicochemical properties. To provide a clear, application-oriented perspective, this section synthesizes the roles of various T_x by application domain. We first examine the pivotal roles of various T_x in photocatalysis (Section 5.1), focusing on their

Table 2 Post-synthetic functional groups engineering: methods, evolution of T_x, advantage and disadvantage

Strategy	Methods	Evolution of T_x	Advantage (✓) and limitations (✗)	Ref.
Thermal treatment	Heat treatment	Defunctionalization of –F.	✓ Simple. ✗ The structure of MXenes was disrupted.	38 and 109
	Heat treatment and H_2 exposure	Defunctionalization of –OH, –F, and –O.	✓ Implemented the defunctionalization of MXenes.	111
Chemical substitution	Gas-phase hydrolysis	–F was replaced by –O/–OH.	✓ Replace oxygen-containing T_x. ✗ The structure of MXene was disrupted.	117
	Alkali treatment	–F was replaced by –OH.	✓ Simple and feasible, MXenes structure was maintained.	120 and 121
	Strong base treatment	–F decreased to 2 at%.	✗ –F cannot achieve complete defunctionalization, unable to achieve the transition from –O to –OH	56
	Alcoholic solvents treatment	–F, and –O were replaced by –OH.	✓ Simple and easy to implement, while protecting the structure of MXenes	128 and 129
	Liquid phase method	–F, or –OH was replaced by $–NH_2$.	✗ Low degree of $–NH_2$-functionalization.	134 and 135
Plasma method	Plasma treatment	–F, and –OH were replaced by –O.	✓ Simple. ✗ The structure of MXene was disrupted.	38
Grafting method	Liquid phase method	Functionalization of organic T_x.	✓ Simple. ✗ Inorganic T_x is not applicable.	134, 135 and 139–143
Multi-step method	**Step 1:** Thermal treatment. **Step 2:** Plasma processing.	Nearly complete conversion of –F/–OH to –O.	✓ Mild temperature conditions suitable for low stability MXenes. MXenes structure was maintained.	78
	Step 1: $CdBr_2$ molten salt treatment. **Step 2:** $NaNH_2$ molten salt treatment.	**Step 1:** –Br functionalized. **Step 2:** –Br were replaced by $–NH_2$.	✓ Ideal $–NH_2$-functionalization. ✗ Requires MXene–Br as an intermediate.	62
	Step 1: NaOH/NaI molten salt treatment. **Step 2:** Thermal annealing.	**Step 1:** –F were replaced by –OH. **Step 2:** –OH were replaced by –O.	✓ This multi-step route enables the preparation of pure –O-terminated MXenes while maintaining structural integrity.	113

This journal is © The Royal Society of Chemistry 2026

influence on light absorption, charge carrier dynamics, and surface-mediated reactions. This is followed by an analysis of electrocatalytic processes (Sections 5.2 and 5.3), where T_x critically govern intermediate adsorption/desorption energetics, charge transfer kinetics, and operational stability. Finally, we explore energy storage and conversion devices (Section 5.4), in which T_x engineering is key to optimizing ion accessibility, redox activity, electrical conductivity, and interfacial stability. This integrated discussion aims to establish a coherent framework that connects specific T_x modifications to enhanced application performance, thereby guiding the rational design of MXenes for advanced catalysis and energy technologies.

5.1. Photocatalysis

Photocatalysis represents a pivotal technology for addressing global energy and environmental challenges. In this context, two-dimensional MXenes have emerged as a promising class of materials due to their exceptional electronic properties and tunable surface chemistry. MXenes serve as efficient co-catalysts and heterojunction components in photocatalytic systems, where the type of surface T_x critically influences the key processes, such as charge dynamics, surface reactivity, and stability.

5.1.1. –OH MXenes

5.1.1.1. Separation and transport of holes. The functionalization of MXene surfaces with –OH, yielding materials such as $Ti_3C_2(OH)_x$ and $Nb_2C(OH)_x$, profoundly alters their physicochemical characteristics and significantly enhances their photocatalytic performance. –OH functionalization enables targeted modulation of key MXene properties related to charge dynamics, primarily by optimizing electrical conductivity.[35,145] Theoretical calculations further indicate that –OH can modulate the Fermi level and work function, leading to improved interfacial charge transfer efficiency.[43,75,146]

Specifically, the introduction of –OH terminations significantly reduce the work function of MXenes. Ultraviolet photoelectron spectroscopy (UPS) and density functional theory (DFT) calculations indicate that the work function of $Ti_3C_2(OH)_x$ can be as low as 2.7–3.4 eV, which is substantially lower than that of other surface terminated counterparts (Fig. 18(a)).[53,147] This reduction raises the Fermi level closer to the conduction band minimum. When integrated with a semiconductor (*e.g.*, TiO_2, g-C_3N_4) to form a heterojunction, this low work function facilitates favorable band alignment. Consequently, a built-in electric field is established, directed from the MXene to the semiconductor, which effectively drives the migration of photogenerated holes toward the MXene layer (Fig. 18(b)).[147] This mechanism enables –OH-terminated MXenes to function as efficient hole-transport mediators.[148] For instance, the Cu/TiO_2@$Ti_3C_2(OH)_x$, Ag/Nb_2O_5@Nb_2CT_x, and A/R-TiO_2/$Ti_3C_2T_x$ composite exhibits a H_2 production rate markedly higher than that of a control sample without MXene (Fig. 18(c)).[53,147,149] This enhancement is attributed to the efficient extraction and confinement of photogenerated holes by the MXene, while electrons accumulate on the TiO_2 or reduction co-catalysts (*e.g.*, Ag), thereby prolonging the overall charge carrier lifetime and suppressing recombination (Fig. 18(b)).

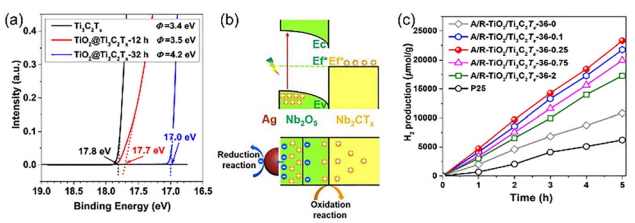

Fig. 18 (a) UPS spectra of $Ti_3C_2T_x$, and TiO_2@$Ti_3C_2T_x$, (b) schematic illustration of the charge separation and transfer on the interface of Ag/Nb_2O_5@Nb_2CT_x, (c) photocatalytic H_2 evolution rate of A/R-TiO_2/$Ti_3C_2T_x$. [(a) Adapted with permission from ref. 53 Copyright © 2018 Elsevier Ltd. (b) Adapted with permission from ref. 147 Copyright © 2021 Elsevier B.V. (c) Adapted with permission from ref. 149 Copyright © 2022 Elsevier B.V.].

5.1.1.2. Reaction activation and selectivity. –OH groups carry lone pair electrons, rendering the MXene surface Lewis basic. Critically, Bader charge analysis demonstrates that these Lewis basic sites can donate electron density to reactant molecules. This property is crucial for CO_2 reduction, as it significantly strengthens the chemical adsorption of CO_2. For instance, the adsorption energy of CO_2 on the BOB/Ti_3C_2–OH composite is as low as −2.05 eV (Fig. 19(a)). Furthermore, the presence of –OH groups lower the Gibbs free energy barrier for the critical first protonation step (CO_2 → *COOH) from 2.78 eV to 1.13 eV. This activation leads to a substantially increased CO production rate of 155.4 μmol g^{-1} h^{-1}. Beyond C1 products, –OH sites can also promote C–C coupling reactions. This is highlighted by the $Ti_2C(OH)_2$@g-C_3N_4 system, which achieves the high-selectivity reduction of CO_2 to ethanol with a notable yield of 784 μmol g^{-1} h^{-1}, underscoring the unique advantage of –OH–MXenes in steering product selectivity toward valuable multi-carbon (C_2^+) compounds (Fig. 19(b)).[129]

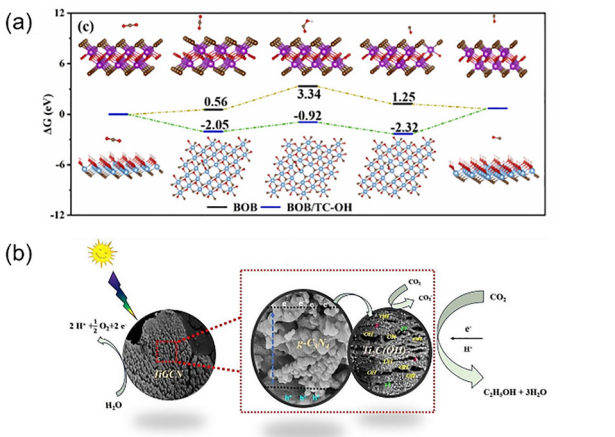

Fig. 19 (a) Calculated free energy diagram of CO_2 reduction intermediates in BOB and BOB composite hydroxyl MXene, and (b) schematic diagram of CO_2 photocatalytic reduction of Ti_2CT_x MXene@g-C_3N_4. [(a) Adapted with permission from ref. 126 Copyright © 2025 Elsevier B.V. (b) Adapted with permission from ref. 129 Copyright © 2024 Elsevier B.V.].

5.1.1.3. Accessibility of reactants. The hydrophilic nature of surface –OH improves the dispersibility of MXenes in aqueous reaction media, enhancing reactant accessibility to active sites.[150] This hydrophilicity also promotes water wetting and infiltration on the MXene surface, facilitating proton supply and interfacial mass transfer, which collectively boost reactant adsorption and photocatalytic efficiency. For example, the –OH-modified $Nb_4C_3T_x$ MXene@ZIS-OH sandwich structure photocatalyst achieved overall water splitting with H_2 and O_2 evolution rates of 53.8 and 26.7 μmol g^{-1} h^{-1} under visible light, demonstrating the key role of hydroxyl-induced surface hydrophilicity in enhancing reactant accessibility.[35]

5.1.2. –O MXenes

5.1.2.1. Separation and transport of electrons. Similar to –OH, –O also improve the conductivity of MXenes, thereby exerting a significant impact on photocatalytic hydrogen evolution reactions where MXenes act as co-catalysts.[38,151] DFT studies reveal that the –O termination upshifts the work function of MXenes, optimizing band alignment with semiconductors to enhance interfacial charge separation.[146] Additionally, it enables the material to behave as an excitonic insulator, where high exciton binding energy suppresses electron–hole recombination and prolongs carrier lifetime, thereby collectively boosting photocatalytic performance.[152]

Differential charge density (DCD) analysis (Fig. 20(a) and (b)) reveals that the –O groups exhibit strong electron affinity, serving as effective electron acceptors that promote electron transfer from metal oxide semiconductors (MOS) to MXene. This process optimizes interfacial charge distribution and enhances carrier separation efficiency.[153] Furthermore, the high work function and favorable band alignment of –O-terminated MXenes facilitate efficient electron separation at heterointerfaces.[156,157] The electron-extracting function of –O-functionalized MXenes in semiconductor heterostructures (Fig. 20(c) and (d)) is enabled by a Schottky barrier, which directs photogenerated electrons to MXene layers. This mechanism significantly boosts photocatalytic activity, achieving a H_2 yield of 14 342 μmol h^{-1} g^{-1} for CdS/Ti_3C_2 (Fig. 20(e)) and a kinetic constant of 0.0217 min^{-1} for tetracycline hydrochloride degradation over TiO_2/Ti_3C_2.[154,155]

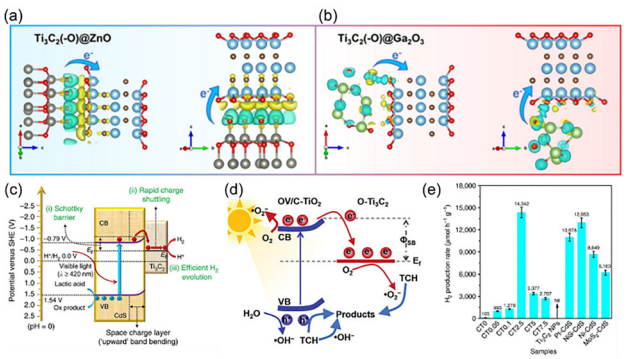

Fig. 20 (a) and (b) Differential charge density (DCD) of Ti_3C_2(–O)@metal oxide semiconductors, (c) schematic diagram of charge separation and transfer in the CdS/$Ti_3C_2T_x$ system, (d) schematic diagram of photocatalytic degradation of tetracycline hydrochloride on TiO_2/$Ti_3C_2T_x$ system, (e) photocatalytic H_2 production rate of CdS/$Ti_3C_2T_x$ (CT) system. [(a) and (b) Adapted with permission from ref. 153 Copyright © 2025 Elsevier B.V. (c) and (e) Adapted with permission from ref. 154 Copyright © 2017 Springer Nature. (d) Reproduced with permission from ref. 155 Copyright © 2023 Wiley-VCH GmbH].

5.1.2.2. Stability. Long term stability is equally critical for photocatalysis. The degradation and oxidation of photocatalysts due to ultraviolet radiation and thermal effects have restricted the application of many photocatalysts.[158] Even without external factor, structural changes in MXenes can occur, primarily due to water intercalated between layers, with oxidation initiating at vulnerable T_x such as –OH.[46,159] The incorporation of –O terminations markedly improves catalyst stability by passivating reactive surface sites, modulating the electronic structure, and forming a protective layer. In particular, –O groups establish stable covalent bonds (*e.g.*, Ti–O) with MXene transition metals, effectively shielding these active sites from oxidation. Both theoretical and experimental evidence confirms that a higher surface density of –O enhances MXene stability, supporting its durable use in photocatalysis.[78,109,160]

This strategy for stability enhancement is directly reflected in the outstanding recyclability of state-of-the-art MXene-based photocatalysts. For instance, the optimized CdS/Ti_3C_2 photocatalyst retained its activity for H_2 production without significant deterioration over seven successive cycles. Similarly, the TiO_2/O–Ti_3C_2 catalyst demonstrated high stability in tetracycline hydrochloride degradation, maintaining a removal efficiency exceeding 80% even after five repeated photodegradation cycles. These results collectively validate the effectiveness of –O function group engineering in achieving the durable performance required for practical applications.[154,155]

5.1.2.3. Optimization of light absorption properties. Light absorption is a fundamental criterion for photocatalytic performance.[161] The introduction of –O groups *via* synthesis methods such as Lewis acidic molten salt etching or annealing treatment after synthesis transforms MXenes from metallic to semiconducting states with tunable bandgaps.[162] Unlike metallic pristine MXene, –O-functionalized MXene exhibits semiconductor-like light absorption characteristics. For instance, –O-functionalized V_2NO_2 MXene exhibits a direct bandgap of approximately 0.45 eV,[163] indicating its suitability for visible light absorption applications.

This semiconducting nature enables effective harvesting of photon energy across the visible to near-infrared region, allowing –O-terminated MXenes to drive photochemical reactions under a broader spectral range. –O-terminated $Ti_3C_2T_x$ MXene possesses a bandgap of about 1 eV. These semiconducting MXenes achieved complete degradation of 25 mg L^{-1} model methylene blue and bromocresol green dyes under UV or white light irradiation.[164]

5.1.3. Organic-terminated MXenes

5.1.3.1. Reaction activation and selectivity. Organic terminations such as –phSO_3H termination on $Ti_3C_2T_x$ weakens Ti–H bonds by increasing the occupancy of antibonding orbitals

This journal is © The Royal Society of Chemistry 2026

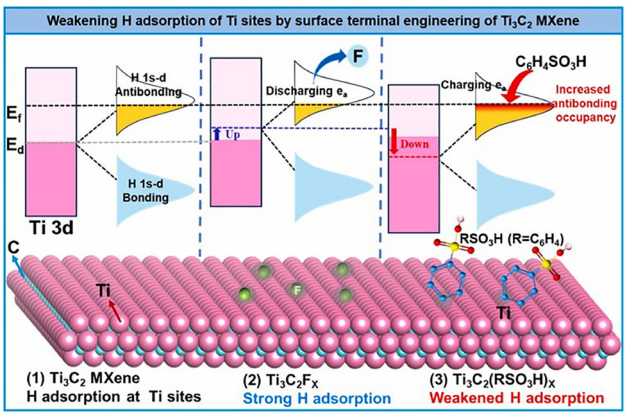

Fig. 21 Schematic diagram illustrating the T_x of weakening H adsorption at Ti sites. [Fig. 21 adapted with permission from ref. 165 Copyright © 2025 Elsevier B.V.].

(Fig. 21), facilitating H_2 evolution rates of 90.8 μmol h^{-1} g^{-1} when coupled with TiO_2.[165] These examples highlight the role of surface organic groups in optimizing MXenes for high-efficiency photocatalytic devices.

5.1.4. Heavy halogen-terminated MXenes

5.1.4.1. Optimization of light absorption properties. Extending the spectral utility further, heavy halogen-terminated MXenes, particularly as quantum dots, leverage up-conversion luminescence to harness near-infrared (NIR) light, converting it to visible/UV photons for broad-spectrum activity. $Ti_3C_2Cl_2$ MXenes quantum dots sensitized heterostructures enable efficient CO_2 reduction to CH_4, with yields of 43.71 μmol g^{-1} under visible light and 6.71 μmol g^{-1} under NIR irradiation, due to enhanced charge separation and Z-scheme mechanisms that minimize recombination.[166] This dual functionality in capacitance and photocatalysis underscores the versatility of heavy halogen-terminated MXenes for sustainable energy technologies.

5.1.5. Summary: mechanistic links between T_x, properties, and photocatalytic performance. The photocatalytic efficacy of MXenes is profoundly governed by their surface T_x, which dictate key material properties that directly control the efficiency of fundamental photocatalytic steps: light absorption, charge carrier dynamics, surface reactions, and catalyst stability. The core links are summarized in Table 3.

Overall, the photocatalytic performance of MXenes is governed by a well-defined structure–property–performance relationship: the engineered T_x dictate key material properties, such as work function, Lewis acidity/basicity, hydrophilicity, bond stability, and bandgap, which in turn directly control the efficiency of fundamental photocatalytic steps including charge separation, reactant adsorption/activation, mass transport, stability, and light harvesting, thereby driving the enhanced activity, selectivity, and durability observed in applications like hydrogen evolution, CO_2 reduction, and pollutant degradation.

5.2. Electrocatalysis–HER

Electrocatalysis plays a pivotal role in renewable energy conversion and storage, with the hydrogen evolution reaction (HER) being a cornerstone process. MXenes have emerged as promising electrocatalysts for HER, and their performance is profoundly governed by the type and engineering of T_x. This section discusses the structure–activity relationships of MXenes in HER electrocatalysis, elucidating how specific T_x modulate key properties such as e.[167]

Table 3 Structure–property–performance relationships for T_x-engineered MXenes in photocatalysis

T_x	Induced feature	Primary role in photocatalysis	Exemplary performance enhancement	Ref.
–OH	Lower work function.	**Charge mediation**: serves as a hole acceptor.	Enhanced H_2 evolution rate *vs.* MXene-free control.	53, 147 and 149
	Lewis basic sites.	**Reaction activation/selectivity**: activates CO_2, promotes C–C coupling.	High-selectivity reduction of CO_2 to ethanol with a notable yield (784 μmol g^{-1} h^{-1} on $Ti_2C(OH)_2$@g-C_3N_4 system).	129
	Hydrophilic surface.	**Mass transter**: improves reactant accessibility.	Overall water splitting with H_2 and O_2 evolution rates of 53.8 and 26.7 μmol g^{-1} h^{-1} (–OH-modified $Nb_4C_3T_x$ MXene@ZIS-OH).	35
–O	High work function.	**Charge mediation**: serves as a electron acceptor.	High H_2 yield (14 342 μmol g^{-1} h^{-1} on CdS/Ti_3C_2); superior photocatalytic performance in tetracycline hydrochloride degradation (kinetic constant of 0.0217 min^{-1} on TiO_2/O–Ti_3C_2).	154
	Stable covalent M–O bonds.	**Stability**: passivates surface against degradation.	Excellent cycling stability for both H_2 production (seven cycles, CdS/Ti_3C_2) and tetracycline hydrochloride degradation (over 80% efficiency after five cycles, TiO_2/O–Ti_3C_2).	154 and 155
	Open bandgap.	**Light harvesting**: extends absorption to visible/NIR region.	High-efficiency dye photodegradation (almost 100% effectiveness, 25 mg L^{-1} model methylene blue and bromocresol green dyes on semiconducting MXenes).	164
Heavy halogens (–Cl)	Up-conversion luminescence (in QDs).	**Light harvesting**: enables NIR-driver photocatalysis *via* up-conversion.	Efficient CO_2 to CH_4 conversion (43.71 μmol g^{-1} under visible light and 6.71 μmol g^{-1} under NIR irradiation on $Ti_3C_2Cl_2$ QDs sensitized heterostructures).	166
Organic (–phSO$_3$H)	Increasing the occupancy of anti-bonding orbitals.	**Reaction kinetics**: lowers kinetic barrierfor H_2 evolution by facilitating H desorption.	Increased H_2 evolution rate (μmol g^{-1} h^{-1} with TiO_2).	165

5.2.1. –OH MXenes. –OH-terminated MXenes (*e.g.*, Ti_3C_2OH, V_2COH, Nb_2COH) exhibit exceptional activity by providing active sites, facilitating reactant adsorption, modulating electronic structures, and improving electrode hydrophilicity and stability.[167,168]

5.2.1.1. Enhancement of active sites. The –OH on MXenes create abundant active sites, particularly at edges and defects, which are crucial for electrocatalytic reactions.[123,169,170] For instance, in Ti_3C_2-based MXene quantum dots (QDs), the reduction from 2D nanosheets to 0D QDs exposes more edge sites terminated with –OH. These sites show higher activity for HER compared to basal planes, as confirmed by DFT calculations indicating lower energy barriers for intermediate H* adsorption on edge –OH sites (Fig. 22(a)). This effect is also exemplified by Ti_4N_3 MXenes with high –OH coverage achieved *via* TMAOH treatment, which optimizes hydrogen adsorption free energy, resulting in a low onset potential of −0.26 V *vs.* RHE (Fig. 22(b) and (c)).[49]

5.2.1.2. Modulation of charge transfer. The functionalization of –OH affects the density of states (DOS) and charge transfer of MXene. DFT studies reveal that –OH groups increase the DOS near the Fermi level in Ti_3C_2OH, enhancing metallic conductivity and electron transfer kinetics.[171] This favourable electronic structure reduces the energy barriers for rate-determining steps. Consequently, –OH-terminated MXenes such as Ti_3C_2OH QDs exhibit a Tafel slope of 106 mV dec^{-1}, indicating faster kinetics compared to –F-terminated counterparts.[169]

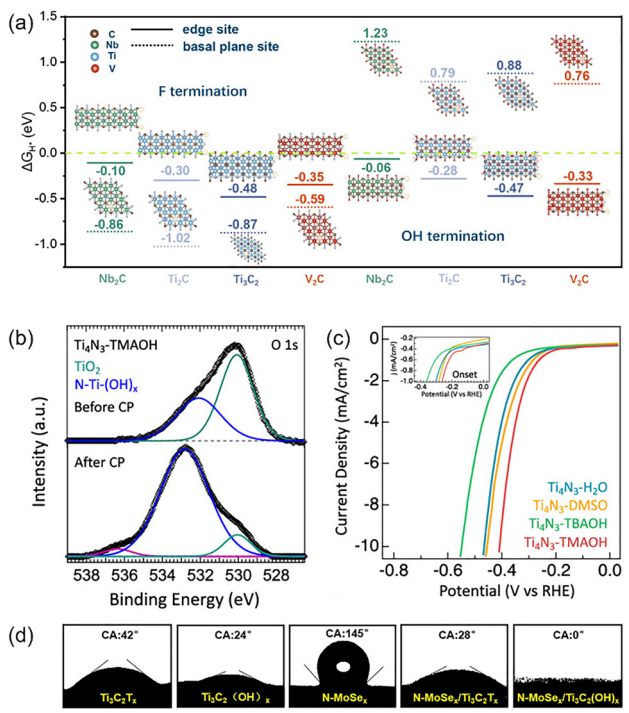

Fig. 22 (a) Gibbs free energy diagrams of MXenes functionalized with different T_x obtained through calculation, (b) O 1s XPS spectra of Ti_4N_3, (c) LSV curves of Ti_4N_3 after chronopotentiometry, and (d) contact angle measurement. [(a) Adapted with permission from ref. 169 Copyright © 2022 Elsevier B.V. (b) and (c) Adapted with permission from ref. 49 according to CC-BY. 4.0 Copyright © 2025 American Chemical Society. (d) Adapted with permission from ref. 123 Copyright © 2023 Elsevier B.V.].

5.2.1.3. Improvement in electrode hydrophilicity. –OH functionalized MXenes, markedly enhances hydrophilicity and catalytic stability by optimizing surface-water interactions and reinforcing structural integrity.[172,173] Furthermore, the interlayer –OH of MXenes can undergo dehydration condensation to form Ti–O–Ti bridging structures, which not only strengthen mechanical integrity but also allow precise regulation of interlayer spacing to facilitate ion transport.[174,175] As demonstrated in contact angle measurements (Fig. 22(d)), the –OH terminations reduce the contact angle from 42° (Ti_3C_2) to 24° ($Ti_3C_2(OH)_x$), facilitating efficient water adsorption for electrocatalytic reactions. N-$MoSe_x$/$Ti_3C_2(OH)_x$ exhibited excellent alkaline HER activity, with an overpotential of 114 mV at 10 mA cm^{-2} and a Tafel plot of 97 mV dec^{-1}. –OH also promotes strong interfacial bonding, suppresses oxidative degradation, and ensures durability during long-term operation, leading to sustained high performance.[123,176,177]

In summary, the strategic engineering of –OH terminations on MXenes enhances HER performance through a synergistic combination of mechanisms: creating abundant active sites, optimizing the adsorption of reaction intermediates, improving electronic conductivity and charge transfer kinetics, and increasing surface hydrophilicity alongside long-term operational stability.

5.2.2. –O MXenes

5.2.2.1. Optimization of adsorption and desorption of intermediates and products. For HER, A key advantage of –O terminations is their ability to optimize the adsorption energetics of reaction intermediates H*. DFT calculations indicate that –O-functionalized MXenes yield a near-zero hydrogen adsorption free energy (ΔG_{H^*}), which is conducive to both efficient proton adsorption and H_2 desorption.[154,178] Experimentally, –O-functionalized $Ti_3C_2O_x$ MXene exhibits a low overpotential of 190 mV at 10 mA cm^{-2} and a Tafel slope of approximately 60.7 mV dec^{-1} in 0.5 M H_2SO_4 at 5 mV s^{-1}, outperforming its –F- or –OH-functionalized counterparts (Fig. 23(a)).[179]

5.2.2.2. Improvement of stability and corrosion resistance. Beyond optimizing reaction kinetics, –O critically enhance the operational stability of MXene electrocatalysts. They form robust covalent bonds (*e.g.*, Ti–O) that elevate the oxidation state of the transition metal and thereby resist oxidative degradation. Compared to –F-rich MXenes, –O-functionalized Ti_2CO_2 demonstrates markedly improved stability, maintaining structural integrity in aqueous solutions for up to 30 days without significant oxidation, as confirmed by XRD and SEM (Fig. 23(b) and (c)).[180] This corrosion resistance is particularly valuable in harsh environments. For example, in seawater electrolysis, –O groups improve chloride corrosion resistance, while in heterostructures (Ni,Fe)S_2@$Ti_3C_2O_x$, the formation of stable bridges (*e.g.* Ti–O–Fe) inhibits metal dissolution, enabling long-term durability over 1000 hours at industrial current densities.[12]

For HER reaction, the stability of MXene-based materials in electrolyte environments is critical, as it directly governs the

 This journal is © The Royal Society of Chemistry 2026

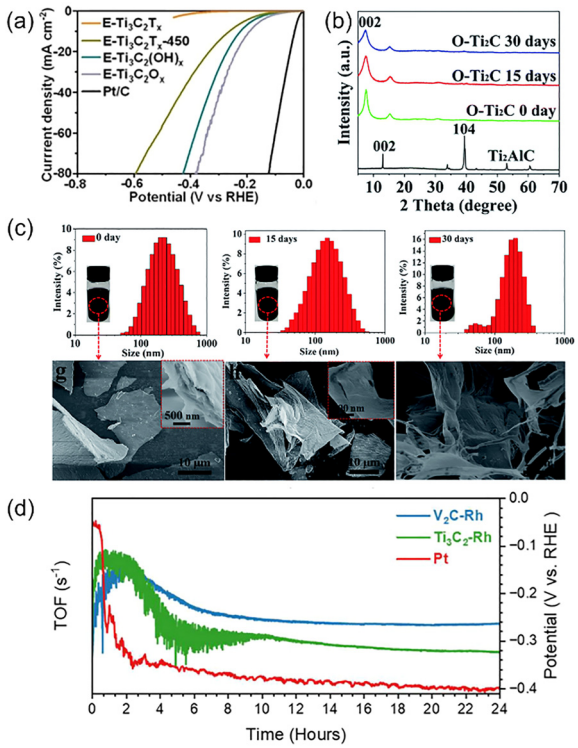

Fig. 23 (a) Polarization curves of different functionalized $Ti_3C_2T_x$, (b) XRD spectrum, and (c) particle size and SEM images of –O-functionalized Ti_2C after being left for several days, and (d) stability test of HER activity of materials. [(a) Adapted with permission from ref. 179 Copyright © 2019 Wiley-VCH Verlag GmbH. (b) and (c) Adapted with permission from ref. 180 Copyright © 2022 Royal Society of Chemistry. (d) Adapted with permission from ref. 178 according to CC-BY. Copyright © 2025 Wiley-VCH GmbH].

durability and sustained performance of the electrocatalyst. For instance, Rh modified –O-functionalized MXenes nanosheets demonstrate notable catalytic activity and durability across acidic, alkaline, and neutral conditions. As illustrated in Fig. 23(d), these MXene-based materials exhibit significantly enhanced electrocatalytic stability compared to conventional platinum-based catalysts.[178]

5.2.3. –F-free MXenes

5.2.3.1. Exposure of catalytic sites. While –O engineering optimizes existing sites, the synthesis of –F-free MXenes represents a complementary strategy focused on eliminating the –F groups that often impede active site accessibility and charge transfer.[181] Replacing inert –F groups with electrochemically active –O and –OH enhances surface reactivity, improves electrical conductivity, and exposes a greater density of catalytic sites.[154,182] For example, –F-free Ta_2C MXenes synthesized *via* alkali etching achieves an overpotential of 223 mV at 10 mA cm^{-2} in acidic media, alongside efficient nitro reduction with 72% conversion and 96% faradaic efficiency, attributed to reduced charge transfer resistance and increased active site availability.[183]

Similarly, –F-free $Ti_3C_2T_x$ (T = O, OH) serves as an excellent conductive substrate for MoS_2 hybrids, enabling an overpotential of 139 mV at 10 mA cm^{-2} and a Tafel slope of 78 mV dec^{-1} in acidic HER, due to optimized mass transport and enhanced –O-terminated active sites.[184] Microwave-assisted –F-free synthesis further enhances HER in alkaline media, with MXene showing 140 mV overpotential at 10 mA cm^{-2} and 84 mV dec^{-1} Tafel slope, due to improved ion intercalation and hydrophilicity.[185]

5.2.4. –S MXenes

5.2.4.1. Enhancement of charge transfer. Progressing beyond the modulation of native T_x, the introduction of entirely new T_x, such as –S, can create novel active sites. –S-functionalization has emerged as a powerful strategy to boost the HER activity of MXenes. For instance, sulfurization of $Mo_{4/3}C$ MXenes *via* annealing with thiourea introduces Mo–S bonds, reduce charge-transfer impedance, the active site for hydrogen evolution. The resulting –S–$Mo_{4/3}C$ exhibits a low overpotential of 210 mV at 10 mA cm^{-2} in acidic media, surpassing pristine $Mo_{4/3}C$ (620 mV) and even 1T-MoS_2 (320 mV).[186] Similarly, MoS_2/Mo_2CT_x hybrids, prepared by *in situ* sulfidation, demonstrate amorphous MoS_2 domains grafted onto MXenes surfaces. These structures yield a high HER activity (overpotential of 110 mV in alkaline media) due to the coexistence of –S and inherent –O/–OH, which facilitate H intermediate adsorption and kinetics.[187]

5.2.5. Summary: mechanistic links between T_x, properties, and electrocatalysis HER performance.

As shown in Table 4. The electrocatalytic HER performance of MXenes is governed by a well-defined structure–property–performance relationship mediated by surface T_x. Among various T_x, –O play a particularly pivotal role by offering a dual advantage. First, –O groups form stable covalent M–O bonds that effectively passivate the MXene surface, significantly enhancing its oxidation resistance and long-term operational stability. Second, –O optimize the ΔG_{H^*} to near-thermoneutral values, thereby increasing the number and efficiency of electrochemically active sites for the Volmer and Heyrovsky/Tafel steps. This combination of robust antioxidative protection and optimized adsorption energetics makes –O-engineered MXenes highly promising and durable electrocatalysts for the HER. Beyond the prominent role of –O, other T_x also confer distinct advantages for the HER. –OH enhance surface hydrophilicity, improve intermediate adsorption at edge sites, and boost electronic conductivity near the Fermi level. –S, as in Mo–S motifs, significantly reduce charge-transfer resistance. Looking forward, the greatest potential may lie in the synergistic interplay of multiple T_x. By precise surface engineering, it might be possible to design MXenes with patterned surface patches or gradient functionalization, where –O ensures stability, –OH optimizes hydrophilicity and local adsorption, and –S or other groups enhance charge transfer, collaboratively optimizing all aspects of HER activity, conductivity, and durability. This multidimensional approach opens a new avenue for the rational design of next-generation, high-performance MXene HER electrocatalysts.

5.3. Electrocatalysis–OER, CO_2RR, eNO_3^-RR, NRR, and ORR

Apart from HER reaction, MXenes also demonstrate significant potential in a broader spectrum of electrocatalytic processes

Table 4 Structure–property–performance relationships for T_x-engineered MXenes in electrocatalysis HER

			Exemplary performance enhancement				
T_x	Induced feature	Primary role in HER	MXene based material	Overpotential (mV *vs.* RHE)	Tafel slope (mV dec^{-1})	Stability	Ref.
–OH	Low electronegativity O-containing surface.	**Reaction activation:** ΔG_{H^*} close to zero, creates abundant active sites.	Ti_4N_3-TMAOH	260 (10 mA cm^{-2})	167.7	After 18 h of CP, overpotential slow decay was observed.	49
	Enhancement of DOS near the Fermi level in MXenes.	**Charge mediation:** enhancing metallic conductivity.	Ti_3C_2 QDs	201 (10 mA cm^{-2})	106	2000 cycles, an overpotential decay of 27 mV.	169
	Hydrophilic surface.	**Mass transter:** improves electrode hydrophilicity.	N-$MoSe_x$/ $Ti_3C_2(OH)_x$	114 (10 mA cm^{-2})	97	1000 cycles and 11.0-h test, no significant overpotential decay.	123
–O	ΔG_{H^*} close to zero.	**Reaction activation:** optimization of adsorption and desorption of H*.	$Ti_3C_2O_x$	190 (10 mA cm^{-2})	60.7	2000 cycles, negligible current decay.	179
	Oxidation state increase of the transition metal.	**Stability:** improvement of stability and corrosion resistance.	Rh-Ti_3C_2	127 (10 mA cm^{-2})	83.8	Better 24-h stability than Pt.	178
–F-free	Replacement of inert –F.	**Reaction activation:** exposure of catalytic sites.	–F-free Ta_2C	223 (10 mA cm^{-2})	75	24 h test, without any degradation in catalytic activity.	183
			–F-free $Ti_3C_2T_x/MoS_2$	139 (10 mA cm^{-2})	78	3000 cycles, negligible current decay.	184
			–F-free $Ti_3C_2T_x$	140 (10 mA cm^{-2})	84	9-h test, maintenance of stable potential.	185
–S	Mo–S reduce charge-transfer resistance.	**Charge mediation:** enhancing charge-transfer.	–S–$Mo_{4/3}C$	210 (10 mA cm^{-2})	67	5000 cycles, 100-h test, negligible current decay.	186
			MoS_2/Mo_2CT_x	110 (10 mA cm^{-2})	65	3000 cycles, without a decrease in current density.	187

crucial for renewable energy conversion. These include the oxygen evolution reaction (OER), carbon dioxide reduction reaction (CO_2RR), electrocatalytic nitrate reduction reaction (eNO_3^-RR), nitrogen reduction reaction (NRR), and the oxygen reduction reaction (ORR). The following section delves into the structure–activity relationships of MXenes in these diverse electrocatalytic applications, focusing on the pivotal roles played by specific T_x.[167,171,188]

5.3.1. –OH MXenes

5.3.1.1. Hydrogen donor for key intermediates. In the electrochemical CO_2RR, the –OH groups on MXenes serve as active hydrogen donors, stabilize key reaction intermediates through hydrogen bonding and direct hydrogen sharing. During the CO_2 reduction process, the H atoms from the –OH groups are captured by the intermediates, forming species such as *(H)COOH and (H)CHO, which lowers the energy barriers for the proton-coupled electron transfer (PCET) steps (Fig. 24(a). For instance, in $Sc_2C(OH)_2$, the reaction proceeds *via* an alternative pathway where CO_2 binds with the –OH group to form (H)COOH, exhibiting an adsorption energy of −0.53 eV).[189]

5.3.1.2. Promotion of reactant adsorption and activation. The –OH groups also significantly enhances the adsorption and activation of reactant molecules. For the NRR, –OH-terminated Ti_3C_2 MXene provides active sites for N_2 activation, with DFT showing that –OH-MXene spontaneously adsorbs N_2, improving the selectivity toward NH_3 over HER (Fig. 24(b)). The NH_3 yield of –OH functionalized Ti_3C_2 QDs is 62.94 μg h^{-1} mg_{cat}^{-1}, surpassing the performance of many reported electrocatalysts.[37]

Similarly, in the eNO_3^-RR, the –OH groups on Ti_3C_2 MXenes form hydrogen bonds with NO_3^-, and –OH participates in the adsorption and stability of intermediates (Fig. 24(c)). –OH-rich Ti_3C_2 MXene achieves a faradaic efficiency (FE) of 90.4% for NH_3 by blocking H* formation, as –OH groups exhibit higher HER overpotentials than NRR steps. Competitive HER was significantly inhibited, highlighting the unique advantage of –OH-functionalized MXene in eNO_3^-RR reaction.[190]

5.3.1.3. Modulation of electronic structure. Beyond direct chemical participation, –OH groups are instrumental in tuning the electronic structure of catalyst composites, which is crucial for reactions like the OER. In the MXene–OH@CoS heterostructure, the –OH groups with rich electronic distribution facilitate an optimized interfacial electron transfer (1.23 e) to the CoS nanoparticles, as revealed by DFT calculations (Fig. 24(d)). This moderate charge transfer optimally regulates the electronic structure of the catalytic Co sites, shifting the d-band centre to a higher energy (−1.61 eV). The upward shift strengthens the adsorption of oxygen-containing intermediates, thereby reducing the free energy barrier for the potential-determining step. This electronic modulation results in superior OER activity, with the catalyst demonstrating a low overpotential of 244 mV at 10 mA cm^{-2} and a Tafel slope of 34.9 mV dec^{-1}, outperforming catalysts with other terminations (–F, –O).[188]

5.3.2. –O MXenes

5.3.2.1. Optimization of adsorption and desorption of intermediates and products. For eNO_3^-RR, –O-functionalized surfaces promote facilitate the hydrogenation step from $*NH_2$ to $*NH_3$,

 This journal is © The Royal Society of Chemistry 2026

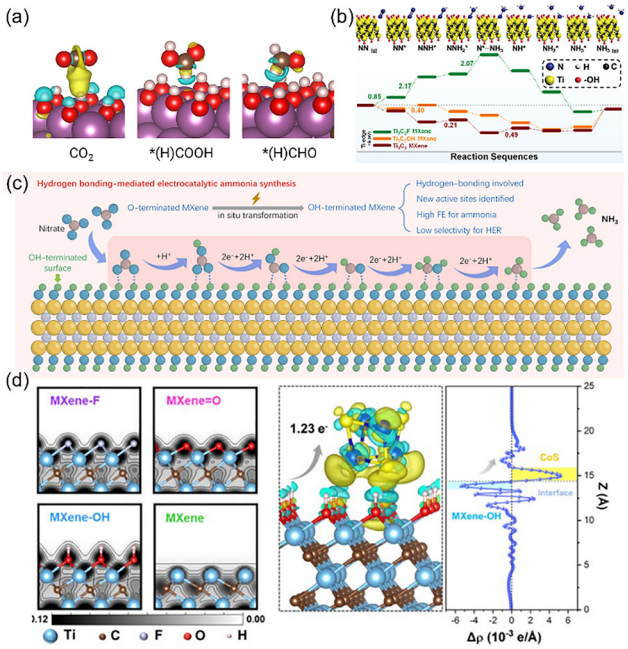

Fig. 24 (a) Deformation charge density of CO_2, *(H)COOH, and *(H)CHO, charge migrates from the H and H–O bonds to the C–H bond, corresponding to outflow (blue) and inflow (yellow) regions in the deformation charge density maps. The interaction energies of these fragments with the substrate are −0.17 eV (CO_2), −0.53 eV ((H)COOH), and −0.37 eV ((H)CHO), (b) reaction mechanism diagram of NRR on the edge Ti of Ti_3C_2 MXenes functionalized with different T_x by distal pathway, (c) schematic diagram of –OH as the active site of eNO_3^-RR, (d) surface charge distribution of MXenes materials and their interface with CoS. The calculated deformation charge density at the MXene–OH/CoS interface shows electron accumulation/depletion (yellow/cyan), with the corresponding planar average potential plotted along the vertical *z* axis. [(a) Adapted with permission from ref. 189 Copyright © 2019 American Chemical Society. (b) Adapted with permission from ref. 37 Copyright © 2020 WILEY. (c) Adapted with permission from ref. 190 Copyright © 2023 Elsevier B.V. (d) Adapted with permission from ref. 188 Copyright © 2023 Royal Society of Chemistry].

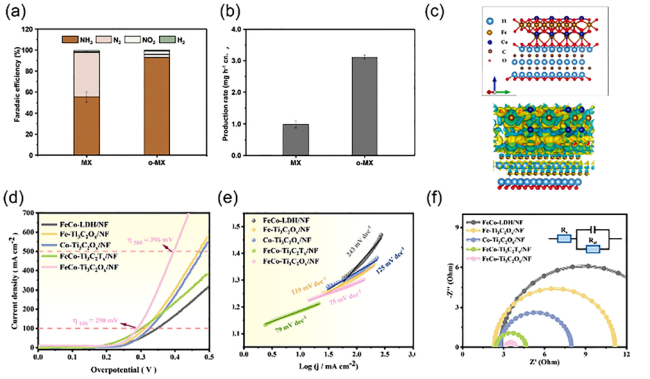

Fig. 25 (a) FE, and (b) NH_3 production rate of –O-functionalized MXenes and MXenes, (c) charge density difference plot of the FeCo–$Ti_3C_2O_x$ hybrid system, electron accumulation (yellow regions) is observed on the –O-terminated side of $Ti_3C_2O_x$, while electron depletion (cyan regions) appears on the $CoFe_2O_4$ side, indicating electron transfer from $CoFe_2O_4$ to the $Ti_3C_2O_x$, (d) polarization curves, and (e) Tafel slopes, and (f) Nyquist plots of FeCo–$Ti_3C_2O_x$/NF and control samples. [(a) and (b) Adapted with permission from ref. 191 Copyright © 2025 Royal Society of Chemistry. (c)–(f) Adapted with permission from ref. 192 Copyright © 2025 Elsevier Ltd.].

thereby lowering the energy barrier of the rate-determining steps. This is demonstrated by $Ti_3C_2O_x$, which achieves a high faradaic efficiency of 92.8% and an NH_3 production rate of 3.278 mg h^{-1} cm^{-2}, outperforming its Un–O-functionalized counterparts (Fig. 25(a) and (b)).[191]

5.3.2.2. Optimization of electronic structure and charge transfer dynamics. The incorporation of –O groups primarily optimizes the electronic structure of MXenes by withdrawing electrons from transition metal centers (*e.g.*, Ti, Fe, Ni), thereby increasing their oxidation state and enhancing metal–oxygen covalency (Fig. 25(c)).[180] This electronic redistribution, along with an upshifted O 2p band centre, improves charge transfer dynamics and strengthens the adsorption of reaction intermediates. As a direct application of this modulation, –O-functionalized systems such as FeCo/$Ti_3C_2O_x$ exhibit accelerated reaction kinetics, achieving a low charge transfer resistance of 0.7 Ω and a ultralow OER overpotential of 396 mV at 500 mA cm^{-2} with a Tafel slope of 75 mV dec^{-1} (Fig. 25(d)–(f)), underscoring the critical structure–performance relationship enabled by surface –O-functionalization.[192,193]

5.3.3. –S MXenes

5.3.3.1. Optimization of charge transfer dynamics. Unlike the disordered –OH/–F/–Cl on typical MXenes that limit conductivity, the orderly –S-terminated structure of Ta_2CS_2 facilitates electron transfer from Ta to S groups. This results in a 22.48 times higher conductivity (3.149×10^4 S m^{-1}) and a 79.4 times greater charge carrier concentration (1.637×10^{21} cm^{-3}) compared to $Ta_4C_3T_x$, optimizing the electronic structure for electrocatalysis. Optimization of adsorption and desorption of intermediates and products: the superior electronic properties translate to excellent bifunctional activity. The exfoliated Ta_2CS_2 nanosheets require low overpotentials of 243 mV for OER and 73 mV for HER at 10 mA cm^{-2} (Fig. 26(a) and (b)), with small Tafel slopes (61.1 and 66.9 mV dec^{-1}, respectively), indicating favorable reaction kinetics. When configured as both anode and cathode, the Ta_2CS_2 electrolyzer delivers a current density of 10 mA cm^{-2} at only 1.51 V and maintains stability for over 100 hours (Fig. 26(c)), positioning it among the best MXene-based catalysts.[194] This underscores how high ordered –S-termination enhances charge transfer processes critical for efficient overall water splitting.

5.3.4. –NH_x MXenes

5.3.4.1. Covalent bridge. –NH_x on MXene surfaces acts as a structural anchor and an electronic structure modulator. In heterojunctions with covalent organic frameworks (COFs), the amino groups (–NH_2) serve as covalent linkage sites. This facilitates the *in situ* growth of COFs, forming robust heterointerfaces with built-in electric fields (Fig. 26(d)). A key feature is the directional electron transfer, typically from the COF to the amino-functionalized MXene, which optimizes the charge density at catalytically active sites. This electronic modulation strengthens the adsorption of key intermediates and lowers

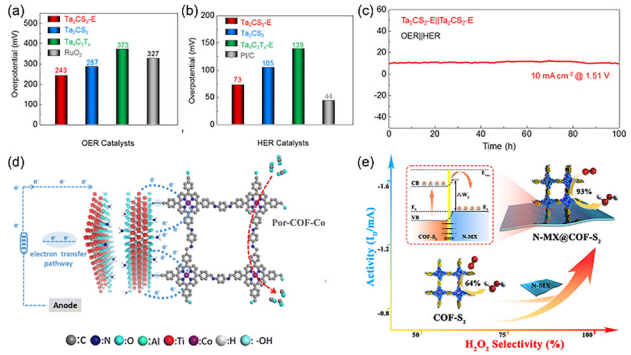

Fig. 26 (a) OER, and (b) HER overpotentials at 10 mA cm^{-2}. (c) Time-dependent current density curves of Ta_2CS_2 at an overpotential of 73 mV, (d) and (e) schematic illustration of $-NH_x-Ti_3C_2$ MXene nanosheets@COF heterostructure. [(a)–(c) Adapted with permission from ref. 194 Copyright © 2021 Wiley-VCH GmbH. (d) Adapted with permission from ref. 195 Copyright © 2024 Royal Society of Chemistry. (e) Adapted with permission from ref. 196 Copyright © 2025 American Chemical Society].

reaction barriers. For instance, in the $-NH_x$–MXenes@COF-S_2 heterojunction, this effect leads to ORR H_2O_2 selectivity >90% in neutral media (Fig. 26(e)).[196] Similarly, the covalently connected covalent bridge in MXene@COF enhances charge transfer, achieving a faradaic efficiency of 97.28% for CO_2-to-CO conversion.[195]

5.3.5. Summary: mechanistic links between T_x, properties, and electrocatalysis OER, CO_2RR, eNO_3^-RR, NRR, and ORR performance. The electrocatalytic performance of MXenes in OER, CO_2RR, eNO_3^-RR, NRR, and ORR is fundamentally governed by a well-defined structure–property–performance relationship orchestrated by surface T_x. Distinct T_x confer specific functionalities: –OH groups serve as hydrogen donors and active sites, promoting reactant adsorption/activation for CO_2RR, NRR, and eNO_3^-RR, while also modulating electronic structures in composites to enhance OER kinetics. –O optimize the adsorption/desorption energetics of key intermediates (*e.g.*, in eNO_3^-RR), improve charge transfer dynamics, and provide crucial antioxidative stability. Emerging terminations like –S significantly enhance charge transfer conductivity, beneficial for OER and HER, whereas $-NH_x$ groups act as covalent bridges in heterostructures, optimizing interfacial charge transfer for reactions like CO_2RR and ORR. The future of high-performance MXene electrocatalysts lies in the rational, synergistic engineering of multiple T_x, creating surfaces where different functional groups collaboratively optimize stability, reactivity, and charge transport for these diverse and critical reactions.

5.4. Energy storage and conversion devices

This section summarizes the impact of MXenes in energy storage and conversion devices, drawing insights from supercapacitors, and battery systems.

5.4.1. –OH MXenes

5.4.1.1. Provision of redox-active sites. The incorporation of –OH in MXenes significantly boosts their pseudocapacitive behavior by providing abundant redox-active sites and facilitating rapid ion transport.[59] –OH-rich MXene QDs exhibit superior specific pseudocapacitance and enhanced redox kinetics. This advantage stems from their abundant surface –OH, which serve as redox-active sites:

$$Ti_3C_2O_x(OH)_yF_{2-x-y} + \delta e^- + \delta H^+ \Leftrightarrow Ti_3C_2O_{x-\delta}(OH)_{y+\delta}F_{2-x-y} \quad (22)$$

after incorporating 20 wt% –OH-functionalized MXene QDs into a MXene nanosheet matrix, the composite achieves a specific capacitance of 372.2 F g^{-1} at a scan rate of 10 mV s^{-1}. This represents a 20% improvement compared to pure MXene nanosheets, underscoring the beneficial role of –OH functionalization in boosting pseudocapacitive performance.[174]

5.4.1.2. Modulation of electronic structure. Functionalization with –OH improves surface conductivity and charge transfer kinetics, which enhances the capacitive performance of MXenes.[198] This improvement arises from the direct modulation of the electronic structure and an increase in quantum capacitance (C_{diff}), driven by the significant contribution of –OH to the density of states (DOS) near the Fermi level. In some systems, –OH can also induce a semiconductor-to-metal transition, further promoting charge storage.[199]

Partial density of states (PDOS) analyses show that –OH provides substantial electronic states in the −3 eV to −6 eV energy range. Notably, in MXenes such as Ti_2C, –OH introduction can trigger a semiconductor-to-metal transition, yielding a high DOS at the Fermi level essential for large C_{diff}. Consequently, –OH-terminated MXenes outperform –O- or –F-terminated counterparts. For example, $Cr_2C(OH)_2$ exhibits a high C_{diff} at negative potential (C_n = 4366.44 μF cm^2), while $V_2C(OH)_2$ reaches a peak C_{diff} (C_p = 3010.51 μF cm^2) at positive potential, underscoring the critical role of –OH.

The advantage of –OH is further evident in comparative studies. For Cr_2CT_2 systems, $Cr_2C(OH)_2$ shows markedly higher C_{diff} at negative potentials than Cr_2CO_2 (Fig. 27(a)). This highlights the unique ability of –OH functionalization to tailor electronic properties for optimized capacitive storage.[197]

5.4.1.3. Construction of hydrogen-bond ion transport networks. –OH contribute to the formation of hydrogen-bond networks, which establish efficient ion transport pathways within the material (Fig. 27(b)).[200,201] This structural advantage is clearly demonstrated in composite systems: –OH-functionalized MXenes enable flexible supercapacitors with a wide voltage window (2.3 V) and high capacitance retention (83% after bending), underscoring their potential in wearable energy storage devices.[176]

5.4.1.4. Ion activation. –OH-rich MXene (D-$Ti_3C_2T_x$) significantly enhances Li-ion battery performance by serving as a conductive scaffold and forming robust hydrogen bonds with organic molecules or ions (Fig. 27(c)).[124,202] This improvement stems from two key mechanisms: –OH act as anchors to immobilize small organic molecules *via* hydrogen bonding, effectively suppressing their dissolution in the electrolyte, while simultaneously providing a highly conductive network that

 This journal is © The Royal Society of Chemistry 2026

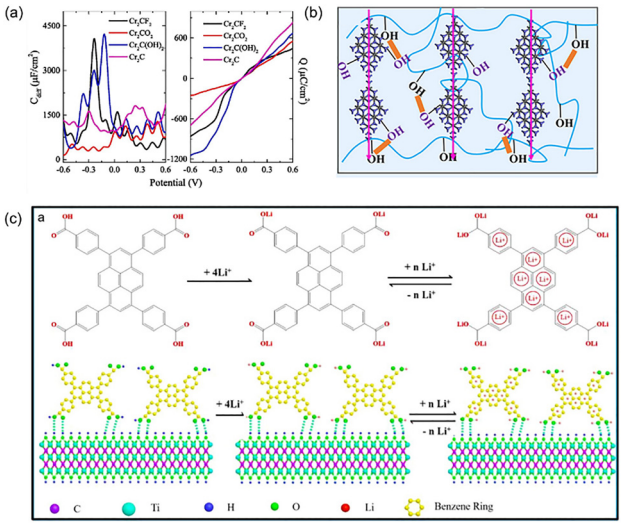

Fig. 27 (a) The quantum capacitance (C_{diff}) of M_2CT_2 (T = –OH, –O, –F, and bare), (b) schematic diagram of MXene–OH constructing directional ion transport channels, (c) schematic diagram of lithiation and delithiation of TBAP@D-$Ti_3C_2T_x$ electrode. [(a) Adapted with permission from ref. 197 Copyright © 2024 Elsevier B.V. (b) Adapted with permission from ref. 176 Copyright © 2023 American Chemical Society. (c) Adapted with permission from ref. 124 Copyright © 2022 American Chemical Society].

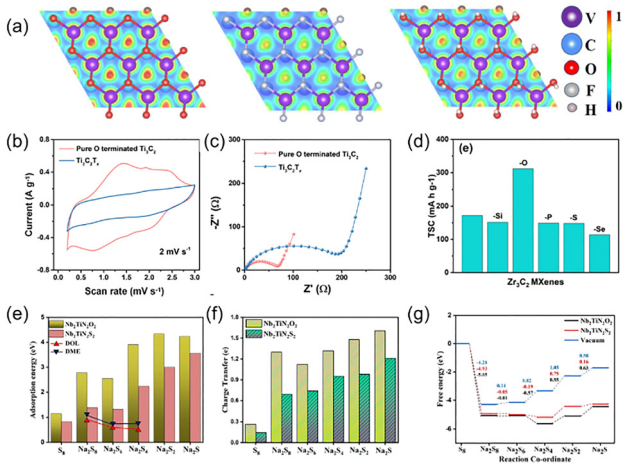

Fig. 28 (a) The electron localization function (ELF) images of different functionalized V_2CT_x, (b) CV profiles, and (c) Nyquist plots of $Ti_3C_2T_x$ and pure –O-functionalized Ti_3C_2, (d) theoretical storage capacity (TSC) of different functionalized Zr_3C_2 MXenes, (e) calculated adsorption energies, and (f) computed charge transfer of S_8 and Na_2S_n adsorbed on different functionalized Nb_2TiN_2, (g) Gibbs free energy of sulfur reduction reaction on different functionalized Nb_2TiN_2. [(a) Adapted with permission from ref. 112 Copyright © 2022 Elsevier Ltd. (b) and (c) Adapted with permission from ref. 113 Copyright © 2025 Elsevier Ltd. (d) Adapted with permission from ref. 203 Copyright © 2024, American Chemical Society. (e)–(g) Adapted with permission from ref. 204 Copyright © 2025 Royal Society of Chemistry].

facilitates rapid electron transport. TBAP@D-$Ti_3C_2T_x$ composite achieves a reversible capacity of 747.7 mAh g^{-1} after 200 cycles at 100 mA g^{-1}, with the TBAP component contributing a capacity of 907.2 mAh g^{-1}—nearly three times that of the pure organic electrode. Furthermore, the hydrogen-bonded structure enables a powerful π-Li cation effect, activating each benzene ring to reversibly store up to six Li^+ ions, while the expanded interlayer spacing and increased specific surface area (89.2 m^2 g^{-1}) promote faster Li^+ diffusion, as evidenced by a higher diffusion coefficient (2.10–3.06 × 10^{-11} cm^2 s^{-1}) compared to the pure organic material.

5.4.2. –O MXenes. The –O groups significantly enhance electrochemical performance by providing active sites, tuning electronic structures, facilitating ion transport, and improving stability, as demonstrated in various MXene systems such as $Ti_3C_2O_x$, V_2CO_2, and Nb_2CO_2.

5.4.2.1. Introduction of electroactive sites. The –O termination on MXenes introduces abundant electroactive sites that participate in typical redox of MXenes, leading to high pseudocapacitance (eqn (22)). For instance, –O-functionalized $Ti_3C_2T_x$ exhibits a specific capacitance of 554 F g^{-1} at 30 A g^{-1} in supercapacitors, which is over seven times higher than pristine $Ti_3C_2T_x$, due to the activation of surface C–Ti–O enabling efficient charge storage.[23] The –O termination induces a substantial redistribution of surface electrons in MXenes, significantly enhancing electron localization at the active sites. This is evidenced by electron localization function (ELF) analysis, which reveals that V_2CO_2 exhibits the highest ELF value among V_2CT_2 (T = –O, –F, or –OH) configurations, creating an electron-rich surface environment (Fig. 28(a)). Such an electronic modulation, driven by the high electronegativity of oxygen, facilitates charge transfer and optimizes the adsorption of key reaction intermediates (*e.g.*, LiO_2, Li_2O_2).[112] Consequently, the tailored surface electronic structure directly boosts the capacity and redox activity of –O-terminated MXenes in lithium–oxygen batteries.

5.4.2.2. Optimization of work function and conductivity. The –O termination effectively modulates the electronic structure of MXenes, leading to a lower and tunable work function and enhanced electrical conductivity, which collectively improve charge injection in electronic devices.[43] This electronic optimization also significantly boosts electrochemical performance in energy storage. For instance, –O-functionalized Ti_3C_2 shows a tunable work function range of 3.67–4.17 eV, exhibits a cyclic voltammetry (CV) curve area more than double that of its pristine counterpart, indicating a greater than twofold increase in Li^+ storage capacity (Fig. 28(b)). Additionally, the charge transfer resistance (R_{CT}) drops substantially from 217 Ω to 86 Ω, confirming that the –O termination promotes faster Li^+ transport (Fig. 28(c)).[113] DFT studies reveal that –O termination increases the density of states near the Fermi level, reducing charge transfer resistance and enabling rapid electron transport.

5.4.2.3. Facilitation of ion diffusion and adsorption. The diffusion and adsorption of metal ions such as Li^+, Na^+, K^+, Ca^{2+}, Mg^{2+}, and Al^{3+} are highly sensitive to surface T_x of MXens.[205] Bader charge analysis confirms that the electronegative –O induce an electron-rich surface environment, which reduces the Li^+ diffusion barrier on $Zr_3C_2O_2$ to 0.298 eV, lower than that

of graphene (0.327 eV), thereby enabling rapid charge/discharge and improved rate capability. In addition, –O termination promotes the stable adsorption of two full layers of Li atoms, whereas other T_x typically permit only a single adsorbed layer. This dual-layer adsorption mechanism directly contributes to a high theoretical Li^+ storage capacity of 312 mA h g^{-1} (Fig. 28(d)).[203]

The electron-rich surface of –O-functionalized MXene, which significantly enhances the electrolyte wettability and facilitates Li^+ desolvation. This optimized interface substantially reduces the Li^+ diffusion barrier, enabling rapid ion transport even at low temperatures. Consequently, the –O-functionalized $Ti_3C_2T_x$ exhibits a high reversible capacity of 226 mAh g^{-1} at −20 °C and outstanding cycling stability, retaining 193.9 mAh g^{-1} after 1000 cycles, far surpassing conventional anodes.[206]

5.4.2.4. Stability of key intermediates. The high electronegativity of –O enables efficient electron withdrawal from the transition metal framework (*e.g.*, Nb, Ti) in MXenes, resulting in a more negatively charged surface.[207] This enhanced surface negativity strengthens electrostatic interactions with positively charged species, such as sodium ions in polysulfides (Fig. 28(e) and (f)). Furthermore, owing to its superior electron affinity, the –O termination promotes greater charge transfer with reactants. In Na–S batteries, the conversion of soluble Na_2S_4 to insoluble Na_2S_2 constitutes the rate-determining step. Notably, –O-functionalized MXenes exhibit a stronger adsorption affinity for positively charged Na_2S_2, effectively mitigating polysulfide dissolution. Theoretical calculations confirm that the –O-functionalized surface (*e.g.*, $Nb_2TiN_2O_2$) significantly reduces the energy barrier of this step to 0.55 eV, outperforming the –S-functionalized analog (0.75 eV) and the gas phase reaction (1.05 eV) (Fig. 28(g)).[204]

5.4.3. –F MXenes. –F significantly modulates the fundamental properties of MXenes, enabling tailored electronic, catalytic, and electrochemical behaviors through controlled fluorination or defluorination processes.[38] The evolution from –F-rich to –F-free MXenes reveals a clear trend: –F-functionalized MXenes often induce semiconductor-like transport or enhanced antioxidant stability, while –F-free states promote metallic conductivity and catalytic activity.[76]

The transition from –F-rich to –F-free terminations drives a significant shift in electronic behavior. –F-rich MXenes, due to the strong electron-withdrawing nature of fluorine and the associated intercalants, often exhibit a reduced density of states at the Fermi level, leading to semiconductor-like transport properties characterized by a negative temperature coefficient of resistance (dR/dT).[199] Upon thermal removal of F-groups and intercalants, a pronounced evolution occurs: the material transitions towards metallic behavior, with carrier density increasing and electron scattering decreasing.[38] This is evidenced by a 4 to 10-fold increase in electronic conductivity, correlating directly with the loss of –F-terminations as confirmed by *in situ* spectroscopic and electrical measurements.

The chemical environment of MXenes surfaces is significantly influenced by the presence of –F. Compared to –OH- or –O-functionalized counterparts etched in aqueous media, –F-rich MXenes exhibit enhanced stability against oxidation.[76] However, excessive –F coverage may reduce surface hydrophilicity, as –F is inherently less hydrophilic than –OH and –O groups. Notably, an appropriate amount of –F can promote the migration and penetration of water molecules, thereby improving wetting behavior.[208,209]

Overall, the evolution from –F-rich to –F-free MXenes underscores a trade-off: –F-rich terminations benefit specific applications like membrane filtration and batteries through surface optimization, while –F-free states maximize conductivity for catalysis, and electronic devices.[210] This duality highlights the need for surface engineering to balance property requirements.

This section summarizes the impact of –F termination on MXenes in catalysis and energy conversion/storage devices, drawing insights from triboelectric nanogenerators (TENGs), lithium-sulfur batteries, lithium-ion batteries, and perovskite solar cells. The –F significantly enhances performance by increasing electronegativity, modulating surface electronic structures, stabilizing interfaces, and facilitating ion transport, as demonstrated in various MXene systems such as $Ti_3C_2F_x$, TiOF/Ti_3C_2, and fluorine-rich $Ti_3C_2T_x$.

5.4.3.1. Enhancement of electronegativity and electron absorption. The high electronegativity of fluorine, when introduced as –F on MXenes, makes them excellent electron-accepting materials in triboelectric systems. In Ti_3CN system, for example, the –F extract electrons from nylon during contact, mimicking the behavior of F in fluorinated ethylene propylene (FEP) due to their strong electron-withdrawing tendency (Fig. 29(a)).[211] This is evidenced by the negative electrical output of the –F-functionalized Ti_3CN–alginate composite with nylon (Fig. 29(b)). The resultant electron transfer between nylon and MXene drives the triboelectrification. Consequently, the MXene-based triboelectric nanogenerator (MTENG) assembled with nylon delivers a high open-circuit voltage of 31.25 V and a short-circuit current of 1.15 μA. In contrast, the device with defluorinated MXene (AMTENG) yields only 7.86 V and 0.25 μA, respectively (Fig. 29(c) and (d)). The high-performance and flexible fluorine-functionalized MTENG is capable of powering commercial LED lights (Fig. 29(e)), demonstrating its practical application potential.[22]

5.4.3.2. Creation of electron-deficient sites. The –F termination tunes the electronic structure of MXenes, enhancing their catalytic activity in energy conversion processes. In Li–S batteries, –F-rich TiOF/Ti_3C_2 catalysts derived from MXene fluorination increased positive charge on Ti sites due to O–Ti–F bonds. This Lewis acid–base interaction strengthens polysulfide adsorption and reduces the energy barrier for sulfur reduction reactions (E_a = 14.88 kJ mol^{-1} for TiOF/Ti_3C_2 *vs.* 17.97 kJ mol^{-1} for pristine Ti_3C_2, accelerating liquid–solid conversion kinetics. Consequently, –F-rich MXenes yield a high capacity of 1240 mAh g^{-1} in Li–S batteries, with improved rate capability due to efficient electrocatalysis.[214] Similarly, in

 This journal is © The Royal Society of Chemistry 2026

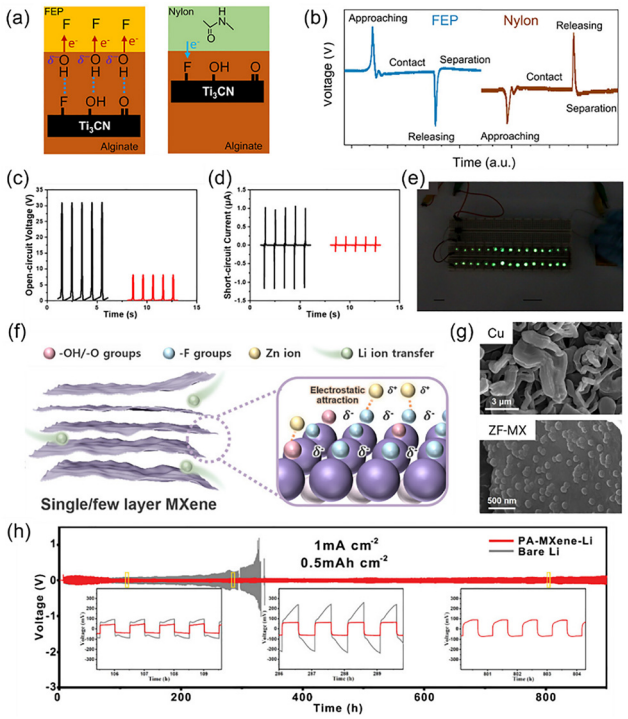

Fig. 29 (a) Schematic diagram of charge transfer in the contact electrification of Ti_3CN with FEP or nylon, (b) voltage curves of Ti_3CN-alginate with FEP and nylon, (c) open-circuit voltage, and (d) short-circuit current of MTENG (black lines) and AMTENG (red lines), (e) LEDs powered by MTENG, (f) schematic diagram of the interaction between Li^+ and the –F-rich MXene surface, (g) SEM image of the material after Li deposition, (h) galvanostatic cycling of symmetric cell. [(a) and (b) Adapted with permission from ref. 211 according to CC-BY. 4.0 Copyright © 2024 American Chemical Society. (c)–(e) Adapted with permission from ref. 22 Copyright © 2023 Wiley-VCH GmbH. (f) and (g) Adapted with permission from ref. 212 Copyright © 2025, American Chemical Society. (h) Adapted with permission from ref. 213 Copyright © 2019 WILEY-VCH Verlag GmbH].

perovskite solar cells, –F-functionalized MXenes passivate defects and suppress ion migration through strong hydrogen bonding (N–H···F), boosting device efficiency to 21.52%. The structure–performance correlation highlights that –F create electron-deficient sites, optimizing MXenes for specific catalytic applications.[215]

5.4.3.3. Improvement of interface stability in batteries. The –F-functionalized MXene possesses a lithiophilic property, guiding the uniform deposition behavior of lithium metal.[216] In lithium metal anodes, Zn^{2+} interacts strongly with the –F on the surface of MXene, thereby acting as a lithiophilic site. –F-rich MXenes guide uniform lithium nucleation by forming a LiF-rich stable solid–electrolyte interphase (SEI) layers through electrochemical reactions, enhancing cyclic longevity (Fig. 29(f)). As shown in Fig. 29(g), during the initial Li deposition, a uniform spherical morphology was exhibited on the entire –F-functionalized ZF-MX surface, thus achieving dense and spherical growth of lithium deposits and avoiding dendritic growth on copper foil under the same conditions.[212] This results in a long cycle life of 900 h with high Coulombic efficiency (>99%) (Fig. 29(h)).[213]

5.4.3.4. Facilitation of ion transport. The –F enhances ion diffusion and nucleation kinetics in electrochemical systems.[217] In sodium-ion batteries, –F-rich MXenes exhibit a low Na^+ diffusion barrier due to the electronegative surface attracting cations, achieving a capacity of 160 mAh g^{-1}, proving that –F-functionalized MXenes can be used in high-power and high-energy sodium batteries.[72]

5.4.4. –F-free MXenes. The development of –F-free MXenes has unlocked new opportunities in catalysis and energy storage devices by eliminating the detrimental effects of –F, such as reduced conductivity and surface inertness. –F-free synthesis routes, including alkali etching, molten salt assisted electrochemical etching, and hydrothermal methods, yield MXenes with dominant –O, –OH, or –Cl terminations, which enhance electronic properties, provide abundant active sites, and improve stability. These terminations facilitate efficient charge transfer, pseudocapacitive reactions, and ion diffusion, leading to superior performance in supercapacitors, batteries, and electrocatalysts compared to their –F-rich counterparts. This section details the key roles of –F-free MXenes in advancing catalysis and energy device applications.

5.4.4.1. Enhancement of electrochemical capacitance for supercapacitors. –F-free MXenes exhibit significantly improved capacitive performance in supercapacitors due to the presence of electrochemically active –O and –OH terminations (eqn (22)).[218–220] For instance, –F-free $Ti_3C_2T_x$ synthesized *via* alkali etching demonstrate a high gravimetric capacitance of 314 F g^{-1} in 1 M H_2SO_4, surpassing –F-rich MXenes by over 200%.[69]

5.4.4.2. Improved stability and cycle life in batteries. –F-free MXenes enhance the cycle life and capacity retention of batteries by avoiding –F-induced side reactions and structural degradation. In lithium-ion batteries, porous –F-free Ti_3C_2 (P-Ti_3C_2) synthesized *via* a chemical-combined ball-milling method exhibits a high reversible capacity of 310 mAh g^{-1} at 100 mA g^{-1}, which is approximately three times that of conventional HF-etched Ti_3C_2 (Fig. 30(a)). The P-Ti_3C_2 electrode demonstrates exceptional long-term cyclability, retaining a capacity of 97 mAh g^{-1} after 3000 cycles at a high current density of 1 A g^{-1}, with nearly 100% capacity retention (Fig. 30(b)). This outperforms –F-rich MXenes, which suffer from rapid capacity fading due to –F-induced side reactions and structural degradation.[221] Similarly, –F-free MoB MBenes anodes retain 144.2 mAh g^{-1} after 1000 cycles at 2 A g^{-1}.[222] The absence of –F also reduces electrode–electrolyte interfacial resistance, as evidenced by electrochemical impedance spectroscopy, leading to longer battery lifespan (Fig. 30(c)).

5.4.4.3. Improvement of electrolyte wettability. –F-free MXenes significantly enhance electrolyte wettability due to their optimized surface chemistry. The replacement of –F with hydrophilic –O and –OH in –F-free-Ti_3C_2 (Ff-Ti_3C_2) improves hydrophilicity, as confirmed by contact angle measurements and ζ-potential analysis.

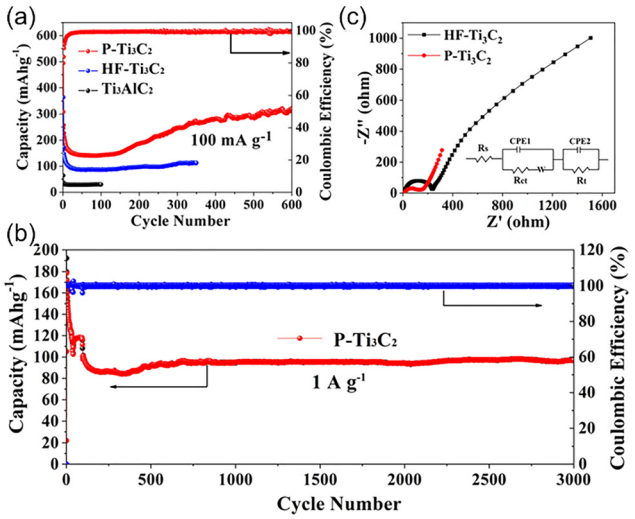

Fig. 30 (a) Cycling performance of –F-free Ti_3C_2 (P-Ti_3C_2) and counterparts at a current density of 100 mA g^{-1}, (b) cycling performance of P-Ti_3C_2 at a current density of 1 A g^{-1}, (c) EIS spectra of P-Ti_3C_2 and HF-Ti_3C_2. [Fig. 30 adapted with permission from ref. 221 Copyright © 2020, American Chemical Society].

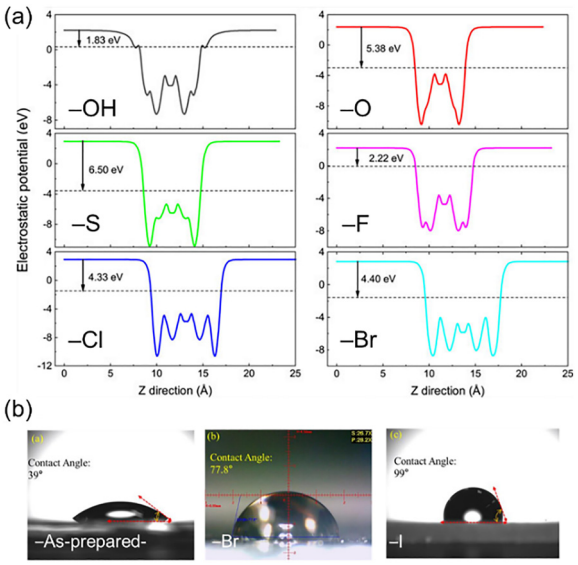

Fig. 31 (a) Calculated electrostatic potentials along the *Z* direction of Nd_2NT_2 (T = –OH, –O, –S, –F, –Cl, and –Br), the work function = $E_{vacuum} - E_F$ is the numerical value shown in the figure, (b) contact angle measurement. [(a) Adapted with permission from ref. 224 Copyright © 2022 Yang, *et al.* (b) Adapted with permission from ref. 225 Copyright © 2024, M. Hilal *et al.*].

The Tyndall effect persists in Ff-Ti_3C_2 suspensions for over 10 days, demonstrating superior colloidal stability. This enhanced wettability facilitates rapid ion transport and uniform electrolyte infiltration, critical for high-performance electrodes. The absence of hydrophobic –F enables efficient electrode–electrolyte interactions, boosting electrochemical kinetics in energy storage devices. The Li–S soft-pack battery involving Ff-Ti_3C_2 exhibits excellent electrochemical performance and remarkable flexibility, achieving an actual weight energy density of 330 Wh kg^{-1} and good cycling performance.[223]

5.4.5. Novel termination MXenes. The strategic engineering of surface terminations in MXenes has evolved beyond conventional T_x (–O, –F, –OH) to encompass a diverse family of novel terminations. This expansion enables precise tuning of electronic properties, catalytic activity, and environmental stability, opening new avenues for applications in energy storage and catalysis. This section highlights structure–property relationships, and emerging applications supported by recent experimental and theoretical advances.

Novel T_x such as heavy halogens (–Cl, –Br, –I), sulfur (–S), and organic groups significantly modulate the fundamental properties of MXenes, enabling tailored electronic, catalytic, and stability behaviors through functionalization engineering.

The introduction of novel T_x drives significant shifts in electronic structure. For instance, –Cl, –Br, and –I terminations on $Ti_3C_2T_x$ MXenes can modify the density of states at the Fermi level to regulate the work function (Fig. 31(a)), band gap, and total magnetic moments of MXenes.[224,226]

Novel T_x profoundly impacts surface chemistry and stability. Halogen terminations, particularly –I, impart hydrophobicity (contact angle up to 99° for I-MXene), which reduces water-induced corrosion and oxidation, enhancing environmental stability (Fig. 31(b)). –I-terminated $Ti_3C_2T_x$ maintains structural integrity for over 80 days in ambient conditions, whereas as-prepared MXenes degrade faster due to higher hydrophilicity.[225] –S can form stable covalent bonds, as in –S–$Mo_{4/3}C$, –S–$W_{4/3}C$, and –S–$Nb_{1.33}C$,[186] where –phSO_3H grafting *via* Ti–O–C linkages expands interlayer spacing from 1.11 nm to 1.69 nm and prevents restacking, leading to improved cyclic stability in capacitive deionization.[227] –N-terminated MXenes show superior oxidation resistance, with oxidation rate constants 13 times lower than Ar-annealed counterparts, due to the formation of protective TiN layers that preserve the Ti–C core.[228] MXenes modified by fluoroalkyl silane or dodecylphosphonic acid also demonstrate long-term humidity stability at room temperature.[229]

The choice of termination profoundly influences electronic conductivity, stability, and interfacial behavior. For instance, Liu *et al.* found that –Br termination leads to a higher Li^+ storage capacity (189 mAh g^{-1}) compared to –F (123 mAh g^{-1}) or –Cl (138 mAh g^{-1}) terminations.[230] In catalysis and energy related applications, it is necessary to customize corresponding T_x to regulate the characteristics of MXenes.

5.4.5.1. –S MXenes. In addition to HER, –S-MXenes demonstrate remarkable capabilities in metal–sulfur battery systems by effectively enhancing redox kinetics, suppressing polysulfide shuttling, and HER side reaction.[234] For Na–S batteries, –S–$Ti_3C_2T_x$ create strong chemical interactions with sodium polysulfides through Ti–S bonds, achieving binding energies of −1.89–4.72 eV for Na_2S_n species, exceeding the corresponding –F and –O counterparts (Fig. 32(a)). Sodium polysulfide molecules preferentially bind to –S–$Ti_3C_2T_x$ instead of –O–$Ti_3C_2T_x$ or –F–$Ti_3C_2T_x$, which means that the –S–$Ti_3C_2T_x$ matrix can prevent shuttle effects. This significantly improves cycle stability, with –S–$Ti_3C_2T_x$/S cathodes maintaining 577 mAh g^{-1} after

 This journal is © The Royal Society of Chemistry 2026

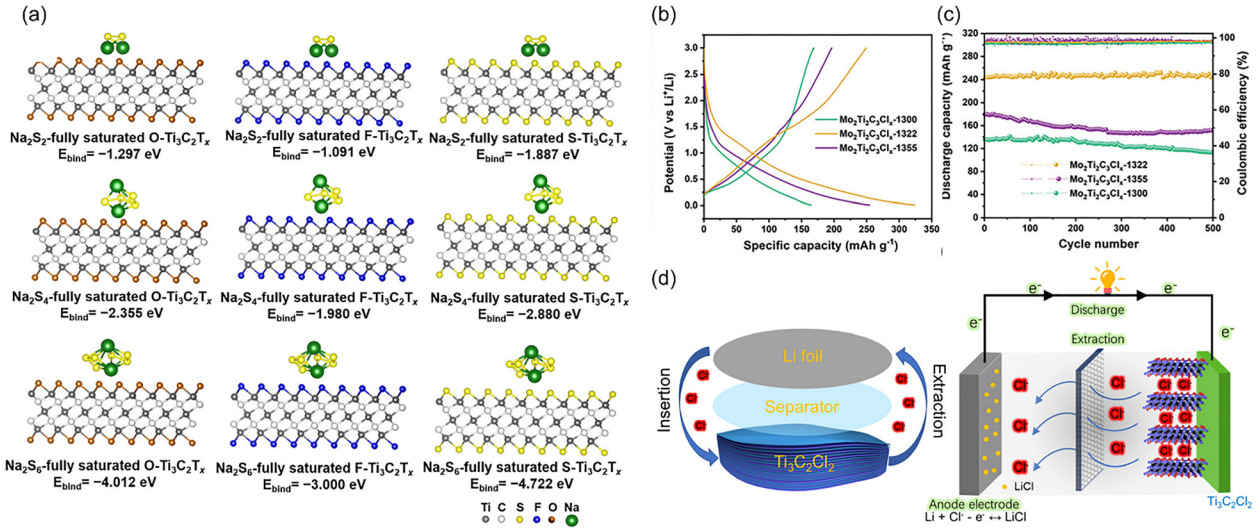

Fig. 32 (a) DFT calculated binding energies of Na_2S_n with $Ti_3C_2T_x$, (b) GCD curves of $Mo_2Ti_2C_3Cl_x$ at 0.2 A g^{-1}, (c) capacity retention and coulombic efficiency at 0.5 A g^{-1}, (d) schematic diagram of pseudocapacitance of Cl-terminated MXenes. [(a) Adapted with permission from ref. 231 Copyright © 2019, American Chemical Society. (b) and (c) Adapted with permission from ref. 232 Copyright © 2024, D. Gandla *et al.* (d) Adapted with permission from ref. 233 Copyright © 2023, American Chemical Society].

500 cycles.[231] Similarly, –F/S coterminated $V_2CF_{0.67}S_{0.33}$ MXenes exhibit enhanced polysulfide anchoring (adsorption energy: 0.8–3.90 eV) and the lowest reported Na_2S decomposition barrier (0.287 eV), enabling efficient sulfur utilization.[235] For Li–S batteries, Mo_2CS_2 MXenes functionalized with transition metal single atoms exhibit metallic conductivity while providing strong LiPSs adsorption *via* TM–S bonds (binding energies: 2.47–3.05 eV for Li_2S_8, Li_2S_6, and Li_2S_4). DFT calculations reveal that these –S-terminated surfaces facilitate Li_2S decomposition with reduced energy barriers as low as 0.540 eV for Fe/SAC, significantly improving reaction kinetics.[236]

5.4.5.2. Heavy halogen-terminated MXenes. Heavy halogen T_x (*e.g.*, –Cl, –Br, –I) on MXenes substantially improve their efficacy in catalysis and energy storage systems by tailoring electronic configurations, surface chemistry, and structural stability. These terminations confer hydrophobicity, mitigate parasitic side reactions, and enhance interfacial ion transport kinetics, rendering them highly suitable for applications such as rechargeable batteries and electrocatalysis. For instance, –Cl-terminated $Ti_3C_2Cl_2$ MXenes produced *via* molten salt or dry etching routes demonstrate high electrical conductivity up to 8000 S cm^{-1} and remarkable environmental stability, retaining performance integrity even under prolonged humid conditions.[237] Beyond conductivity enhancement, MXene–Cl serve as pivotal active sites for Li^+ storage, facilitating ion diffusion by lowering energy barriers and thereby boosting electrochemical performance.[232] In lithium-ion batteries, Ti_2NCl_2-based anodes deliver a reversible capacity of 303.4 mAh g^{-1} over 1200 cycles with negligible capacity fade, owing to minimized Li^+ diffusion barriers and durable Ti–Cl bonding that suppresses structural degradation.[238,239] Similarly, double transition metal MXenes such as $Mo_2Ti_2C_3Cl_x$ achieve a specific capacity of 324 mAh g^{-1} at 0.2 A g^{-1} and maintain 97% capacity retention after 500 cycles at 0.5 A g^{-1} (Fig. 32(b) and (c)).[232] Comparative studies further reveal that –Br-terminated MXenes exhibited superior Li^+ storage capacity (189 mAh g^{-1}) relative to their –F-terminated counterparts, a result of optimized electron distribution and reduced charge transfer resistance.[230]

In capacitive systems, high electrical conductivity –Cl-terminated MXenes are the redox active sites, which facilitate efficient ion intercalation and pseudocapacitive charge storage (Fig. 32(d)):

$$Ti_3C_2Cl_{2-x} + Cl^- - e^- \leftrightarrow Cl\text{–}Ti_3C_2Cl_{2-x} \quad (23)$$

For instance, $Ti_3C_2Cl_2$-based electrodes achieve a gravimetric capacity of 536 mAh g^{-1} with >99.5% Coulombic efficiency over 1000 cycles at 0.2 A g^{-1}, alongside superior rate capability: 153.1 mAh g^{-1} at 1 A g^{-1}, owing to low diffusion barriers and high ion accessibility.[233]

5.4.5.3. Nitrogen-containing groups terminated MXenes. The introduction of nitrogen-containing terminations such as $–NH_2$ or –N onto MXene surfaces represents a strategic approach to tailor their electronic, chemical, and structural properties, which enhances performance in energy storage and catalytic applications. Electronically, nitrogen incorporation optimizes band alignment, and increases the density of states near the Fermi level, thereby facilitating efficient charge transfer. These changes originate from the strong electron-donating character of $–NH_2$, which passivate undercoordinated metal sites and reduce trap states, consequently suppressing non-radiative recombination. As a result, nitrogen-terminated MXenes exhibit superior electrical conductivity up to 17 831 S cm^{-1} after annealing in NH_3, alongside excellent oxidation stability with a 13-fold lower oxidation rate constant compared to Ar-annealed MXenes, and mechanical robustness demonstrated by a tensile strength of 240 MPa in composite films.[134,228,240]

In energy storage applications, these properties lead to high pseudocapacitive performance. For example, $Ti_3C_2N_x$ electrodes achieve specific capacitances of 471 F g^{-1} for H^+ storage, 209 mAh g^{-1} for Li^+, and 79 mAh g^{-1} for Na^+ in both aqueous and non-aqueous electrolytes, owing to improved ion accessibility and reduced diffusion barriers.[241] Specifically, N-modified $Ti_3C_2T_x$–NH_2 films demonstrate a gravimetric capacitance of 415 F g^{-1} at 2 mV s^{-1} in 3 M H_2SO_4, with a rate capacity of 75.9% at 200 mV s^{-1} and cycling stability exceeding 90% retention after 18 000 cycles. The presence of T_x like –NH_2, O–Ti–N, and Ti–O–N synergistically enhances intercalation-pseudocapacitance, with O–Ti–N playing a more significant role in charge storage.[242] Additionally, in photovoltaic devices, $Ti_3C_2T_x$–NH_2 increase charge carrier density and mobility, where extracted charge density rises from 2.4×10^{14} cm^{-3} to 7.3×10^{14} cm^{-3}.[243] This comprehensive optimization underscores the versatility of nitrogen containing-terminated MXenes in advancing next-generation energy technologies.

5.4.5.4. Organic-terminated MXenes. Organic-terminated MXenes with T_x such as benzenesulfonic acid (–phSO_3H) or amino acids (*e.g.*, –L-cysteine) introduces covalent bonds Ti–O–C, Ti–S, or Ti–N that profoundly alter their structural and electronic properties. These modifications expand interlayer spacing from 1.11 nm to 1.69 nm for –phSO_3H-grafted $Ti_3C_2T_x$, mitigate restacking, and enhance hydrophilicity or hydrophobicity depending on the organic moiety. Electronically, electron-donating –SO_3H increase the antibonding orbital occupancy of Ti sites, weakening H adsorption and reducing the Gibbs free energy barrier for reactions.[165] Additionally, organic-functionalization improves oxidation resistance by passivating surface metal atoms and stabilizing the layered framework.[227]

In energy storage, organic-terminated MXenes exhibit superior performance. For instance, –phSO_3H-grafted $Ti_3C_2T_x$ in capacitive deionization delivers a high salt adsorption capacity of 34 mg g^{-1} with 90.7% retention after 25 cycles, owing to expanded ion diffusion pathways and additional Na^+ adsorption sites.[227] In electrocatalysis, L-cysteine–$Ti_3C_2T_x$ achieves a specific capacitance of 279 F g^{-1} in ionic liquid electrolytes, enabling flexible supercapacitors with an energy density of 72.1 Wh kg^{-1}.[244]

5.5. Summary of MXenes T_x in catalysis and energy

The strategic engineering of T_x in MXenes enables precise tuning of their structural, electronic, and chemical properties, which is critical for optimizing performance in catalysis and energy applications. Each type of T_x imparts distinct advantages tailored to specific functionalities. For instance, –OH-rich terminations enhance hydrophilicity and photogenerated charge separation, making them ideal for photocatalytic HER and aqueous electrochemical systems. –O-terminated MXenes exhibit high electrical conductivity and optimized work functions, favoring applications in supercapacitors and electrocatalysis, such as the OER and CO_2 reduction. –F-rich MXenes improve oxidation stability and triboelectric performance, while –F-free variants offer enhanced capacitance and cycling stability in batteries by providing accessible redox-active sites.

Heavy halogen T_x introduces hydrophobicity and high conductivity, benefiting capacitive energy storage and Li–S batteries by facilitating ion transport and polysulfide anchoring. Nitrogen-containing T_x optimize the density of states near the Fermi level, enhancing pseudocapacitance and HER activity. Organic-functionalized MXenes expand interlayer spacing, prevent restacking, and introduce additional ion adsorption sites, advancing capacitive deionization and photocatalytic HER.

Overall, the targeted selection of T_x allows for customization of MXene properties, such as conductivity, stability, and surface reactivity, to meet the demands of specific catalytic and energy storage systems, underscoring the versatility of surface engineering in unlocking next-generation applications.

6. Summary, challenges, and outlooks

6.1. Summary

The strategic engineering of T_x is a cornerstone for unlocking the versatile potential of MXenes in catalysis and energy technologies. As detailed throughout this review, each T_x type confers distinct and tunable physicochemical properties, creating a direct structure–property–performance link. Conventional T_x like –OH, –O, and –F offer foundational benefits: –OH enhance hydrophilicity and mediate hole transfer in photocatalysis, –O optimize electronic conductivity and stability for electrocatalysis and batteries, while –F increases electronegativity, benefiting triboelectric devices and interfacial stability. The expansion to novel T_x, such as heavy halogens (–Cl, –Br, –I), –S, –NH_x, and organic groups, further broadens the functional landscape, enabling tailored light absorption, charge transfer, hydrophobicity, and ion transport. Table 5 concisely maps these induced properties to their best-suited applications and representative performance metrics, highlighting how rational T_x design allows precise customization of MXenes for targeted functions. This capability for precise surface engineering positions MXenes as uniquely adaptable materials, driving advancements in sustainable energy conversion, storage, and catalytic processes. Future progress hinges on mastering mixed-T_x effects and scalable synthesis to fully realize this potential.

6.2. Challenges

6.2.1. Scalable synthesis of MXenes with uniform T_x. A paramount challenge that bridges fundamental research and practical application is the scalable synthesis of MXenes with precisely controlled, uniform T_x. While Sections 4.1 and 4.2 detail sophisticated *in situ* and post-synthetic strategies to achieve specific –O, –OH, –S, or –NH_x surfaces, these methods often involve multi-step processes, harsh conditions (*e.g.*, molten salts, high temperature), or meticulous stoichiometric control, which are inherently difficult to scale uniformly. The dynamic nature of T_x interchange (Section 3.2) further complicates the preservation of a homogeneous surface during large-scale processing and storage. Overcoming this challenge

 This journal is © The Royal Society of Chemistry 2026

Table 5 A concise guide to MXene T_x engineering: structure, property, performance, and application suitability

T_x	Key induced properties	Best-suited applications	Representative performance metrics	Ref.
–OH	• Low work function.	• **Photocatalysis:** as hole-transfer mediator.	• Photocatalysis (H_2): Cu/TiO_2@$Ti_3C_2(OH)_x$ showed significantly enhanced H_2 production rate *vs.* control.	37, 49, 53, 124, 129 and 174
	• Lewis basicity, and hydrophilicity.	• **Photocatalysis:** CO_2 reduction to multi-carbon products.	• Photocatalysis (CO_2 → C_2H_5OH): $Ti_2C(OH)_2$@g-C_3N_4, yield of 784 μmol g^{-1} h^{-1}.	
	• Redox-active sites, and H-bond networks.	• **Electrocatalysis:** HER, NRR, eNO_3^-RR where –OH acts as active site, and H-donor. **Supercapacitors:** for high pseudocapacitance.	• Electrocatalysis (HER): $Ti_4N_3(OH)$, onset potential of −0.26 V *vs.* RHE. Electrocatalysis (NRR): Ti_3C_2 QDs(OH), NH_3 yield of 62.94 μg h^{-1} mg_{cat}^{-1}. Supercapacitors: –OH-rich MXene QDs composite, specific capacitance of 372.2 F g^{-1} at 10 mV s^{-1}.	
	• Increase DOS near Fermi level.	• **Batteries:** as conductive scaffold with ion-activation function.	• Batteries: TBAP@D-$Ti_3C_2T_x$ composite achieves a reversible capacity of 747.7 mAh g^{-1} after 200 cycles at 100 mA g^{-1}.	
–O	• High work function, and opens bandgap.	• **Photocatalysis:** as electron acceptor.	• Photocatalysis (H_2): CdS/Ti_3C_2, H_2 yield of 14 342 μmol h^{-1} g^{-1}.	23, 154, 178, 191 and 206
	• Stable covalent M–O bonds.	• **Electrocatalysis**: stable electrodes in harsh or oxidative environments.	• Electrocatalysis (HER): Rh-Ti_3C_2, better 24-h stability than Pt.	
	• Optimize adsorption energetics.	• **Electrocatalysis:** HER, OER, eNO_3^-RR where optimized intermediate binding is critical.	• Electrocatalysis (eNO_3^-RR): $Ti_3C_2O_x$, FE: 92.8%, NH_3 production rate of 3.278 mg h^{-1} cm^{-2}.	
	• Electron-rich surface.	• **Batteries & supercapacitors**: for high-rate capability, capacity.	• Supercapacitors: $Ti_3C_2T_x$(O), specific capacitance of 554 F g^{-1} at 30 A g^{-1}. Batteries: $Ti_3C_2T_x$(O) anode, capacity retention of 193.9 mAh g^{-1} after 1000 cycles at −20 °C.	
–F	• High electronegativity.	• **TENGs**: as strong electron-accepting layer.	• TENGs: –F-rich Ti_3CN based device, $V_{open\text{-}circuit}$ of 31.25 V, $I_{short\text{-}circuit}$ of 1.15 μA.	22 and 214
	• Induce semiconductor-like transport, reduce conductivity.	• **Batteries**: to modulate Li^+ deposition and stabilize interfaces.	• Li–S batteries: TiOF/Ti_3C_2 achieved the high capacity of 1240 mAh g^{-1} at 0.1C.	
	• Passivates surface.	• Applications requiring antioxidant surfaces.		
Heavy halogens	• Enhance conductivity.	• **Electrocatalysis**: as conductive, stable substrates.	• Li^+ batteries: Ti_2NCl_2-based anodes, reversible capacity of 303.4 mAh g^{-1} over 1200 cycles. $Mo_2Ti_2C_3Cl_x$, specific capacity of 324 mAh g^{-1} at 0.2 A g^{-1}.	166, 232 and 238
	• Up-conversion luminescence.	• **Photocatalysis**: broad-spectrum (visible to NIR) activity.	• Photocatalysis (CO_2 → CH_4): $Ti_3C_2Cl_2$ QDs sensitized system, CH_4 yield of 43.71 (visible) and 6.71 (NIR) μmol g^{-1}.	
–S	• Creates novel active sites of Mo–S, W–S.	• **Electrocatalysis:** Mo–S, W–S motifs for HER.	• Electrocatalysis (HER): –S–$Mo_{4/3}C$, overpotential of 210 mV at 10 mA cm^{-2}, Tafel slope 67 mV dec^{-1}.	186 and 194
	• Enhances charge transfer.	• **Electrocatalysis:** lowers charge-transfer resistance.	• Electrocatalysis (overall water splitting): Ta_2CS_2 nanosheets, overpotentials of 243 mV (OER) and 73 mV (HER) at 10 mA cm^{-2}.	
–NH_x	• Covalent bridging sites.	• **Electrocatalysis:** facilitates strong interfacial coupling in heterostructures (*e.g.*, with COFs).	• Electrocatalysis (CO_2RR): –NH_x–MXene@COF, FE for CO: 97%. Electrocatalysis (ORR): –NH_x–MXene@COF-S, H_2O_2 selectivity >90% in neutral media.	195 and 196
Organic terminations	• Modulates surface electronic structure.	• **Photocatalysis:** weaken Ti–H bonds to facilitate H* desorption, optimize surface reaction kinetics.	• Photocatalysis (H_2): –phSO_3H–$Ti_3C_2T_x$ with TiO_2, H_2 evolution rate of 90.8 μmol h^{-1} g^{-1}.	165

requires innovative engineering of both etching and post-processing protocols to ensure that the precise T_x control demonstrated at the lab scale translates to reproducible, bulk material production without compromising the tailored properties essential for high-performance catalysis and energy devices.

6.2.2. The disconnect between idealized models and actual surfaces. A persistent obstacle in linking the computational design of MXenes to their observed photo/electrochemical performance is the marked disconnect between idealized theoretical models and the chemically heterogeneous nature of as-synthesized surfaces.[68] Experimental studies consistently report MXenes bearing mixed –O, –OH, and –F, yet DFT investigations have often relied on simplified, monomolecular surface models, such as fully –O-terminated $Ti_3C_2O_2$.[68] This approximation, while computationally expedient, can yield misleading descriptors and obscure genuine structure–activity relationships. Illustratively, studies of the hydrogen evolution reaction on Ti_3C_2 demonstrate that thermodynamically stable surfaces under operating conditions are not pure –O or –OH,

but mixed binary or ternary terminations, with catalytic activity highly sensitive to T_x ratios. For instance, while a fully –O-terminated model yields a suboptimal hydrogen adsorption free energy ($\Delta G_H \approx -0.40$ eV), mixed surfaces like $O_{2/3}OH_{1/3}$ approach the ideal $\Delta G_H \approx 0$ eV. This stark contrast underscores how oversimplified models may fail to identify the most active surface motifs present in real materials.

6.2.3. Integration of dynamic environment and hybrid terminal model. These discrepancies are further compounded by the dynamic evolution of surface chemistry in electrochemical environments. Although thermodynamic analyses may favor –O, operational factors, including applied potential, pH, and proton activity, drive reversible protonation/deprotonation processes (eqn (22)) that render surface T_x composition fluid under working conditions.[38,68,245] Consequently, the catalytically relevant interface likely differs from both the as-synthesized state and static computational representations. Overreliance on DFT results derived from pristine, monomolecular models thus risks misinterpretation of functional group contributions.

Addressing this challenge requires moving beyond idealized surface representations. Computational efforts should systematically incorporate mixed-termination models with varying stoichiometries and spatial distributions, while integrating operando conditions such as solvation, interfacial fields, and potential control. Coupled with advanced *in situ* spectroscopic validation, such approaches are essential to reconcile theory and experiment, resolve lingering contradictions, and enable the predictive design of MXene-based electrocatalysts.[68,246]

6.3. Outlooks

6.3.1. New T_x, new properties, new applications, new structure. The exploration of novel T_x beyond conventional –O, –OH, and –F has significantly expanded the property landscape of MXenes. Heavy halogen terminations (*e.g.*, –Cl, –Br, –I) impart enhanced hydrophobicity and environmental stability, as demonstrated by the improved oxidation resistance of –I-terminated $Ti_3C_2T_x$, which can remain stable for over 80 days in ambient conditions. Chalcogen terminations like –S introduce catalytically active sites, enabling efficient HER and sulfur electrocatalysis. Organic T_x, including –phSO_3H, further tailor surface chemistry by expanding interlayer spacing and introducing functional moieties for sensing and energy storage applications. These novel T_x empower MXenes with customized electronic structures, surface properties, and interlayer interactions, unlocking advanced applications in catalysis, energy storage, and optoelectronics that are unattainable with standard terminations. The continuous discovery of new T_x species is thus a fundamental driver for developing next-generation MXene-based technologies with tailored performance metrics. Furthermore, the abundant T_x on MXenes enable the self-assembly of MXenes with other components *via* hydrogen bonding or electrostatic interactions.[247] Building on this, a critical future direction is the integration of T_x-engineered MXenes with single-atom catalysts, 2D materials (*e.g.*, TMDCs, graphene), or other materials (*e.g.*, metal phosphate/phosphide composites, metal chalcogenides) to construct synergistic van der Waals heterostructures.[247–249] This interfacial engineering strategy promotes enhanced charge transfer, tailored band alignment, and novel functionalities in optoelectronics, photocatalysis, and energy storage applications.

6.3.2. Multi-step combinations for purer surfaces. Looking forward, research must prioritize the development of integrated strategies that couple *in situ* synthesis with post-synthetic engineering to achieve precise, pure MXenes surfaces. The field has evolved from simple one-step engineering to sophisticated multi-step approaches, which synergistically combine etching, thermal annealing, chemical substitution, and molecular grafting. These integrated pathways overcome the limitations of single-method processes by enabling sequential control over T_x selection, coverage, and distribution, thereby reducing impurities and enhancing termination purity. For instance, coupling molten salt etching with post-synthetic treatments allows for the targeted removal of unstable T_x (*e.g.*, –F, and –OH) and the enrichment of desired T_x (*e.g.*, –O), leading to surfaces with optimized electronic and chemical properties. However, the pursuit of purity is not merely an aesthetic goal, but a prerequisite for establishing reproducible structure–property relationships. High-purity surfaces are essential to isolate the intrinsic contribution of specific terminations without interference from residual –F or –OH groups. Achieving atomic-level precision in termination control is the necessary foundation for machine learning (ML)-guided inverse design, facilitating the accurate prediction of termination evolution trajectories. This holistic methodology transforms surface engineering from empirical trial-and-error into a deterministic science, driving innovations in MXene-based devices through enhanced reproducibility and functionality.

6.3.3. Interactions and effects of mixed T_x. Unlike many 2D materials such as MoS_2 or hBN, which possess chemically fixed surface terminations, MXenes exhibit an intrinsic and unparalleled richness in surface functional group diversity and dynamism. Mixed T_x, such as the coexistence of –O and –OH, often exhibit synergistic effects that significantly enhance the overall performance of MXenes by leveraging the unique properties and roles of individual functional groups. Each type of termination contributes distinct characteristics: –O improve electrical conductivity and oxidation stability, while –OH enhance hydrophilicity and catalytic activity. When combined, these terminations create a hybrid surface environment that optimizes electronic structure, charge distribution, and interfacial interactions. For instance, in V_2CO_2 MXenes, mixed –O and –OH yield superior HER and OER performance compared to single-T_x systems, as they collectively optimize the Gibbs free energy of intermediate adsorption and facilitate efficient electron transfer.

In energy storage, mixed terminations such as –O/–OH in MXenes improve ion accessibility and redox activity, leading to high pseudocapacitance. The non-thermalized electron dynamics at MXene/molecule interfaces further highlight the role of mixed terminations in enabling efficient charge and heat transfer pathways. By integrating the advantages of individual T_x, such as the stability of –O, the hydrophilicity of –OH,

 This journal is © The Royal Society of Chemistry 2026

and the catalytic activity of –F, mixed T_x strategies tailor MXene surfaces for specific applications, including plasmonic catalysis and interfacial energy conversion. Future research should focus on unraveling the fundamental mechanisms of T_x interactions through combined experimental and computational studies, paving the way for designing advanced MXene-based materials with optimized performance.

While the synergistic effects of mixed T_x open exciting opportunities, rationally designing optimal termination combinations remains challenging due to the vast and complex parameter space. Mixed T_x configurations constitute the native, functional state of MXenes and evolve continuously under realistic electrochemical or catalytic conditions. Rather than serving as inert scaffolds, MXenes behave as self-adaptive catalytic interfaces, with performance likely dictated by the trajectory of termination evolution under operando conditions rather than by any fixed surface composition. Advancing MXene catalysis therefore requires moving beyond static structure–property correlations toward time-resolved mapping of termination pathways, positioning mixed T_x MXenes as chemically programmable platforms whose surfaces are continuously rewritten by their reactive environment.

Machine learning offers a transformative route to decode the dynamic complexity of MXene T_x. By leveraging datasets from DFT and operando experiments, ML models can efficiently map the otherwise intractable relationship between evolving surface chemistry and catalytic performance. Predictive algorithms can identify ideal T_x ensembles, thereby accelerating the design of multifunctional MXenes that synergistically combine the robustness of –O, hydrophilicity of –OH, and reactivity of alternative terminations. To validate these predictions, experimental efforts must employ operando spectroscopies, including ambient-pressure XPS, *in situ* Raman, sum-frequency generation (SFG), and X-ray absorption spectroscopy, complemented by electrochemical quartz crystal microbalance (EQCM) measurements. These techniques collectively capture the real-time trajectory of T_x evolution under working conditions, transforming mixed-T_x. MXenes from passive materials into chemically programmable, self-adaptive catalytic platforms.

In conclusion, the rational design of MXene surface T_x has opened new avenues for customizing properties and enhancing performance across diverse fields. While significant progress has been made in synthesizing and characterizing novel and mixed T_x, future work must address scalability, stability, and the exploration of hybrid functionalities. With continued innovation, T_x-tailored MXenes are poised to drive advancements in sustainable energy technologies and beyond.

Author contributions

Hao Yu conceived and designed the review, and contributed to the manuscript's overall structure and framework. Wenkang Xu led the writing process, coordinated the development of the manuscript, performed a comprehensive literature review, prepared the tables, and designed the figures. Haoran Wang, Xiaoyan An, Changzhuo Xue, and Zhiyang Yu summarized recent research and assisted in revising the manuscript. Chao Peng, Hao-Fan Wang, Yonghai Cao, and Hongjuan Wang provided expertise in energy and catalysis. All authors participated in iterative revisions, co-writing, and ensuring the scientific accuracy of the manuscript. Hao Yu* supervised the project and provided critical insights.

Conflicts of interest

There are no conflicts to declare.

Data availability

No primary research results, software or code have been included and no new data were generated or analyzed as part of this review.

Acknowledgements

This work was supported by the National Natural Science Foundation of China (No. 22272056) and Natural Science Foundation of Guangdong Province (2024B1515040016).

References

1 C. A. Mirkin, E. H. Sargent and D. P. Schrag, *Science*, 2024, **384**, 713.
2 V. Andrei, G. M. Ucoski, C. Pornrungroj, C. Uswachoke, Q. Wang, D. S. Achilleos, H. Kasap, K. P. Sokol, R. A. Jagt, H. Lu, T. Lawson, A. Wagner, S. D. Pike, D. S. Wright, R. L. Z. Hoye, J. L. MacManus-Driscoll, H. J. Joyce, R. H. Friend and E. Reisner, *Nature*, 2022, **608**, 518–522.
3 X. Li, Z. Huang, C. E. Shuck, G. Liang, Y. Gogotsi and C. Zhi, *Nat. Rev. Chem.*, 2022, **6**, 389–404.
4 A. VahidMohammadi, J. Rosen and Y. Gogotsi, *Science*, 2021, **372**, eabf1581.
5 J.-H. Han, J. Park, M. Kim, S. Lee, J. M. Heo, Y. H. Jin, Y. Chae, J. Han, J. Wang, S.-H. Seok, Y. Sim, G. Byun, G.-D. Lee, E. Choi and S.-Y. Kwon, *Adv. Mater.*, 2025, **37**, 2502443.
6 B. Zhang, P. W. Wong, J. Guo, Y. Zhou, Y. Wang, J. Sun, M. Jiang, Z. Wang and A. K. An, *Nat. Commun.*, 2022, **13**, 3315.
7 M. Jiang, D. Wang, Y.-H. Kim, C. Duan, D. V. Talapin and C. Zhou, *Angew. Chem., Int. Ed.*, 2024, **63**, e202409480.
8 L. Huang, L. Ding, Y. Lin, J. Caro, Y. Li and H. Wang, *Adv. Funct. Mater.*, 2025, **36**, e08581.
9 Q. Sun, X. Zhang, P. Gu, X. Liang, Z. Hu, X. Yang, M. Liu, J. Huang and G. Zu, *Adv. Funct. Mater.*, 2024, **34**, 2308537.
10 H. Shin, W. Jeong and T. H. Han, *Nat. Commun.*, 2024, **15**, 10507.
11 A. Thakur, W. J. Highland, B. C. Wyatt, J. Xu, N. Chandran B. S, B. Zhang, Z. D. Hood, S. P. Adhikari, E. Oveisi, B. Pacakova, F. Vega, J. Simon, C. Fruhling, B. Reigle,

M. Asadi, P. P. Michałowski, V. M. Shalaev, A. Boltasseva, T. E. Beechem, C. Liu and B. Anasori, *Nat. Synth.*, 2025, **4**, 888–900.
12 J. Wang, Y. Liu, G. Yang, Y. Jiao, Y. Dong, C. Tian, H. Yan and H. Fu, *Nat. Commun.*, 2025, **16**, 1319.
13 J. Zhang, Y. Zhao, X. Guo, C. Chen, C.-L. Dong, R.-S. Liu, C.-P. Han, Y. Li, Y. Gogotsi and G. Wang, *Nat. Catal.*, 2018, **1**, 985–992.
14 X. Li, Q. Yin, Z. Zhao, Z. Song, Z. Li, M. Shi, H. Wu, X. Guo, Y.-Z. Li, D. Zhao and Y. Sui, *Adv. Energy Mater.*, 2025, **15**, 2502859.
15 Z. Cao, H. Chen, Z. Du, J. Gu, Q. Zhu, B. Li and S. Yang, *Adv. Energy Mater.*, 2022, **12**, 2201189.
16 B. R. P. Yip, C. Chen, Y. Jiang, D. Ohayon, G. C. Bazan and X. Wang, *Nat. Commun.*, 2025, **16**, 7984.
17 C. Zhang, L. McKeon, M. P. Kremer, S.-H. Park, O. Ronan, A. Seral-Ascaso, S. Barwich, C. Ó. Coileáin, N. McEvoy, H. C. Nerl, B. Anasori, J. N. Coleman, Y. Gogotsi and V. Nicolosi, *Nat. Commun.*, 2019, **10**, 1795.
18 L. Liu, S.-J. Zheng, H. Chen, J. Cai and S.-Q. Zang, *Angew. Chem., Int. Ed.*, 2024, **63**, e202316910.
19 Y. Hao, F. Hu, S. Zhu, Y. Sun, H. Wang, L. Wang, Y. Wang, J. Xue, Y.-F. Liao, M. Shao and S. Peng, *Angew. Chem., Int. Ed.*, 2023, **62**, e202304179.
20 Y. Shi, G. Song, B. Yang, Y. Tang, Z. Liu, Z. Zhang, M. Shakouri, J. Cheng and H. Pang, *Adv. Mater.*, 2025, **37**, 2416665.
21 Y. Wang, Z. Shi, M. Luo, Y. Zhai, C. Jing, L. Ding, S. Dai, K.-G. Zhou, L. Li, S. Li, J. Luo, Y. Zhao, W. Wu, Z. Lu, L. Lan, W. Li, Y. Wei and H. Wang, *Nat. Commun.*, 2025, **16**, 10005.
22 L. Jin, Z. Li, H. Huang, X. Chu, W. Deng, J. Zhang, Y. Ao, T. Xu, G. Tian, T. Yang, L. Tang and W. Yang, *Adv. Eng. Mater.*, 2023, **25**, 2300709.
23 X. Sha, X. Song, P. Gao, F. Zeng, Z. Wang, W. Zhou, X. Wu, M. Yu, Z. Shi, J. Liu and C. Jiang, *Nano Energy*, 2025, **144**, 111341.
24 Y. Shin, W. H. Kan, M. Aykol, J. K. Papp, B. D. McCloskey, G. Chen and K. A. Persson, *Nat. Commun.*, 2018, **9**, 4597.
25 S. Wrede, Q. Liu, L. Chen, L. D'Amario, B. Cai, M. Scardamaglia, Z.-B. Zhang, M. Hahlin and H. Tian, *Phys. Chem. Chem. Phys.*, 2025, **27**, 12762–12773.
26 R. Ponce Perez, J. Guerrero Sanchez and M. G. Moreno Armenta, *RSC Adv.*, 2025, **15**, 30156–30164.
27 X. Wei, Y. Liang, H. Shen, H. Zhao, J. Wu, H. Huang, X. Liang, W. Zhou, S. Xu and H. Yu, *Battery Energy*, 2025, **4**, e70017.
28 C. Xie, L. Xu, J. Peng, L. Zhang, X. Wang, J. Deng, M. Capron and V. Ordomsky, *Adv. Funct. Mater.*, 2023, **33**, 2213782.
29 X. Cai, Y. Xiao, B. Zhang, Y. Yang, J. Wang, H. Chen and G. Shen, *Adv. Funct. Mater.*, 2023, **33**, 2304456.
30 T. Zhang, K. A. Mazzio, R. J. Wang, M. Lounasvuori, A. Al-Temimy, F. Amargianou, M.-A. Mawass, F. Kronast, D. M. Többens, K. Lips, T. Petit and Y. Gogotsi, *Nat. Commun.*, 2025, **16**, 7447.
31 R. A. Kumar and J. V. Rohit, *FlatChem*, 2025, **53**, 100922.
32 K. Tang, S. Liu, Y. Huang, J. Zhou and Z. Sun, *Surf. Interfaces*, 2025, **76**, 107866.
33 H. Wang, W. Jiang, X. Ma, R. Ma, X. Zhang, Y. Fang, M. Jiao and Z. Zhou, *Chem. Commun.*, 2025, **61**, 17621–17624.
34 F. Yu, Z. Zhou, Y. You, J. Zhan, T. Yao and L.-H. Zhang, *ACS Appl. Mater. Interfaces*, 2023, **15**, 24346–24353.
35 X. Liu, J. Zhang, J. Xu, Y. Li, Y. Du, Y. Jiang and K. Lin, *J. Colloid Interface Sci.*, 2023, **633**, 992–1001.
36 X. Pan, X. Yang, M. Yu, X. Lu, H. Kang, M.-Q. Yang, Q. Qian, X. Zhao, S. Liang and Z. Bian, *Nat. Commun.*, 2023, **14**, 4183.
37 Z. Jin, C. Liu, Z. Liu, J. Han, Y. Fang, Y. Han, Y. Niu, Y. Wu, C. Sun and Y. Xu, *Adv. Energy Mater.*, 2020, **10**, 2000797.
38 J. L. Hart, K. Hantanasirisakul, A. C. Lang, B. Anasori, D. Pinto, Y. Pivak, J. T. van Omme, S. J. May, Y. Gogotsi and M. L. Taheri, *Nat. Commun.*, 2019, **10**, 522.
39 J. Wang, Z. Zhang, J. Shen, M. Zhang, L. Niu and L. Bai, *J. Phys. Chem. C*, 2023, **127**, 18067–18075.
40 D. Zhang, S. Wang, R. Hu, J. Gu, Y. Cui, B. Li, W. Chen, C. Liu, J. Shang and S. Yang, *Adv. Funct. Mater.*, 2020, **30**, 2002471.
41 M. Khazaei, M. Arai, T. Sasaki, C.-Y. Chung, N. S. Venkataramanan, M. Estili, Y. Sakka and Y. Kawazoe, *Adv. Funct. Mater.*, 2013, **23**, 2185–2192.
42 K. Yusupov, J. Björk and J. Rosen, *Nanoscale Adv.*, 2023, **5**, 3976–3984.
43 Y. Liu, H. Xiao and W. A. Goddard, III, *J. Am. Chem. Soc.*, 2016, **138**, 15853–15856.
44 S. W. Koh, L. Rekhi, A. Arramel, M. D. Birowosuto, Q. T. Trinh, J. Ge, W. Yu, A. T. S. Wee, T. S. Choksi and H. Li, *ACS Appl. Mater. Interfaces*, 2024, **16**, 66826–66836.
45 Y. Tian, P. Hou, H. Zhang, Y. Xie, G. Chen, Q. Li, F. Du, A. Vojvodic, J. Wu and X. Meng, *Nat. Commun.*, 2024, **15**, 10099.
46 F. Cao, Y. Zhang, H. Wang, K. Khan, A. K. Tareen, W. Qian, H. Zhang and H. Ågren, *Adv. Mater.*, 2022, **34**, 2107554.
47 P. Tian, G. Yu, K. Wei, Z. Zhang and N. Wang, *Ceram. Int.*, 2021, **47**, 30722–30728.
48 Z. Zhou, F. Yu, Y. You, J. Zhan and L.-H. Zhang, *Inorg. Chem. Front.*, 2023, **10**, 5371–5378.
49 E. Pranada, B. Ngozichukwu, R. Yoo, D. Johnson, M. A. Barteau, A. Abdel-Wahab and A. Djire, *ACS Catal.*, 2025, **15**, 982–991.
50 Y. Ge, Y. Hu, X. Ma, Y. Chen, J. He, L. Jiang, Z. Yan and J. Wang, *ACS Appl. Nano Mater.*, 2024, **7**, 1233–1244.
51 Y. Luo, W. Que, Y. Tang, Y. Kang, X. Bin, Z. Wu, B. Yuliarto, B. Gao, J. Henzie and Y. Yamauchi, *ACS Nano*, 2024, **18**, 11675–11687.
52 M. R. Lukatskaya, S. Kota, Z. Lin, M.-Q. Zhao, N. Shpigel, M. D. Levi, J. Halim, P.-L. Taberna, M. W. Barsoum, P. Simon and Y. Gogotsi, *Nat. Energy*, 2017, **2**, 17105.
53 C. Peng, P. Wei, X. Li, Y. Liu, Y. Cao, H. Wang, H. Yu, F. Peng, L. Zhang, B. Zhang and K. Lv, *Nano Energy*, 2018, **53**, 97–107.
54 Y. Wei, P. Zhang, R. A. Soomro, Q. Zhu and B. Xu, *Adv. Mater.*, 2021, **33**, 2103148.

 This journal is © The Royal Society of Chemistry 2026

55 K. Arole, S. A. Micci-Barreca, S. Athavale, M. Tajedini, G. Raghuvaran, J. L. Lutkenhaus, M. Radovic, H. Liang and M. J. Green, *ACS Appl. Mater. Interfaces*, 2024, **16**, 6290–6300.

56 X. Chen, Y. Zhu, M. Zhang, J. Sui, W. Peng, Y. Li, G. Zhang, F. Zhang and X. Fan, *ACS Nano*, 2019, **13**, 9449–9456.

57 C. Hu, Z. Wei, L. Li and G. Shen, *Adv. Funct. Mater.*, 2023, **33**, 2302188.

58 Q. Tang, Z. Zhou and P. Shen, *J. Am. Chem. Soc.*, 2012, **134**, 16909–16916.

59 B. Anasori, M. R. Lukatskaya and Y. Gogotsi, *Nat. Rev. Mater.*, 2017, **2**, 16098.

60 M. Naguib, M. Kurtoglu, V. Presser, J. Lu, J. Niu, M. Heon, L. Hultman, Y. Gogotsi and M. W. Barsoum, *Adv. Mater.*, 2011, **23**, 4248–4253.

61 M. Ghidiu, M. R. Lukatskaya, M.-Q. Zhao, Y. Gogotsi and M. W. Barsoum, *Nature*, 2014, **516**, 78–81.

62 V. Kamysbayev, A. S. Filatov, H. Hu, X. Rui, F. Lagunas, D. Wang, R. F. Klie and D. V. Talapin, *Science*, 2020, **369**, 979–983.

63 H. Shi, P. Zhang, Z. Liu, S. Park, M. R. Lohe, Y. Wu, A. Shaygan Nia, S. Yang and X. Feng, *Angew. Chem., Int. Ed.*, 2021, **60**, 8689–8693.

64 L. Liu, H. Zschiesche, M. Antonietti, B. Daffos, N. V. Tarakina, M. Gibilaro, P. Chamelot, L. Massot, B. Duployer, P.-L. Taberna and P. Simon, *Adv. Energy Mater.*, 2023, **13**, 2202709.

65 M. Alhabeb, K. Maleski, B. Anasori, P. Lelyukh, L. Clark, S. Sin and Y. Gogotsi, *Chem. Mater.*, 2017, **29**, 7633–7644.

66 M. A. Hope, A. C. Forse, K. J. Griffith, M. R. Lukatskaya, M. Ghidiu, Y. Gogotsi and C. P. Grey, *Phys. Chem. Chem. Phys.*, 2016, **18**, 5099–5102.

67 J. Peng, X. Chen, W.-J. Ong, X. Zhao and N. Li, *Chem*, 2019, **5**, 18–50.

68 R. Ibragimova, M. J. Puska and H.-P. Komsa, *ACS Nano*, 2019, **13**, 9171–9181.

69 T. Li, L. Yao, Q. Liu, J. Gu, R. Luo, J. Li, X. Yan, W. Wang, P. Liu, B. Chen, W. Zhang, W. Abbas, R. Naz and D. Zhang, *Angew. Chem., Int. Ed.*, 2018, **57**, 6115–6119.

70 J. Yoon, S. Kim, K. H. Park, S. Lee, S. J. Kim, H. Lee, T. Oh and C. M. Koo, *Small Methods*, 2023, **7**, 2201579.

71 W. Xu, Z. Shi, Z. Yu, C. Peng, G. Yang, H.-F. Wang, J. Huang, Y. Cao, H. Wang, L. Li and H. Yu, *Nano Lett.*, 2024, **24**, 10547–10553.

72 V. Natu, R. Pai, M. Sokol, M. Carey, V. Kalra and M. W. Barsoum, *Chem*, 2020, **6**, 616–630.

73 D. Meng, M. Xu, S. Li, M. Ganesan, X. Ruan, S. K. Ravi and X. Cui, *Small*, 2024, **20**, 2304483.

74 P. Zhang, H. Shou, Y. Xia, C. Wang, S. Wei, W. Xu, Y. Chen, Z. Liu, X. Guo, K. Zhu, Y. Cao, X. Wu, S. Chen and L. Song, *Nano Lett.*, 2023, **23**, 1401–1408.

75 T. Schultz, N. C. Frey, K. Hantanasirisakul, S. Park, S. J. May, V. B. Shenoy, Y. Gogotsi and N. Koch, *Chem. Mater.*, 2019, **31**, 6590–6597.

76 J. Björk and J. Rosen, *Chem. Mater.*, 2021, **33**, 9108–9118.

77 I. Persson, L.-Å. Näslund, J. Halim, M. W. Barsoum, V. Darakchieva, J. Palisaitis, J. Rosen and P. O. Å. Persson, *2D Mater.*, 2018, **5**, 015002.

78 J. L. Hart, K. Hantanasirisakul, Y. Gogotsi and M. L. Taheri, *ACS Nanosci. Au*, 2022, **2**, 433–439.

79 M. Shekhirev, C. E. Shuck, A. Sarycheva and Y. Gogotsi, *Prog. Mater. Sci.*, 2021, **120**, 100757.

80 V. Natu, M. Benchakar, C. Canaff, A. Habrioux, S. Célérier and M. W. Barsoum, *Matter*, 2021, **4**, 1224–1251.

81 Z. Dessoliers, A. Chemin, G. Valurouthu, R. Lord, T. Bilyk, Y. Gogotsi, V. Mauchamp and T. Petit, *Adv. Mater. Interfaces*, 2025, **12**, 2500391.

82 Y. Li, H. Shao, Z. Lin, J. Lu, L. Liu, B. Duployer, P. O. Å. Persson, P. Eklund, L. Hultman, M. Li, K. Chen, X.-H. Zha, S. Du, P. Rozier, Z. Chai, E. Raymundo-Piñero, P.-L. Taberna, P. Simon and Q. Huang, *Nat. Mater.*, 2020, **19**, 894–899.

83 W. Xu, Z. Yu, H. Yang, X. An, C. Peng, G. Yang, H.-F. Wang, Y. Cao, H. Wang and H. Yu, *Small*, 2026, **22**, e13542.

84 A. S. Racz and M. Menyhard, *Appl. Surf. Sci. Adv.*, 2025, **30**, 100872.

85 T. Guo, D. Zhou, S. Deng, M. Jafarpour, J. Avaro, A. Neels, J. Heier and C. Zhang, *ACS Nano*, 2023, **17**, 3737–3749.

86 V. Natu and M. W. Barsoum, *J. Phys. Chem. C*, 2023, **127**, 20197–20206.

87 T. Bashir, S. A. Ismail, J. Wang, W. Zhu, J. Zhao and L. Gao, *J. Energy Chem.*, 2023, **76**, 90–104.

88 F. Brette, D. Kourati, M. Paris, L. Loupias, S. Célérier, T. Cabioc'h, M. Deschamps, F. Boucher and V. Mauchamp, *J. Am. Chem. Soc.*, 2023, **145**, 4003–4014.

89 T. Kobayashi, Y. Sun, K. Prenger, D.-E. Jiang, M. Naguib and M. Pruski, *J. Phys. Chem. C*, 2020, **124**, 13649–13655.

90 S. Kajiyama, L. Szabova, K. Sodeyama, H. Iinuma, R. Morita, K. Gotoh, Y. Tateyama, M. Okubo and A. Yamada, *ACS Nano*, 2016, **10**, 3334–3341.

91 S. Sunny, Y. Coppel, P. L. Taberna and P. Simon, *J. Electrochem. Soc.*, 2024, **171**, 030512.

92 A. Çelik, Y. Aksoy, Ö. Hanay, M. Yegin, Y. Köse, K. Demirelli and H. Hasar, *J. Appl. Electrochem.*, 2025, **55**, 1281–1294.

93 Z. Li, L. Wang, D. Sun, Y. Zhang, B. Liu, Q. Hu and A. Zhou, *Mater. Sci. Eng., B*, 2015, **191**, 33–40.

94 H.-W. Wang, M. Naguib, K. Page, D. J. Wesolowski and Y. Gogotsi, *Chem. Mater.*, 2016, **28**, 349–359.

95 Y. Ying, Y. Liu, X. Wang, Y. Mao, W. Cao, P. Hu and X. Peng, *ACS Appl. Mater. Interfaces*, 2015, **7**, 1795–1803.

96 S. Kumar, *Small*, 2024, **20**, 2308225.

97 F. Tian, Z. Pang, X. Yu, Z. Jiang, F. Wang, J. Xu, G. Li, S. Hu, Q. Xu, H.-Y. Hsu, Y. Zhao, L. Ji, X. Lu and X. Zou, *Angew. Chem., Int. Ed.*, 2025, **64**, e202514594.

98 X. Zhang, Z. Ni, X. Bai, H. Shen, Z. Wang, C. Wei, K. Tian, B. Xi, S. Xiong and J. Feng, *Adv. Energy Mater.*, 2023, **13**, 2301349.

99 J. Chen, M. Chen, W. Zhou, X. Xu, B. Liu, W. Zhang and C. Wong, *ACS Nano*, 2022, **16**, 2461–2470.

100 L. Liu, E. Raymundo-Piñero, P.-L. Taberna and P. Simon, *Electrochem. Commun.*, 2023, **148**, 107453.
101 S. Yang, P. Zhang, F. Wang, A. G. Ricciardulli, M. R. Lohe, P. W. M. Blom and X. Feng, *Angew. Chem., Int. Ed.*, 2018, **57**, 15491–15495.
102 A. Jawaid, A. Hassan, G. Neher, D. Nepal, R. Pachter, W. J. Kennedy, S. Ramakrishnan and R. A. Vaia, *ACS Nano*, 2021, **15**, 2771–2777.
103 G. Li, L. Tan, Y. Zhang, B. Wu and L. Li, *Langmuir*, 2017, **33**, 9000–9006.
104 A. A. Mayyahi, S. Sarker, B. M. Everhart, X. He and P. B. Amama, *Mater. Today Commun.*, 2022, **32**, 103835.
105 T. Thomas, S. Pushpan, J. A. Aguilar Martínez, A. Torres Castro, N. Pineda Aguilar, A. Álvarez-Méndez and K. C. Sanal, *Ceram. Int.*, 2021, **47**, 35384–35387.
106 J. Mei, G. A. Ayoko, C. Hu, J. M. Bell and Z. Sun, *Sustainable Mater. Technol.*, 2020, **25**, e00156.
107 C. Peng, P. Wei, X. Chen, Y. Zhang, F. Zhu, Y. Cao, H. Wang, H. Yu and F. Peng, *Ceram. Int.*, 2018, **44**, 18886–18893.
108 Y. Zheng, Y. Wang, D. Liu, J. Zhao and Y. Li, *Angew. Chem., Int. Ed.*, 2025, **64**, e202415742.
109 M. Seredych, C. E. Shuck, D. Pinto, M. Alhabeb, E. Precetti, G. Deysher, B. Anasori, N. Kurra and Y. Gogotsi, *Chem. Mater.*, 2019, **31**, 3324–3332.
110 K. R. G. Lim, M. Shekhirev, B. C. Wyatt, B. Anasori, Y. Gogotsi and Z. W. Seh, *Nat. Synth.*, 2022, **1**, 601–614.
111 I. Persson, J. Halim, H. Lind, T. W. Hansen, J. B. Wagner, L.-Å. Näslund, V. Darakchieva, J. Palisaitis, J. Rosen and P. O. Å. Persson, *Adv. Mater.*, 2019, **31**, 1805472.
112 H. Xu, R. Zheng, D. Du, L. Ren, R. Li, X. Wen, C. Zhao and C. Shu, *Appl. Mater. Today*, 2022, **27**, 101464.
113 T. Zhang, P.-Y. Cao, Q. Wang, B. Yang, H. Wan, L. Chang, G. Zhang, Q. Jin, Y. Deng, C. Yang, Y. Wang, Y.-C. Han, T. Ding and X. Xiao, *Fundam. Res.*, 2025, DOI: 10.1016/j.fmre.2025.10.005.
114 R. B. Rakhi, B. Ahmed, M. N. Hedhili, D. H. Anjum and H. N. Alshareef, *Chem. Mater.*, 2015, **27**, 5314–5323.
115 J. Halim, I. Persson, P. Eklund, P. O. Å. Persson and J. Rosen, *RSC Adv.*, 2018, **8**, 36785–36790.
116 Y. Chi, Y. Xu, C. Xu, J. Tian, Y. Li, B. Gu, H. Song and H. Zhang, *Ind. Eng. Chem. Res.*, 2022, **61**, 9054–9066.
117 F. H. Fagerli, Z. Wang, T. Grande, H. Kaland, S. M. Selbach, N. P. Wagner and K. Wiik, *ACS Omega*, 2022, **7**, 23790–23799.
118 J. Halim, K. M. Cook, M. Naguib, P. Eklund, Y. Gogotsi, J. Rosen and M. W. Barsoum, *Appl. Surf. Sci.*, 2016, **362**, 406–417.
119 Y. Xie, M. Naguib, V. N. Mochalin, M. W. Barsoum, Y. Gogotsi, X. Yu, K.-W. Nam, X.-Q. Yang, A. I. Kolesnikov and P. R. C. Kent, *J. Am. Chem. Soc.*, 2014, **136**, 6385–6394.
120 Q. Peng, J. Guo, Q. Zhang, J. Xiang, B. Liu, A. Zhou, R. Liu and Y. Tian, *J. Am. Chem. Soc.*, 2014, **136**, 4113–4116.
121 J. Li, X. Yuan, C. Lin, Y. Yang, L. Xu, X. Du, J. Xie, J. Lin and J. Sun, *Adv. Energy Mater.*, 2017, **7**, 1602725.
122 Y. Luo, Z. Weng, Y. Lin, B. Han, X. Ou, Y. Zhou and J. Jiang, *Environ. Sci.: Nano*, 2022, **9**, 3385–3396.
123 Y. Meng, P. Zeng, X.-Y. Yang, Z. Liu, X.-Y. Li, C.-F. Ye, Y. Li, J.-P. Liu, B.-L. Su, L.-H. Chen and Y.-L. Wang, *Chem. Eng. J.*, 2023, **466**, 143372.
124 C. Guo, Y. Zhang, M. Yao, Y. Cao, Q. Feng and Y. Wang, *ACS Appl. Mater. Interfaces*, 2022, **14**, 29974–29985.
125 R. Eslami, N. Azizi, P. Santhirakumaran, M. Mehrvar and H. Zarrin, *Chem. Eng. J.*, 2024, **480**, 148063.
126 Y. Wang, Z. Fan, Y. Wan, M. Xu, J. Li, Y. Ling, Y. Xie, K. Yang and X. Li, *Appl. Catal., B*, 2025, **366**, 125017.
127 S. Wei, Y. Fu, P. Roy, X. Tong, H. Yue, M. Liu, H. N. Jaiswal, S. Shahi, Y. I. Gata, T. Butler, H. Li, Q. Jia and F. Yao, *ACS Appl. Mater. Interfaces*, 2022, **14**, 35673–35681.
128 R. Cheng, J. Wang, T. Hu, Y. Zhao, Y. Liang, X. Wang and Y. Zhou, *J. Mater. Sci. Technol.*, 2023, **165**, 219–224.
129 M. S. Sulabha, V. Arunachaleshwar and B. M. J. Ali, *Appl. Surf. Sci.*, 2025, **686**, 162104.
130 H. Li, C. Ma, M. Gao, Y. Li, L. Xie, D. Zhao, R. Zhang, G. Zhang, W. Li, R. Rong and B. Kong, *Anal. Bioanal. Chem.*, 2022, **414**, 8447–8461.
131 Y. Hu, Y. Liu, C. Cui, W. Cai, C. Ma, R. Min, A. Wang, Y. Yang, S. Zhang and J. Jiang, *Compos. Sci. Technol.*, 2026, **273**, 111426.
132 F. Ai, C. Fu, G. Cheng, H. Zhang, Y. Feng, X. Yan and X. Zheng, *ACS Appl. Nano Mater.*, 2021, **4**, 8192–8199.
133 J. Wan, R. Wu, Y. Chen, H. Zhang, H. Li, B. Wang, T. Liskiewicz and S. Shi, *Appl. Surf. Sci.*, 2024, **678**, 161154.
134 M. Peng, M. Dong, W. Wei, H. Xu, C. Liu and C. Shen, *Carbon*, 2021, **179**, 400–407.
135 Y. Ma, Y. Hu, Y. Wang, J. Yu, S. Song and Z. Hu, *ACS Appl. Nano Mater.*, 2024, **7**, 23485–23493.
136 X. Jin, D. Mo, L. Feng, D. Wang, B. Su and X. Guo, *Nano Res.*, 2025, **18**, 94907092.
137 H. Zhang, H. Ding, W. Wang, J. Zhao, B. Sun, Y. Xia, G. Li and X. Chang, *Mater. Today Energy*, 2024, **44**, 101623.
138 Z. Zhang, J. Liu, H. Du, X. Zhao, H. Sun, M. Yang and J. Chu, *Chem. Eng. J.*, 2024, **484**, 149620.
139 H. Shin, H. Lee, Y. Seo, W. Jeong and T. H. Han, *Langmuir*, 2023, **39**, 2358–2367.
140 T. Yousaf, A. Areeb, M. Murtaza, A. Munir, Y. Khan and A. Waseem, *ACS Omega*, 2022, **7**, 19502–19512.
141 H. Jing, H. Yeo, B. Lyu, J. Ryou, S. Choi, J.-H. Park, B. H. Lee, Y.-H. Kim and S. Lee, *ACS Nano*, 2021, **15**, 1388–1396.
142 K. Zhao, J. Liu, X. Wang, Q. Che, B. Zhang, H. He, K. Wang and Y. Chen, *Adv. Opt. Mater.*, 2024, **12**, 2301761.
143 Y. Liu, Z. Dai, W. Zhang, Y. Jiang, J. Peng, D. Wu, B. Chen, W. Wei, X. Chen, Z. Liu, Z. Wang, F. Han, D. Ding, L. Wang, L. Li, Y. Yang and Y. Huang, *ACS Nano*, 2021, **15**, 9065–9075.
144 B. Zhu, K. Wang, H. Gao, Q. Wang, X. Pan and M. Fan, *ChemPhysChem*, 2021, **22**, 1675–1683.
145 T. Sun, S. Wang, M. Xu, N. Qiao, Q. Zhu and B. Xu, *ACS Appl. Mater. Interfaces*, 2024, **16**, 10093–10103.
146 M. Khazaei, M. Arai, T. Sasaki, A. Ranjbar, Y. Liang and S. Yunoki, *Phys. Rev. B*, 2015, **92**, 075411.
147 C. Peng, X. Xie, W. Xu, T. Zhou, P. Wei, J. Jia, K. Zhang, Y. Cao, H. Wang, F. Peng, R. Yang, X. Yan, H. Pan and H. Yu, *Chem. Eng. J.*, 2021, **421**, 128766.

 This journal is © The Royal Society of Chemistry 2026

148 W. Xu, X. Li, C. Peng, G. Yang, Y. Cao, H. Wang, F. Peng and H. Yu, *Appl. Catal., B*, 2022, **303**, 120910.
149 C. Peng, T. Zhou, P. Wei, H. Ai, B. Zhou, H. Pan, W. Xu, J. Jia, K. Zhang, H. Wang and H. Yu, *Chem. Eng. J.*, 2022, **439**, 135685.
150 H. Ahmad, M. E. Hossain, M. A. Azeem, B. A. Alaqil and T. N. Baroud, *J. Membr. Sci.*, 2025, **736**, 124635.
151 S. Cheng, Q. Xiong, C. Zhao and X. Yang, *Chin. J. Struct. Chem.*, 2022, **41**, 2208058–2208064.
152 N. Kumar and F. Karlický, *Appl. Phys. Lett.*, 2023, **122**, 183102.
153 D.-G. Wei, X.-Y. Chen, Z.-H. Liu, Y. Zhao, Y.-T. Pang, C.-J.-Y. Wang and C.-B. Yao, *Appl. Surf. Sci.*, 2026, **717**, 164794.
154 J. Ran, G. Gao, F.-T. Li, T.-Y. Ma, A. Du and S.-Z. Qiao, *Nat. Commun.*, 2017, **8**, 13907.
155 S. Zhou, L. Jiang, H. Wang, J. Yang, X. Yuan, H. Wang, J. Liang, X. Li, H. Li and Y. Bu, *Adv. Funct. Mater.*, 2023, **33**, 2307702.
156 H. Zhang, X. Zhang, C. Xie, W. Shi and P. Yang, *Environ. Res.*, 2023, **227**, 115793.
157 K. Liu, L. Wang, T. Fu, H. Zhang, C. Lu, Z. Tong, Y. Yang and Y. Peng, *Chem. Eng. J.*, 2023, **457**, 141271.
158 I. A. Navid, Z. Ye, Y. Pan, Y. Shen, T. Norris and Z. Mi, *J. Mater. Chem. A*, 2025, **13**, 31642–31653.
159 H. Fang, A. Thakur, A. Zahmatkeshsaredorahi, Z. Fang, V. Rad, A. A. Shamsabadi, C. Pereyra, M. Soroush, A. M. Rappe, X. G. Xu, B. Anasori and Z. Fakhraai, *Proc. Natl. Acad. Sci. U. S. A.*, 2024, **121**, e2400084121.
160 X. Zhao, D. E. Holta, Z. Tan, J.-H. Oh, I. J. Echols, M. Anas, H. Cao, J. L. Lutkenhaus, M. Radovic and M. J. Green, *ACS Appl. Nano Mater.*, 2020, **3**, 10578–10585.
161 J. Li, D. Zhang, Z. Hu and Z. Yuan, *Nat. Catal.*, 2025, **8**, 1268–1280.
162 B. Vénosová and F. Karlický, *Nanoscale*, 2025, **17**, 24529–24540.
163 S. Saharan, U. Ghanekar and S. Meena, *Phys. Scr.*, 2023, **98**, 095521.
164 D. Bury, M. Jakubczak, M. A. K. Purbayanto, A. Wojciechowska, D. Moszczyńska and A. M. Jastrzębska, *Small Methods*, 2023, **7**, 2201252.
165 T. Chen, P. Wang, X. Wang and F. Chen, *Int. J. Hydrogen Energy*, 2026, **202**, 152869.
166 C.-M. Fung, B.-J. Ng, Y.-H. Chew, C.-C. Er, J. Low, X. Guo, X. Y. Kong, L.-L. Tan, H. Onishi, A. R. Mohamed and S.-P. Chai, *Cell Rep. Phys. Sci.*, 2024, **5**, 102296.
167 A. D. Handoko, K. D. Fredrickson, B. Anasori, K. W. Convey, L. R. Johnson, Y. Gogotsi, A. Vojvodic and Z. W. Seh, *ACS Appl. Energy Mater.*, 2018, **1**, 173–180.
168 X. Sang, Y. Xie, M.-W. Lin, M. Alhabeb, K. L. Van Aken, Y. Gogotsi, P. R. C. Kent, K. Xiao and R. R. Unocic, *ACS Nano*, 2016, **10**, 9193–9200.
169 B. Jiang, T. Yang, T. Wang, C. Chen, M. Yang, X. Yang, J. Zhang and Z. Kou, *Chem. Eng. J.*, 2022, **442**, 136119.
170 B.-Z. Guo, S.-B. Kim, S.-Y. Lee and S.-J. Park, *Carbon*, 2025, **231**, 119732.
171 J. Xia, S.-Z. Yang, B. Wang, P. Wu, I. Popovs, H. Li, S. Irle, S. Dai and H. Zhu, *Nano Energy*, 2020, **72**, 104681.
172 P. Hou, Y. Tian, Y. Xie, Q. Li, G. Chen, F. Du, J. Wu, Y. Ma and X. Meng, *Angew. Chem., Int. Ed.*, 2024, **63**, e202411849.
173 Y. Liu, Y. Tian, F. Liu, T. Gu, B. Wang, J. He, C. Wang, X. Meng, P. Sun and G. Lu, *Adv. Sci.*, 2024, **11**, 2404178.
174 Y. Zhu and X. Li, *Nanoscale*, 2025, **17**, 27923–27932.
175 J. Liu, J. Yang, X. Tang, R. Tian, G. Zhang, J. Yang, Y. Jiang and Y. Sun, *J. Mater. Chem. A*, 2025, **13**, 37581–37594.
176 Q. Shan, Q. Ding and W. Wu, *Ind. Eng. Chem. Res.*, 2023, **62**, 9492–9502.
177 E. Thirugnanasambandam, S. Ren, R. Zhang, H. Yang, R. Xing and S. Liu, *Appl. Surf. Sci.*, 2025, **703**, 163402.
178 A. S. Zverev, C. Penschke, L. Cancellara, S. Reinicke, C. Günter, S. Rüstig, N. Deepak, S. Kogikoski Jr, P. Saalfrank and I. Bald, *Small*, 2026, **22**, e10349.
179 Y. Jiang, T. Sun, X. Xie, W. Jiang, J. Li, B. Tian and C. Su, *ChemSusChem*, 2019, **12**, 1368–1373.
180 N. Xue, X. Li, L. Han, H. Zhu, X. Zhao, J. Zhuang, Z. Gao and X. Tao, *J. Mater. Chem. A*, 2022, **10**, 7960–7967.
181 Y. Guo, T. Wang, Q. Yang, X. Li, H. Li, Y. Wang, T. Jiao, Z. Huang, B. Dong, W. Zhang, J. Fan and C. Zhi, *ACS Nano*, 2020, **14**, 9089–9097.
182 B. Ngozichukwu, E. Pranada, D. Johnson and A. Djire, *ACS Appl. Nano Mater.*, 2024, **7**, 13765–13774.
183 A. Vijayaprabhakaran and M. Kathiresan, *Mater. Adv.*, 2023, **4**, 3593–3602.
184 M. Li, Y. Wang, T. Li, J. Li, L. Huang, Q. Liu, J. Gu and D. Zhang, *J. Mater. Chem. A*, 2021, **9**, 922–927.
185 K. Mahabari, R. D. Mohili, M. Patel, A. H. Jadhav, K. Lee and N. K. Chaudhari, *Nanoscale Adv.*, 2024, **6**, 5388–5397.
186 L. Qin, J. Jiang, J. Halim, J. Palisaitis, P. O. A. Persson and J. Rosen, *ACS Appl. Energy Mater.*, 2025, **8**, 9069–9074.
187 B. Unnikrishnan, C.-W. Wu, A. Sangili, Y.-J. Hsu, Y.-T. Tseng, J. Shanker Pandey, H.-T. Chang and C.-C. Huang, *J. Colloid Interface Sci.*, 2022, **628**, 849–857.
188 X. Du, X. Zhang, S. Zhu, Y. Xu and Y. Wang, *Sustainable Energy Fuels*, 2023, **7**, 4977–4983.
189 H. Chen, A. D. Handoko, J. Xiao, X. Feng, Y. Fan, T. Wang, D. Legut, Z. W. Seh and Q. Zhang, *ACS Appl. Mater. Interfaces*, 2019, **11**, 36571–36579.
190 J. Cai, J. Huang, A. Cao, Y. Wei, H. Wang, X. Li, Z. Jiang, G. I. N. Waterhouse, S. Lu and S.-Q. Zang, *Appl. Catal., B*, 2023, **328**, 122473.
191 Y. H. Moon, H. Shin, I. Kim, Y. Jo, T. H. Han and Y. J. Jang, *Nanoscale*, 2025, **17**, 25700–25709.
192 Y. Wu, Y. Li, Y. Yang, S. Zhang, B. Liu, X. Ma, Z. Liu, H. Li and J. Wang, *Fuel*, 2026, **407**, 137372.
193 H. Zong, W. Liu, M. Li, S. Gong, K. Yu and Z. Zhu, *ACS Appl. Mater. Interfaces*, 2022, **14**, 10738–10746.
194 T. Wu, X. Pang, S. Zhao, S. Xu, Z. Liu, Y. Li and F. Huang, *Small Struct.*, 2022, **3**, 2100206.
195 L. Zhou, Q. Tian, X. Shang, Y. Zhao, W. Yao, H. Liu and Q. Xu, *Green Chem.*, 2024, **26**, 1454–1461.
196 M. Li, J. Wang, S. Wei, Y. Wang, Y. Cao, H. Wang, S. Chen, J. Li, J. Huang and Y.-N. Liu, *Ind. Eng. Chem. Res.*, 2025, **64**, 17750–17758.

197 S.-H. Yin, X.-H. Li, R.-Z. Zhang and H.-L. Cui, *FlatChem*, 2024, **44**, 100632.
198 J. Duan, Z. Liu, G. Hang, Y. Wang and X. Wang, *Appl. Surf. Sci.*, 2025, **711**, 164034.
199 X. Bai, X.-H. Zha, Y. Qiao, N. Qiu, Y. Zhang, K. Luo, J. He, Q. Li, Q. Huang, J. S. Francisco, C.-T. Lin and S. Du, *Nanoscale*, 2020, **12**, 3795–3802.
200 L. Wang, Y. Tan, Z. Yu, H. Tian, Y. Lai, Y. He, H. Xiang, J. Wang, W. Zhao and L. Zhang, *Mater. Chem. Front.*, 2021, **5**, 7883–7891.
201 X. He, S. Jin, L. Miao, Y. Cai, Y. Hou, H. Li, K. Zhang, Z. Yan and J. Chen, *Angew. Chem., Int. Ed.*, 2020, **59**, 16705–16711.
202 Z. Pan, L. Kang, T. Li, M. Waqar, J. Yang, Q. Gu, X. Liu, Z. Kou, Z. Wang, L. Zheng and J. Wang, *ACS Nano*, 2021, **15**, 12975–12987.
203 A. Kadangodan Putiyaveettil and B. Natesan, *J. Phys. Chem. C*, 2024, **128**, 12777–12791.
204 S. Mani and M. M. Islam, *Nanoscale*, 2025, **17**, 24196–24207.
205 X. Wang, X. Shen, Y. Gao, Z. Wang, R. Yu and L. Chen, *J. Am. Chem. Soc.*, 2015, **137**, 2715–2721.
206 Y. Wang, C. Ma, W. Ma, W. Fan, Y. Sun, H. Yin, X. Shi, X. Liu and Y. Ding, *2D Mater.*, 2019, **6**, 045025.
207 C. Huang, S. Shi and H. Yu, *ACS Energy Lett.*, 2021, **6**, 3464–3472.
208 X. Ma, X. Zhu, C. Huang and J. Fan, *J. Membr. Sci.*, 2022, **647**, 120334.
209 S. Kim, S. Lee, H. S. Ryu, H. Jo, J. Yun, S. Mun, S. Park, K. Kim and H.-D. Lim, *Chem. Eng. J.*, 2025, **513**, 162294.
210 B. P. Thapaliya, C. J. Jafta, H. Lyu, J. Xia, H. M. Meyer III, M. P. Paranthaman, X.-G. Sun, C. A. Bridges and S. Dai, *ChemSusChem*, 2019, **12**, 1316–1324.
211 B. Wicklein, G. Valurouthu, H. Yoon, H. Yoo, S. Ponnan, M. Mahato, J. Kim, S. S. Ali, J. Y. Park, Y. Gogotsi and I.-K. Oh, *ACS Appl. Mater. Interfaces*, 2024, **16**, 23948–23959.
212 S. Mun, S. Kim, J. Yun, H. S. Ryu, S. Park, H. Jo and H.-D. Lim, *ACS Appl. Energy Mater.*, 2025, **8**, 6474–6481.
213 D. Zhang, S. Wang, B. Li, Y. Gong and S. Yang, *Adv. Mater.*, 2019, **31**, 1901820.
214 Q. Gu, Y. Cao, J. Chen, Y. Qi, Z. Zhai, M. Lu, N. Huang and B. Zhang, *Nano-Micro Lett.*, 2024, **16**, 266.
215 Y. Zhao, B. Li, C. Tian, X. Han, Y. Qiu, H. Xiong, K. Li, C. Hou, Y. Li, H. Wang and Q. Zhang, *Chem. Eng. J.*, 2023, **469**, 143862.
216 S. Ha, D. Kim, H.-K. Lim, C. M. Koo, S. J. Kim and Y. S. Yun, *Adv. Funct. Mater.*, 2021, **31**, 2101261.
217 G. R. Berdiyorov, *Appl. Surf. Sci.*, 2015, **359**, 153–157.
218 Y. Dall'Agnese, M. R. Lukatskaya, K. M. Cook, P.-L. Taberna, Y. Gogotsi and P. Simon, *Electrochem. Commun.*, 2014, **48**, 118–122.
219 X. Yang, M. Zhang, C. Wang, M. Bi, J. Xie, W. Bai, Y. Zhang, S. Pan, M. Liu, X. Pan, Z. Lu, Z. Han and Y. Fu, *J. Energy Storage*, 2023, **71**, 108140.
220 H. Liu, B.-Q. Chen, C.-Y. Li, C.-J. Fang, R. K. Kankala, S.-B. Wang and A.-Z. Chen, *Small*, 2024, **20**, 2305321.
221 N. Xue, X. Li, M. Zhang, L. Han, Y. Liu and X. Tao, *ACS Appl. Energy Mater.*, 2020, **3**, 10234–10241.
222 W. Xiong, X. Feng, Y. Xiao, T. Huang, X. Li, Z. Huang, S. Ye, Y. Li, X. Ren, X. Wang, X. Ouyang, Q. Zhang and J. Liu, *Chem. Eng. J.*, 2022, **446**, 137466.
223 L. Liang, L. Niu, T. Wu, D. Zhou and Z. Xiao, *ACS Nano*, 2022, **16**, 7971–7981.
224 K. Yang, S. Ren, H. Huang, B. Wu, G. Shen, T. Zhou and X. Liu, *Front. Chem.*, 2022, **9**, 832449.
225 M. Hilal, W. Yang, Y. Hwang and W. Xie, *Nano-Micro Lett.*, 2024, **16**, 84.
226 Y. Qin, X.-H. Zha, X. Bai, K. Luo, Q. Huang, Y. Wang and S. Du, *J. Phys.: Condens. Matter*, 2020, **32**, 135302.
227 M. Hu, S. Li, J. Yu, J. Jiu, Y.-P. Wu, X.-Q. Wu, G. Hai, Q.-W. Han and D.-S. Li, *Sep. Purif. Technol.*, 2026, **386**, 136525.
228 W. Eom, H. Shin, W. Jeong, R. B. Ambade, H. Lee and T. H. Han, *Mater. Horiz.*, 2023, **10**, 4892–4902.
229 H. Bark, G. Thangavel, R. J. Liu, D. H. C. Chua and P. S. Lee, *Small Methods*, 2023, **7**, 2300077.
230 P. Liu, P. Xiao, M. Lu, H. Wang, N. Jin and Z. Lin, *Chin. Chem. Lett.*, 2023, **34**, 107426.
231 W. Bao, C. E. Shuck, W. Zhang, X. Guo, Y. Gogotsi and G. Wang, *ACS Nano*, 2019, **13**, 11500–11509.
232 D. Gandla, Q. Li, Y. A. Zhou, Y. Yan, Z. Liu, J. Chen and D. Q. Tan, *Small*, 2024, **20**, 2404880.
233 L. Zhu, J. Ji, H. Yin and H. Zhao, *Energy Fuels*, 2023, **37**, 5607–5612.
234 F. Tian, F. Wang, W. Nie, X. Zhang, X. Xia, L. Chang, Z. Pang, X. Yu, G. Li, S. Hu, Q. Xu, H.-Y. Hsu, Y. Zhao, L. Ji, X. Lu and X. Zou, *Angew. Chem., Int. Ed.*, 2024, **63**, e202408996.
235 R. Sewak and A. Mondal, *ACS Appl. Nano Mater.*, 2025, **8**, 21964–21974.
236 N. Li, J. Fan and J. Jia, *J. Power Sources*, 2025, **640**, 236783.
237 T. Zhang, K. Shevchuk, R. J. Wang, H. Kim, J. Hourani and Y. Gogotsi, *Chem. Mater.*, 2024, **36**, 1998–2006.
238 Y. Cao, S. Wei, Q. Zhou, P. Zhang, C. Wang, K. Zhu, W. Xu, X. Guo, X. Yang, Y. Wang, X. Wu, S. Chen and L. Song, *2D Mater.*, 2023, **10**, 014001.
239 B. Davis, D. LaBelle, H. Kim, T. Zhang, T. Parker, S. Ippolito, K. Shevchuk, J. Kim, G. Valurouthu, Y.-J. Hu and Y. Gogotsi, *Angew. Chem., Int. Ed.*, 2026, **65**, e15780.
240 M. Peng, Z. Wu, W. Wei, H. Xu, C. Liu and C. Shen, *Adv. Mater. Interfaces*, 2022, **9**, 2102418.
241 T. Guo, W. Wei, J. Chai, Y. Ren, M. yilmaz, A. Uddin, A. Cabot and D. Zhou, *Small*, 2025, **21**, e08556.
242 Y. Tian, W. Que, Y. Luo, C. Yang, X. Yin and L. B. Kong, *J. Mater. Chem. A*, 2019, **7**, 5416–5425.
243 J. H. H. Rossato, H. G. Lemos, I. C. Gouvea, M. Lounasvuori, E. Nandayapa, A. Tarasov, M. Tomic, S. F. Santos, F. Stavale, E. Unger and C. F. O. Graeff, *Sol. Energy*, 2025, **298**, 113668.
244 H. Shi, M. Ma, Y. Sun, M. Cui and A. Qian, *Adv. Funct. Mater.*, 2024, **34**, 2410006.
245 J. Tang, T. S. Mathis, N. Kurra, A. Sarycheva, X. Xiao, M. N. Hedhili, Q. Jiang, H. N. Alshareef, B. Xu, F. Pan and Y. Gogotsi, *Angew. Chem., Int. Ed.*, 2019, **58**, 17849–17855.

 This journal is © The Royal Society of Chemistry 2026

246 L. Meng, L.-K. Yan, F. Viñes and F. Illas, *J. Mater. Chem. A*, 2023, **11**, 6886–6900.
247 M. A. K. Purbayanto, M. Chandel, M. Birowska, A. Rosenkranz and A. M. Jastrzębska, *Adv. Mater.*, 2023, **35**, 2301850.
248 I. Hussain, A. Iqbal, F. Bibi, S. Pandiyarajan, S. N. Banitaba, S. Khademolqorani, M. S. Javed, H.-C. Chuang and K. Zhang, *SusMat*, 2025, **5**, e259.
249 X. Xu, D. Feng, L. You, Y. Xie, F. Wu, Y. Zhu, Y. Mei and D. Xie, *Energy Mater. Adv.*, 2024, **5**, 0146.

This journal is © The Royal Society of Chemistry 2026